NISTIR 89-4167

RESEARCH FOR ELECTRIC ENERGY SYSTEMS - AN ANNUAL REPORT

R. J. Van Brunt, Editor

U.S. DEPARTMENT OF COMMERCE
National Institute of Standards
and Technology
Center for Electronics and
Electrical Engineering
Electrosystems Division
Gaithersburg, MD 20899

U.S. DEPARTMENT OF COMMERCE
Robert A. Mosbacher, Secretary
NATIONAL INSTITUTE OF STANDARDS
AND TECHNOLOGY
Raymond G. Kammer, Acting Director

NIST

NISTIR 89-4167

RESEARCH FOR ELECTRIC ENERGY SYSTEMS - AN ANNUAL REPORT

R. J. Van Brunt, Editor

U.S. DEPARTMENT OF COMMERCE
National Institute of Standards
and Technology
Center for Electronics and
Electrical Engineering
Electrosystems Division
Gaithersburg, MD 20899

Prepared for
Department of Energy
Division of Electric Energy Systems
1000 Independence Avenue, SW
Washington, DC 20585

December 1988

Issued October 1989

U.S. DEPARTMENT OF COMMERCE
Robert A. Mosbacher, Secretary
NATIONAL INSTITUTE OF STANDARDS
AND TECHNOLOGY
Raymond G. Kammer, Acting Director

Foreword

This report summarizes the progress of four technical investigations conducted during CY 88. Although reasonable efforts have been made to ensure the reliability of the data presented, it must be emphasized that this is an interim progress report and that further experimentation and analysis may be performed before the conclusions from any of these investigations are formally published. It is therefore possible that some of the observations presented in this report will be modified, expanded, or clarified by our subsequent research.

Table of Contents

Research for Electric Energy Systems – An Annual Report

R. J. Van Brunt, Editor

Abstract

This report documents the technical progress in the four investigations which make up the project "Support of Research Projects for Electrical Energy Systems", Department of Energy Task Order Number 137, funded by the U.S. Department of Energy and performed by the Electrosystems Division of the National Institute of Standards and Technology (NIST). The first investigation covers the measurement of ions in the vicinity of dc high-voltage transmission lines and in biological exposure facilities designed to simulate the environment around transmission lines. The measurements of ion mobilities at atmospheric pressure using two different types of drift tubes are discussed. Results are also presented from an investigation into the uncertainties associated with measurement of monopolar space-charge densities in the atmosphere around high-voltage transmission lines where dc electric fields are present. The second area of investigation is concerned with the behavior of gaseous dielectrics like SF_6 used in high-voltage power systems. Results from two significant technical activities in this area are summarized here. The first is concerned with measurement of collisional electron detachment probabilities for negative ions moving in gaseous SF_6 and the implications of the results of these detachment measurements on achieving a better understanding of ion transport and positive discharge initiation probabilities in SF_6. The second is about a new method for measuring the stochastic behavior of pulsating partial-discharge phenomena. Although this method is applied here to an investigation of Trichel-pulse corona in gas mixtures like air and SF_6/O_2, it is argued that it has a more general application to measurement of partial discharges and offers the possibility of revealing much more information about the physical bases for these processes than can be achieved by presently used measurement techniques. The third area of investigation has to do with observation of prebreakdown phenomena in dielectric liquids. Results are presented here from optical observations of the influence of hydrostatic pressure on prebreakdown partial discharge development and from measurement of nanosecond impulse breakdown at liquid-solid interfaces. An image-preserving optical delay system is described for use in obtaining photographs of improbable fast breakdown events in liquids. The fourth area of research discussed in this report is concerned with electrical measurement of fast transient phenomena. Results are presented from an investigation into the interactions between two dividers used simultaneously to measure fast impulse voltages. A discussion is given about the difficulties encountered in attempting direct comparisons of the responses from two impulse dividers used simultaneously. Techniques for minimizing the effects of the interactions on measurement accuracy are considered.

1. ELECTRIC FIELD MEASUREMENTS

Task 01

Martin Misakian, William Anderson, and Ronald McKnight
Electricity Division
National Institute of Standards and Technology

1.1 Introduction

The objectives of this project are to develop methods to evaluate and calibrate instruments which are used, or are being developed, to characterize the electrical parameters in the vicinity of power lines and in laboratory apparatus designed to simulate the power line environment. Electrical measurement support is also provided for DOE-funded efforts to determine if there are biological effects due to ac fields and dc fields with ions.

The electrical parameters of interest include the electric field strength, magnetic flux density, ion current and charge densities, ion mobility and ion species. Recent laboratory studies have focused on the measurement of ion mobilities at atmospheric pressure using drift-tubes. During the past year the evaluation of two drift tubes fabricated from insulating cylinders was completed. Excerpts from this study are presented in the following sections. A manuscript which describes the full study has been accepted for publication [1]. The influence of a dc electric field on the measurement of monopolar charge densities using an aspirator-type ion counter and the measurement of net space charge density using a Faraday cage or filter was also examined. Optimum configurations which minimized the effect of the electric field were identified for each type of instrument. Some results of this study are briefly described in this report. A full account of the work will be published at a later date [2]. Other NIST activities in 1988 included: three revisions of a new IEEE draft standard which will provide guidance for the measurement of dc power line fields and ion-related parameters; a site visit to the Battelle Pacific Northwest Laboratories to characterize electrical parameters in several bioeffects exposure systems; and invited conference talks at the IEEE Instrumentation and Technology Conference and the NSF sponsored U.S.-Japan Seminar on Electromagnetic Interference in Highly Advanced Social Systems. Both talks considered measurement procedures for characterizing electrical parameters near ac and dc power lines.

1.2 Ion Mobility and Drift Tubes

The mobility of an ion as it moves through a gas under the influence of a weak electric field is defined as the ratio of the ion drift velocity to the electric field strength. Corrections for pressure and temperature are normally made to obtain a "reduced mobility." As has been noted previously, the motivation for measuring ion mobilities, within the context of possible bioeffects due to dc power lines, is that mobility values provide, in some cases, a rough measure of ion mass [3, 4]. Ideally, the ion species is of interest when considering the possibility of bioeffects due to exposure to ions from dc power lines, but sampling ions at atmospheric pressure with a mass spectrometer is difficult and requires a complex apparatus [5]. Ion mobility spectra can be measured at atmospheric pressure with less complicated instrumentation and ascertaining that the mobility spectra remain unchanged during a bioeffects study may be as important as knowing that the electric field strength or ion current density remains constant.

Ion mobility can be determined by measuring the time required for an ion to travel a given distance in a known dc electric field. A device that that has been used extensively for this measurement is the drift tube. The two drift tubes that were evaluated are shown in Figure 1 and have been described in detail previously [6]. The construction of the drift tubes differs from those of conventional design in that metal guard rings with insulating spacers and alignment rods have been replaced with an insulating tube on which guard rings have been coated.

Figure 1(a) shows a drift tube designed to operate in a pulsed time-of-flight (TOF) mode. Briefly, ions arriving from the right are prevented entry into the drift tube by the shutter which is biased shut with a small voltage supplied to the outside mesh. The ions are produced in untreated room air by wires in corona, using an apparatus that has been previously described [7]. Ions enter the drift tube and travel to the collector after the shutter is pulsed open for a fraction of a millisecond. Because more than one species of ions is present in the approximately disk-shaped volume of ions that passes through the shutter, the ions will separate into groups with the same drift velocity or mobility as they traverse the length of the drift tube. A shield grid before the collector prevents the induction of current in the collector circuit until the ions pass through the shield grid. The current induced in the collector circuit as the ions travel between the shield and collector is monitored and exhibits maxima and minima as a function of time because of the different time-of-flights of the different ion species. The length of the drift region is variable so that the distance the ions travel can be made nominally 4 cm or 8 cm. By obtaining TOF spectra at two drift distances, it is possible to eliminate so called "end effects" when computing the TOF of a given ion peak.

Figure 1(b) shows a schematic view of an ac TOF drift tube similar in principle to that employed by Tyndall and Powell [8]. The shutters at each end of the drift tube

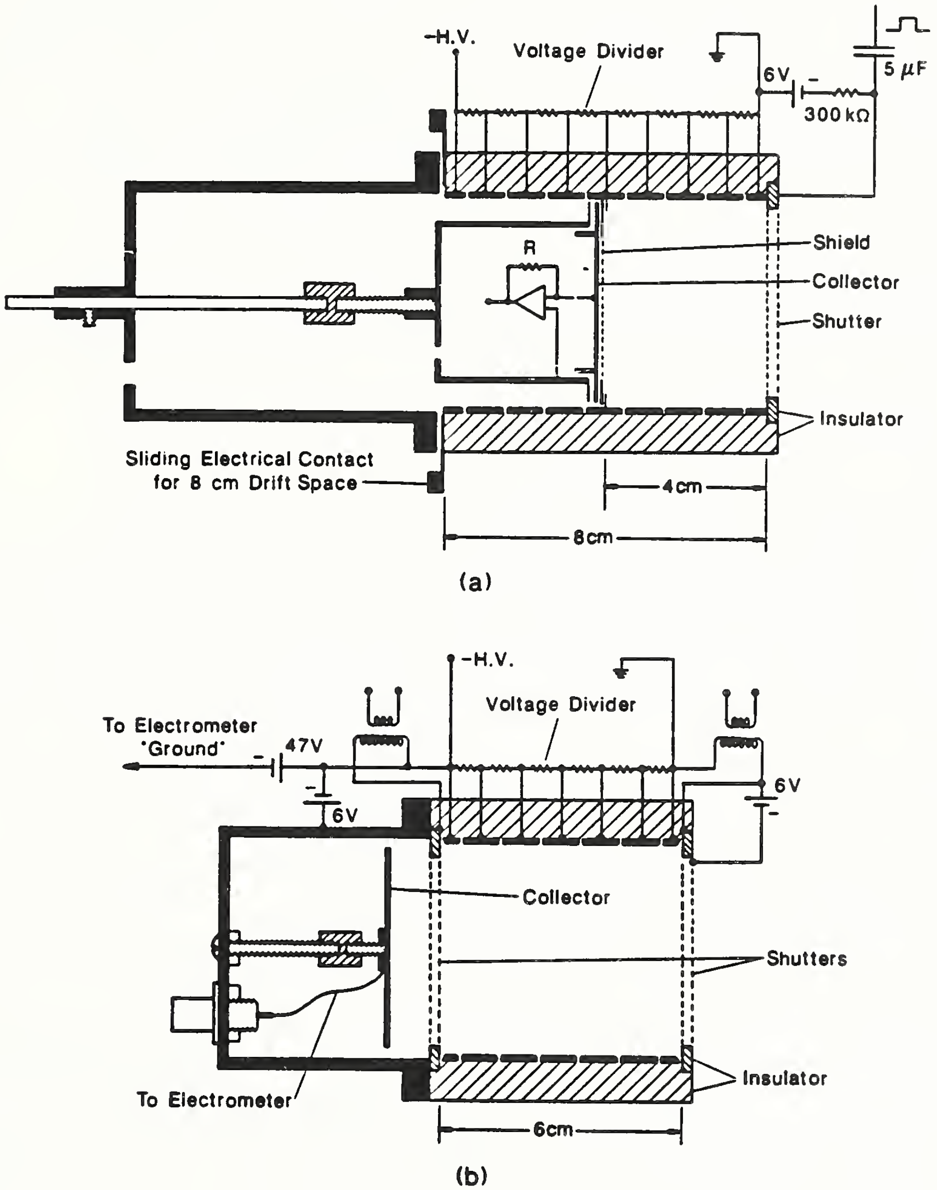

Figure 1. Schematic views of drift tubes made of insulating cylinders with conductive guard rings on the inside walls. (a) pulsed time-of-flight drift tube with movable collector electrode. Metal tabs at L equal to 4 cm and 8 cm (movable) provide appropriate potential to shield grid. (b) ac time-of-flight drift tube. The inside diameter of each tube is 5.65 cm.

are biased closed and are opened periodically with sinusoidal voltages applied to the inner mesh of each shutter. Ions that have TOF's between the shutters equal to half the period of the ac voltage will pass through both shutters to yield a steady-state current which is measured with an electrometer. Ideally, measurement of ion current as a function of frequency results in current maxima at specific frequencies for ions with different mobilities. The mobility of an ion, K, is given by the expression

$$K = 2L^2 f / V, \tag{1}$$

where f is the frequency of the current maximum, L is the length of the drift space and V is the voltage across the drift tube.

1.3 Experimental Results

At the close of 1988, it had been determined that (1) for the pulse TOF drift tube, there existed a discrepancy between the shape and peak position of measured TOF spectra and that determined from theory and (2) the use of sinusoidal voltage waveforms to gate the shutters of the ac TOF drift tube failed to resolve ions with different mobility in the TOF spectrum [6]. The resolution of these problems is described below.

(1) Matching Theoretical and Experimental Spectra: Pulse TOF Drift Tube

Figure 2 shows fits of the fastest TOF feature of complex positive ion spectra obtained on different days for a drift space of 8 cm. The fits are made using trial values of drift velocities in a theory described in detail previously [6]. This theory takes into account such factors as diffusion, shutter pulse width, and transit time between the shield grid and collector. The choice of drift velocity is made by matching the calculated initial rise of the ion current with the experimental one. Ideally, the fit should be to the shape of the spectrum, but simultaneous matching of the onset and peak ion currents in figure 2 was not possible. The data in figures 2(a) and 2(b) are obtained with feedback resistors in the amplifier circuit [R in fig. 1(a)] of 2000 and 200 MΩ, respectively.

It is found that the fitting process yields mobility values that are in good agreement with values determined by obtaining TOF spectra for two different drift distances. This latter approach is expected to yield the most accurate mobility values because it is free of end effects. While there is agreement between the mobility values determined experimentally ($1.97 \pm 0.02 \times 10^{-4}$ m^2/Vs), the shape of the calculated spectrum as noted above does not match the data very well in figure 2(a). The agreement between mobility values suggests that the peak of the measured spectrum may be shifted to a longer TOF due to (i) the possible overlapping with a slower adjacent feature, (ii) an instrumental effect, or (iii) some combination of (i) and (ii).

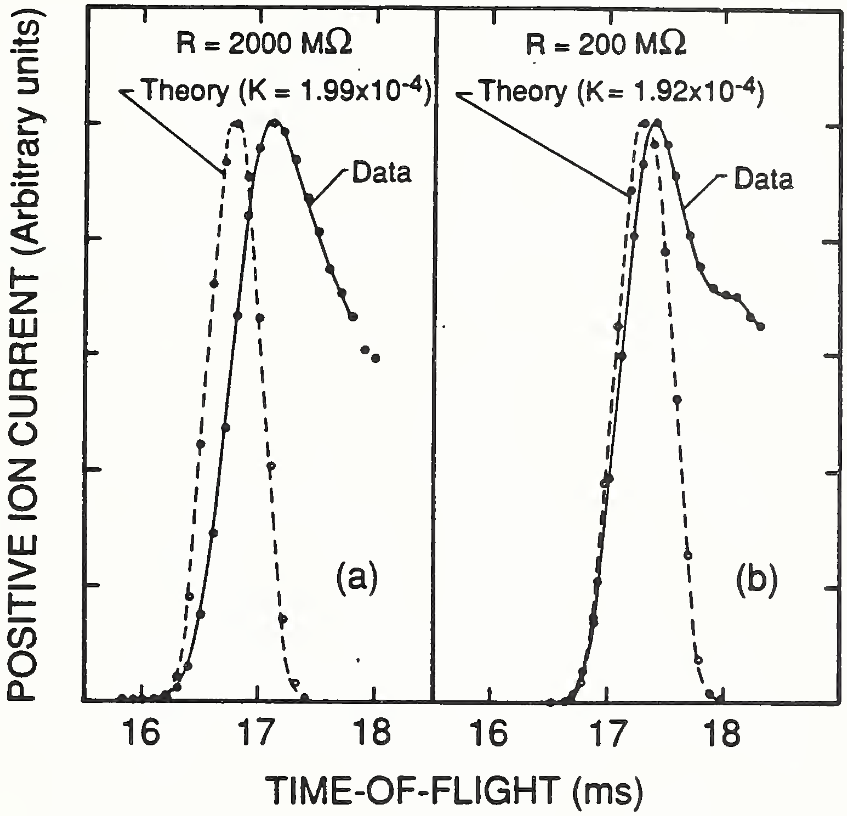

Figure 2. TOF spectra of positive ions with the largest mobility, obtained with the pulse-TOF drift tube ($L = 8\,\text{cm}$) on different days. The data, represented by the solid curves, are fitted with theoretical curves (dashed curves) and assuming the indicated mobility values. (a) measurement performed with 2000 megohm feedback resistor in current-to-voltage amplifier circuit. (b) measurement performed with 200 megohm feedback resistor on different day. While the spectra overlap with slower adjacent features, the discrepancies between theoretical and measured peak TOF values is due mainly to excessively long circuit time constants.

While there is some overlap of the fastest TOF feature with an adjacent slower one, mechanism (ii) appears to be the predominant reason for the discrepancy in peak position. Because of the 2000 megohm feedback resistor, stray capacitances of a few tenths-of-picofarads in the circuit can lead to time constants of several tenths-of-milliseconds and cause the observed shift in the TOF of the peak ion current. This explanation is supported by the results in figure 2(b) which shows improved agreement between the calculated fit and data when the feedback resistor is reduced by a factor of ten. The calculated and experimental mobility values are $1.92 \pm 0.02 \times 10^{-4}\,\mathrm{m^2/Vs}$ and $1.92 \pm 0.02 \times 10^{-4}\,\mathrm{m^2/Vs}$, respectively, and the difference in peak positions is reduced to about 0.1 ms. A risetime of about 40 μsec in an optical link circuit, not shown in figure 1, also contributes to the discrepancies in TOF's in figure 2. Further evidence for the time constant explanation is provided below when new data obtained using the ac TOF technique are discussed.

(2) Resolving Ions With Different Mobilities Using AC TOF Drift Tube

As has been previously noted [6], a theoretical expression for a TOF spectrum is not readily developed when the shutters of the ac drift tube are gated open with a sinusoidal voltage. However, a more serious difficulty is that at atmospheric pressure, the frequency of the gating voltage can be below 50 Hz. At such low frequencies and for the ac voltage amplitudes required to produce adequate signal strength, the duration of the open condition can be several milliseconds. The long duration results in a very broad spectrum making it difficult to identify the frequency in Eq. 1. Because more than one ion species is normally present in the spectrum, the long opening of the shutters also results in the loss of resolution of the individual current maxima.

During 1988, the sinusoidal waveform was replaced with a pulse waveform of alternating polarity. This modification permitted the derivation of an expression which describes the spectrum shape as a function of frequency of a single ion species and it also became possible to resolve ions of different mobility in the experimental spectra. [1]. With the alternating pulse waveform, the expression for ion mobility that corresponds to Eq 1 becomes [1]

$$K_{\mathrm{acp}} = FL^2/V. \tag{2}$$

F is the inverse of the ion TOF and is given by

$$F = [(1/f_p) - \delta]^{-1}, \tag{3}$$

where f_p is the experimental frequency corresponding to the peak ion current and δ is the delay in ion TOF as the ion passes through the first shutter (δ is determined experimentally).

To gate the shutters of the ac drift tube in the ac pulse mode, the transformers in figure 1(b) were replaced with phototransistor optoisolators as shown in figure 3.

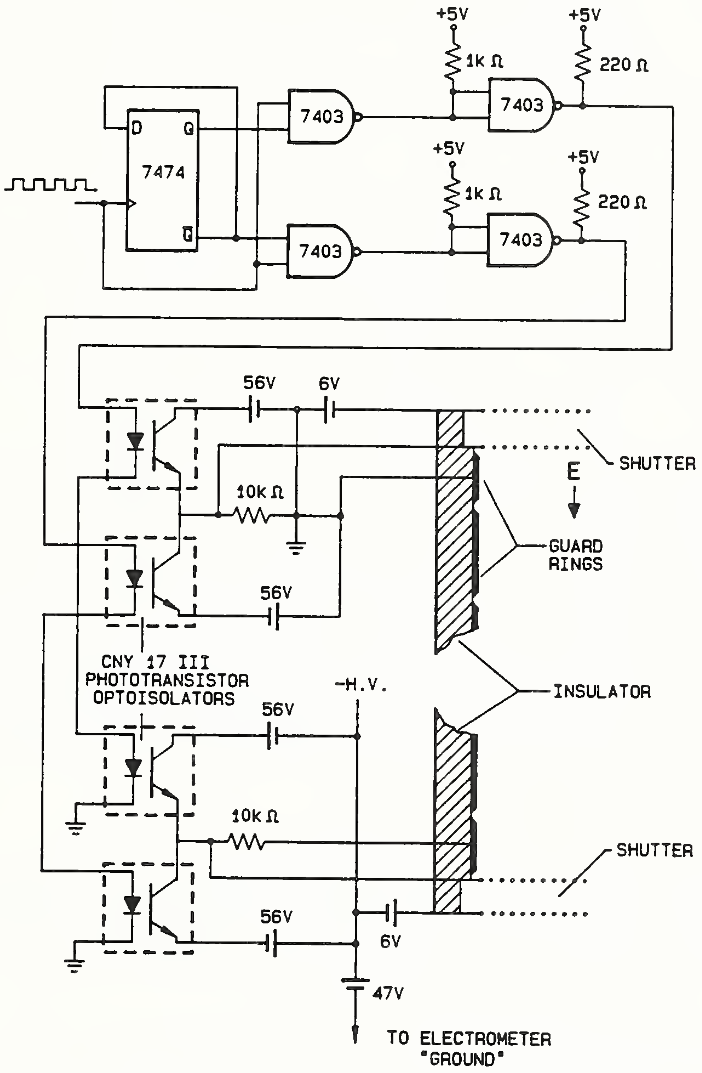

Figure 3. Schematic view of circuit which converts pulses from the function generator to pulses of alternating polarity. Nearly identical pulse voltages are applied to the inner mesh of each shutter to maintain the same electric field in the drift space.

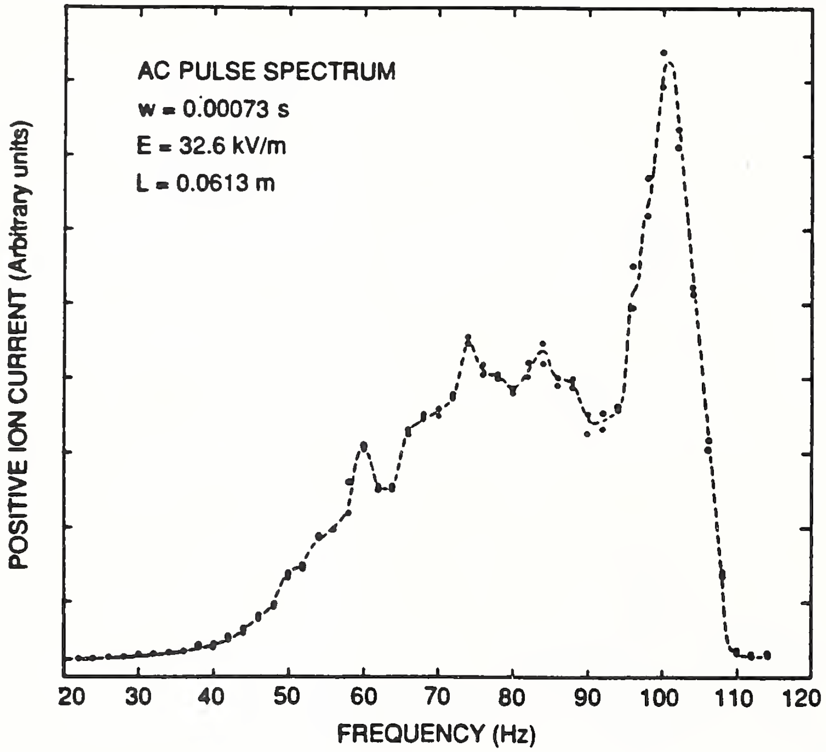

Figure 4. Positive ion current as a function of shutter frequency. The current measurements are made with the ac TOF drift tube, using alternating-polarity pulse-voltages (pulsewidth = 0.73 ms) to gate the shutters. The dashed curve indicates the general features of the spectrum.

A train of rectangular pulses from a waveform generator is converted into pulses of alternating polarity by means of TTL flip-flop NAND gates. The same voltage waveform is applied to the inner mesh of each shutter as for the sinusoidal waveform.

An example of spectra that is obtained when the sinusoidal waveform is replaced by a pulse waveform of alternating polarity is shown in figure 4. The data represent positive ion collector current for two sweeps of the frequency from 20 Hz to 114 Hz in 2-Hz increments. Each point is an average of five current measurements using an electrometer-voltmeter combination. While the structure in figure 4 is reproducible, in general, considerable variation of the peak intensities occurs above 80 Hz. The data in figure 5 represent four sweeps of the pulse frequency from 85 Hz to 113 Hz in 1-Hz increments and is compared with a calculated spectrum (solid curve) determined from theory.

For the spectrum in figure 5, $L = 6.13 \pm 0.03\,\mathrm{cm}$, $f_p = 101 \pm 1\,\mathrm{Hz}$, $V = 2000 \pm 2\,\mathrm{V}$, and $\delta = 0.27 \pm 0.02\,\mathrm{ms}$. From Eqs (2) and (3), the value of mobility is $1.95 \pm 0.03 \times 10^{-4}\,\mathrm{m^2/Vs}$. The mobility determined from the theoretical fitting process is also $1.95 \pm 0.02 \times 10^{-4}\,\mathrm{m^2/Vs}$.

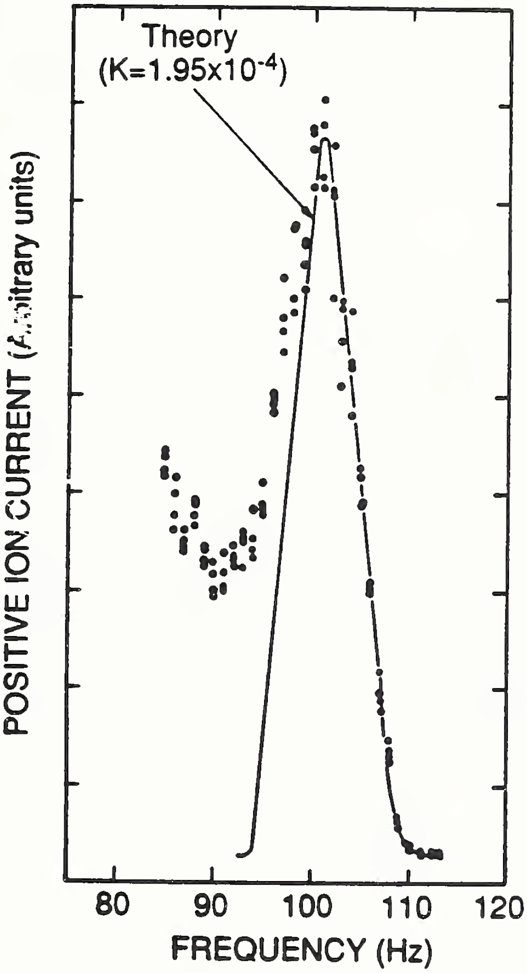

Figure 5. Positive ion current as a function of shutter frequency for the same conditions in figure 4. The solid curve is a theoretical fit of the fastest feature. The data in this figure and in figure 2(a), using the pulse-TOF drift tube, were obtained nearly simultaneously.

The results in figure 5 should be compared with the spectrum shown in figure 2(a), which was measured at the same time using the pulse-TOF drift tube. All of the mobility values agree within the noted uncertainties. Also, it can be shown that the theories for the pulse and ac-pulse spectra are the same except for the technique of detecting the ion current [1]. The ac-pulse measurement technique involves the measurement of an average steady-state ion current at each frequency or TOF and circuit time constant problems are avoided. Thus, the good agreement between the shape of the data and the calculated spectrum in figure 5 provides further evidence that the discrepancy between the calculated and experimental peak TOF's in figure 2(a) is due to stray capacitance effects in the current detector of the pulse-TOF drift tube.

1.4 Conclusions

This study examined the operation of two types of drift tubes that are suitable for measuring ion mobilities at atmospheric pressure in the presence of large dc electric fields. The fabrication of the drift tubes from insulating cylinders with guard rings coated on the inside wall differs from conventional designs employing stacked metal guard rings with precision insulating spacers. The fabrication costs should, in general, be less. The good mobility values and theoretical fits of the spectra suggest that the exposed insulators between the coated guard rings do not significantly affect the determination of ion mobility for atmospheric pressure conditions.

1.5 DC Electric Field Effects During Measurement of Monopolar Charge Density and Net Space Charge Density

This NIST study briefly examined errors that arise due to the influence of a dc power line electric field during measurements of monopolar charge densities with an aspirator-type ion counter [9] and during the measurement of net space charge density using Faraday cages and filters [10, 11]. Where appropriate, measurements were considered with the instrumentation in and above the ground plane. The study made use of theory developed by Swann for terrestrial electric fields and air ions [12], and recent experimental results which are supportive of Swann's theory even for cases where there is significant distortion of the electric field due to space charge [13, 14]; the latter case can be found near high voltage dc transmission lines [15, 16]. The focus of the study was on the influence of the electric field. Errors which can occur due to other factors such as wind, Coulomb repulsion, uncertainties in the measurement of ion current or volumetric air flow were not considered. What is presented in the following sections are excerpts from the study that focuses on above-ground measurements of monopolar charge density with ion counters and measurements of net space charge density with filters.

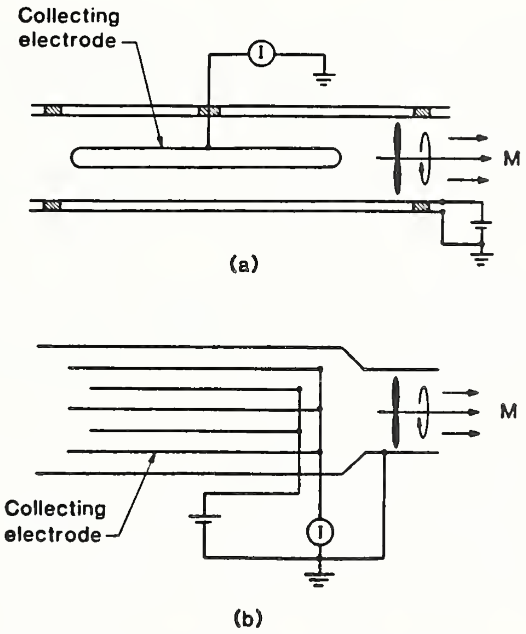

Figure 6. Schematic view of aspirator-type ion counters: (a) cylindrical geometry, (b) parallel-plate geometry. The polarizing potential provided by the battery permits measurement of positive charge densities.

1.6 Monopolar Charge Density Measurements

Schematic views of cylindrical and parallel plate aspiratory-type ion counters are shown in figure 6. Under ideal conditions, the measured monopolar charge density, ρ_{m}, is given by the expression [9]

$$\rho_{\mathrm{m}} = I/M \tag{4}$$

where I is the measured ion current to the collecting electrode(s) and M is the laminar volumetric flow rate of the air through the ion counter due to the action of the fan. Equation (4) is valid for ions with mobilities equal to or greater than the "critical" mobility, k_{c}, given by [9]

$$k_{\mathrm{c}} = M\epsilon_{\mathrm{o}}/CV \tag{5}$$

where C is the capacitance of the electrodes, ϵ_{o} is the permittivity of free space, and V is the voltage across the electrodes.

It can be shown from ion trajectory calculations that if there exists an electric field external to the ion counter that transports ions of a given polarity toward the ion counter, the number of ions arriving at the entrance of the ion counter can exceed that due to the aspirating action alone by a factor of two or more [2]. It can also be shown that if there is adequate electric field shielding, i.e., the collecting electrode(s) in the ion counter is shielded against the external field, the excess ions will travel to the housing of the ion counter and not be measured. With this background information, the measurement of monopolar charge density is considered for an ion counter above the ground plane in the presence of an external electric field. It is shown that if the ion counter housing is appropriately oriented and electrically biased, the measurements can be made free of errors due to the presence of the electric field.

Figure 7 schematically shows ion counters in two orientations above the ground plane for measuring negative charge densities in the presence of a uniform vertical electric field, E_o. The housing of the ion counter is shown electrically floating in figures 7(a) and 7(d), at ground potential in figures 7(b) and 7(e) and biased to attract negative ions in figures 7(c) and 7(f). The number of induced negative charges on the housing in figures 7(b) and 7(e) depends on the difference in potential between the ambient space potential and the ion counter housing; the larger this difference, which is a function of height above the ground plane, the fewer are the number of negative charges.

Electrically floating the ion counter housing at ambient space potential minimizes the perturbation of the electric field. However, the induced negative charges near the ion counter aperture for the horizontal orientation [fig. 7(a)] will repel some approaching negative ions and possibly prevent their entry into the ion counter [17]. When the ion counter housing is at ground potential or has an attractive potential applied to it [figs. 7(b) and 7(c)], the number of approaching negative ions repelled by the induced negative charges is reduced or eliminated.

Figure 8 shows experimental results demonstrating ion losses by the mechanism discussed above when the ion counter is oriented horizontally about 0.4 m above the ground plane and beneath a thin horizontal wire 2.1 m high that is in negative corona. Measurements of negative charge densities at two flow rates are shown as a function of voltage applied to the ion-counter housing [13, 18]. During the measurements, the unperturbed electric field strength in the ground plane directly beneath the wire was about 27 kV/m. Further details of the experimental arrangement can be found in the references that are cited.

When the potential of the housing is zero or positive and attracts negative ions, the measured charge densities are nominally constant at both air flow rates. The scatter of the data is due, in part, to fluctuating air currents in the laboratory which can affect the flow of ions from the monopolar line to the ion counter. As the potential of the ion counter housing approaches the ambient unperturbed space potential (determined with an electrostatic voltmeter and radioactively equilibrated probe), some negative ions are repelled by the negative charges on the housing and are not measured as discussed above. It is noted that similar experimental results have been obtained during conductivity measurements aboard airplanes [19, 20].

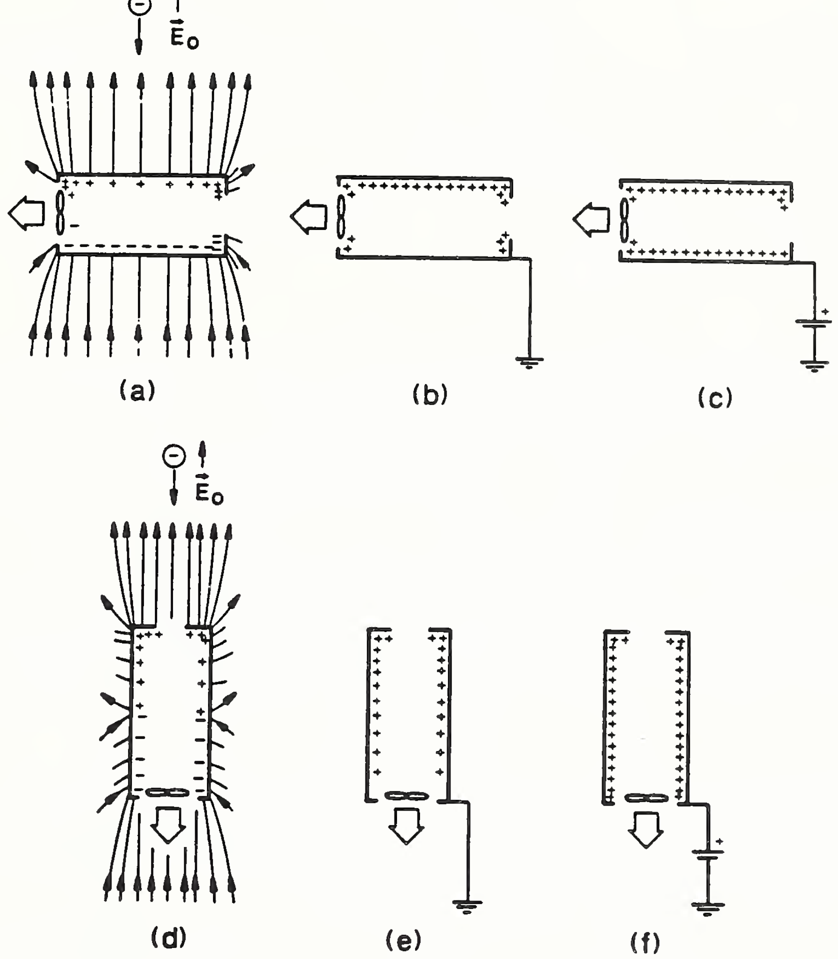

Figure 7. Schematic views of ion counter above ground plane in vertical and horizontal orientations. Induced charges produced by a uniform vertical electric field, E_o, are shown when the ion counter housing is at space potential in (a) and (d), referenced to ground potential in (b) and (e) [the number of negative charges depends on the difference in potential between the ion counter housing and ambient space potential], and biased to attract negative ions in (c) and (f).

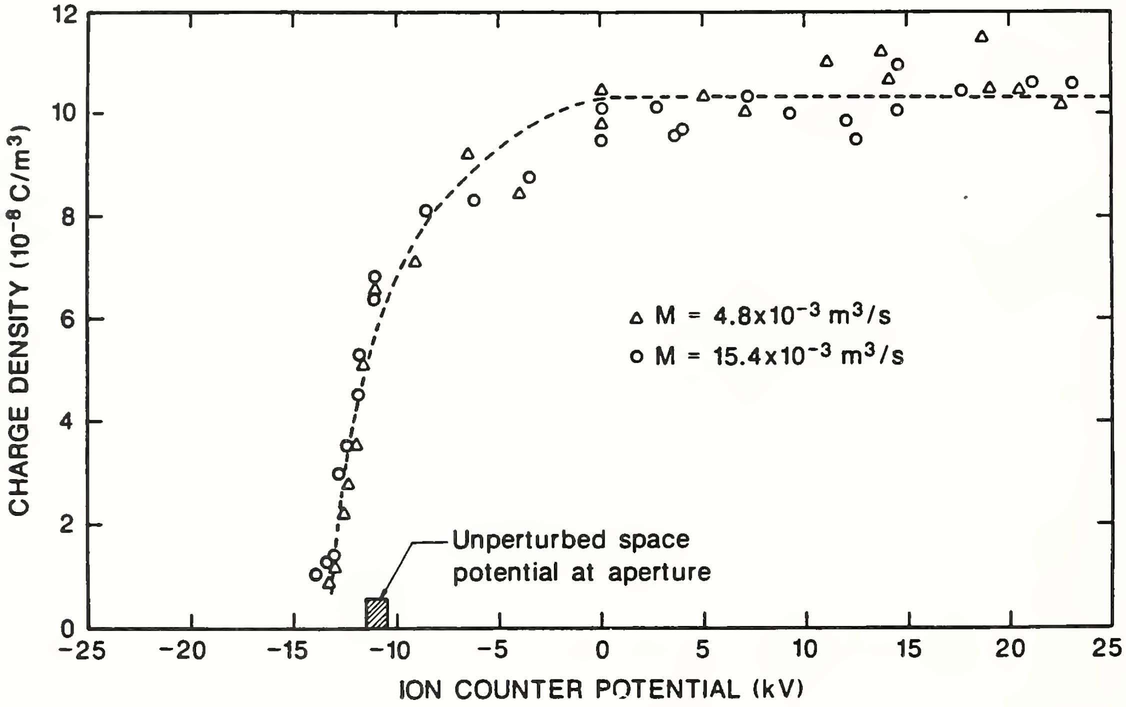

Figure 8. Above-ground ion density measurements at two air flow rates and as a function of ion counter potential. The ion counter is oriented horizontally and the unperturbed space potential at the height of the aperture is near −11 kV.

When the ion counter housing is oriented vertically and electrically biased as shown in figures 7(d), 7(e), and 7(f), the loss of approaching negative ions due to repulsion from like charges on the ion-counter housing is expected to be small or eliminated.

It appears that the optimum arrangement for above-ground charge density measurements is to orient the ion counter horizontally to reduce the effects of rain or snow, and to apply an attractive potential to the ion counter housing to eliminate ion losses due to repulsion by like charges on the housing, e.g., figure 7(c). The grounded vertical geometry shown in figure 7(e) also would be a useful arrangement in the absence of adverse weather conditions. It is noted once more that although the electric field can increase the number of ions reaching the ion counter aperture to a value in excess of that due to the aspirating action of the ion counter alone, the extra ions will not be measured provided there is adequate electric field shielding of the collecting electrodes.

1.7 Net Space-Charge Density Measurements

One measurement technique for determining net space charge density is known as the filtration method [10] and is illustrated in figure 9. Here, an air sample is drawn

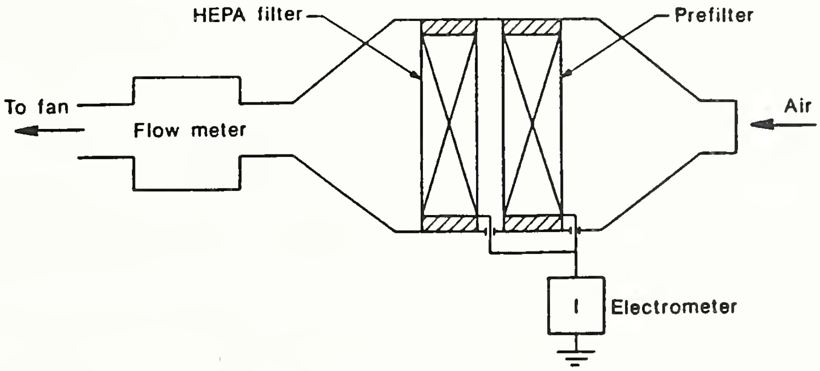

Figure 9. Schematic view of filter for measuring net space charge density. Both prefilter and HEPA filters are isolated from ground and the filter housing. To prolong the life of the HEPA filter, it is common practice to employ a prefilter made of such materials as stainless steel wool and glass fibers.

into a metal enclosure with a filter through which all the air passes. The filter is electrically isolated from the enclosure and ground so that the current, I, resulting from the charge removed from the air stream by the filter can be measured. From this current, the net space charge density can be calculated from the expression

$$\rho_s = \mathrm{I}/\mathrm{M}_o \tag{6}$$

where M_o is the volumetric air flow through the filter. This method of measuring space charge density assumes that the filter collects almost all of the charge in the air stream. High-efficiency air-particulate (HEPA) filters are adequate for this application because tests with such filters indicate that the collection efficiency for small air ions can exceed 99.8% [21, 22].

Equation 6, which is used to determine net space charge density, is derived assuming that ions of both polarity are transported into the filter by the air drawn through the filter. However, with the presence of an external electric field, ions are transported to the filter aperture under the combined effects of the air motion and electric field. It is noteworthy that the electric field will discriminate against the arrival of ions of one polarity and favor ions of the opposite polarity.

Use can be made of figure 7 for identifying an optimum arrangement for filter measurements above the ground plane. Taking the ion counter housing in figure 7 to be that of a filter, it is apparent that the optimum configuration for net space charge density measurements (but not monopolar charge density measurements) is the horizontal orientation with the housing electrically floating at space potential, i.e., figure 7(a). For this configuration ions of both polarities will be discriminated against by the induced charges near the aperture. If the positive and negative ions have comparable mobilities, the percentage of positive and negative ions repulsed by the induced charges will also be comparable. However, even with equal discrimination against ions of both polarities, the net space charge density measurement can be adversely affected unless the net space charge is zero.

Measurements of net space charge density using a filter above the ground plane, with the filter housing at space potential, is reported by Crozier [23]. However, details of the experimental arrangement are not provided. Extra ions which arrive at the aperture because of the electric field will not be measured if the filter element is adequately shielded by the filter housing. The electrical shielding can be checked by noting whether there is any ion current to the filter when M_o is zero.

1.8 Conclusion

This study, described in more detail elsewhere [2], has shown that the influence of a dc electric field on measurement of monopolar space charge densities with an ion counter can be made negligible when the measurements are performed in the ground plane, and oriented vertically or horizontally above the ground plane with an attractive potential applied to the ion counter housing. This assumes that the collecting electrode(s) in the ion counter is adequately shielded from the external electric field.

Measurements of net space charge density with a Faraday cage (not discussed in this report) appear to be significantly influenced by a large field except when the space charge is predominantly monopolar or when composed of large ions (aerosols) with small mobilities. The optimum configuration for the filter is an above-ground horizontal orientation with the filter housing at ambient space potential.

2. GASEOUS DIELECTRICS RESEARCH

Task 03
Richard J. Van Brunt, Sanjay V. Kulkarni (Guest Scientist), and James K. Olthoff
Electricity Division
National Institute of Standards and Technology

2.1 Introduction

The objectives of this project are the development of measurement capabilities and providing fundamental data as part of the Department of Energy's basic research concerned with the development and evaluation of advanced compressed-gas-insulation technology.

To reduce space requirements and improve the efficiency of high-voltage transmission systems, the electric power industry has turned toward more extensive use of compressed-gas insulation. To design meaningful tests of system performance and establish specifications for the quality of materials used in such systems, more information is needed about the fundamental physical and chemical processes which lead to insulation deterioration and electrical breakdown. The research includes applications of gas chromatography-mass spectrometry to characterize corona discharge by-products; and the acquisition of fundamental data, e.g., reaction-rate coefficients, corona-inception voltages, production rates of corona by-products, the effects of contaminants on discharge initiation, and the rates of discharge-induced decomposition of the gas.

This report highlights two significant technical activities. The first is concerned with measurement of collisional electron-detachment and ion-conversion cross sections for the interaction of the negative ions SF_6^-, SF_5^-, and F^- with SF_6 molecules. The measured cross sections were used to calculate electron-detachment and ion-conversion reaction rate coefficients which were in turn used in a model to interpret previous results of negative ion measurements in uniform-field drift tubes and investigations of electrical discharge initiation probabilities at relatively high pressures in SF_6 insulated power systems. The experimental part of this work was conducted in a collaboration with scientists in the Department of Physics, College of William and Mary, Williamsburg, Virginia. The results of this work have been accepted for publication in two archival papers [24, 25] and have also been presented in three recent conference publications [26–28].

The second major technical activity to be highlighted concerns the development of a new technique to measure the stochastic properties of pulsating corona or partial discharges. This technique is unique in that it allows direct measurement of various *conditional* pulse-height and pulse-time interval distributions that enable a quantitative determination of the degree of correlation among successive partial discharge pulses. A detailed description of the measurement system has been accepted for archival publication [29]. Results from application of this method to an investigation of the stochastic behavior of negative corona (Trichel) pulses in electronegative gas mixtures have been presented at three different technical conferences [30–32].

2.2 Collisional Electron-Detachment and Ion-Conversion Processes in SF_6

2.2.1 Introduction

It has long been hypothesized that collisional electron detachment from negative ions may be the cause of discharge initiation in SF_6-insulated high-voltage equipment. However, uncertainties continue to exist concerning the identities of the significant negative ions, and the magnitudes of the detachment cross sections and corresponding reaction coefficients. Discharge-inception studies, which usually assume that SF_6^- is the negative ion of interest, have predicted collisional-detachment cross sections of SF_6^- in SF_6 with thresholds ranging from 1 to 8 eV [33]. Collisional-detachment coefficients determined from low-pressure drift-tube experiments [34, 35] lie several orders of magnitude above those calculated from breakdown data [33], while exhibiting an unexplained pressure dependence. Additionally, evidence exists that the destruction of negative ions in SF_6 is dominated by collisional dissociation into ionic fragments [34, 36–40] or by charge-transfer processes rather than by the loss of an electron. However, the exact nature of these ion-conversion processes have not previously been determined.

In this report we summarize results from the first direct measurements of absolute cross sections for electron-detachment and ion-conversion processes involving interactions of SF_6^-, SF_5^-, and F^-, with SF_6. These cross sections are used to calculate electron-detachment and ion-conversion reaction coefficients as functions of electric field-to-gas density ratios (E/N) for the reactions listed in Table 1. We then discuss the relevance of these results to the interpretation of data from uniform-field drift-tube measurements and measurements of electrical-discharge initiation processes.

2.2.2 Cross Sections

Details of the experimental method used to measure the cross sections reported here are given elsewhere [25, 41], and will not be covered here. We shall focus here only on the results obtained for collisions of SF_6^-, SF_5^-, and F^- on the SF_6 target gas,

Table 1. Collisional processes for which cross sections have been presented in the present work

cross section (σ_i)	reaction
σ_1	$SF_6^- + SF_6 \rightarrow e^- + SF_6 + SF_6$
σ_2	$SF_5^- + SF_6 \rightarrow e^- + SF_5 + SF_6$
σ_3	$F^- + SF_6 \rightarrow e^- + F + SF_6$
σ_4	$SF_6^- + SF_6 \rightarrow F^- + SF_5 + SF_6$
σ_5	$SF_5^- + SF_6 \rightarrow F^- + SF_4 + SF_6$
σ_6	$SF_6^- + SF_6 \rightarrow SF_5^- + F + SF_6$
σ_7	$SF_6^- + SF_6 \rightarrow$ charge-transfer products $+ SF_6$
σ_8	$SF_5^- + SF_6 \rightarrow$ charge-transfer products $+ SF_5$
σ_9	$F^- + SF_6 \rightarrow F + SF_6^-$ (see ref. 35)

although measurements were also made using other target gases [25], namely He, Ne, Ar, Kr, and Xe.

The experimentally determined center-of-mass energy dependencies of the collisional electron-detachment cross sections, $\sigma_i(\epsilon_{cm})$ for SF_6^-, SF_5^-, and F^- on an SF_6 target are shown in Fig. 10. The thresholds for the "prompt" collisional electron-detachment processes

$$SF_6^- + SF_6 \longrightarrow \text{neutral products} + e^-$$

$$SF_5^- + SF_6 \longrightarrow \text{neutral products} + e^-$$

as indicated by the vertical arrows in Fig. 10, are seen to be quite high (approximately 90 eV in both cases), while F^- has a lower detachment threshold of about 8 eV. At center-of-mass collision energies below the indicated thresholds there is no evidence to suggest finite (non zero) values for the $\sigma_i(\epsilon_{cm})$'s. Similar high values for the collisional electron-detachment thresholds were found for collisions of SF_6^- and SF_5^- ions with rare gas targets [25]. The implication of these results as shown below is that prompt electron detachment from either SF_6^- or SF_5^- cannot be important for electrical discharge conditions because, even for the highest E/N values which could conceivably occur in a gas discharge gap, only an insignificant fraction of the negative ions could acquire a kinetic energy of 90 eV or more.

Cross sections for the ion-conversion processes (reactions (4)–(9)) listed in Table 1 are shown in Fig. 11 together with extrapolations down to the thresholds which are used in the calculation of corresponding rate coefficients. The bases for these extrapolations are discussed later. The solid symbols indicate cross sections due to collisional-induced-dissociation (CID) processes, and the open symbols indicate cross sections for charge-transfer processes (including charge-transfer decomposition). There is evidence that the charge-transfer process involving SF_6^- on SF_6 is predominately dissociative [42, 43], and that charge transfer involving F^- on SF_6 may lead to

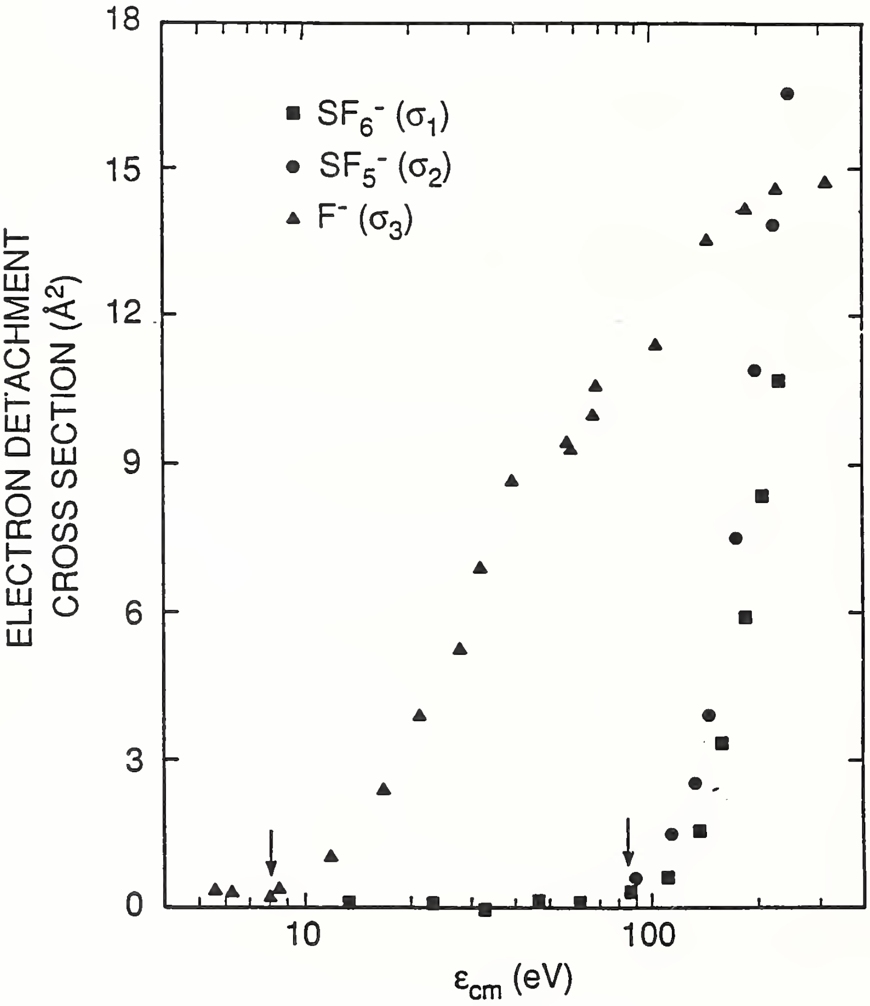

Figure 10. Collisional electron-detachment cross sections for F^-, SF_5^-, and SF_6^- on SF_6 target gas as a function of center-of-mass energy.

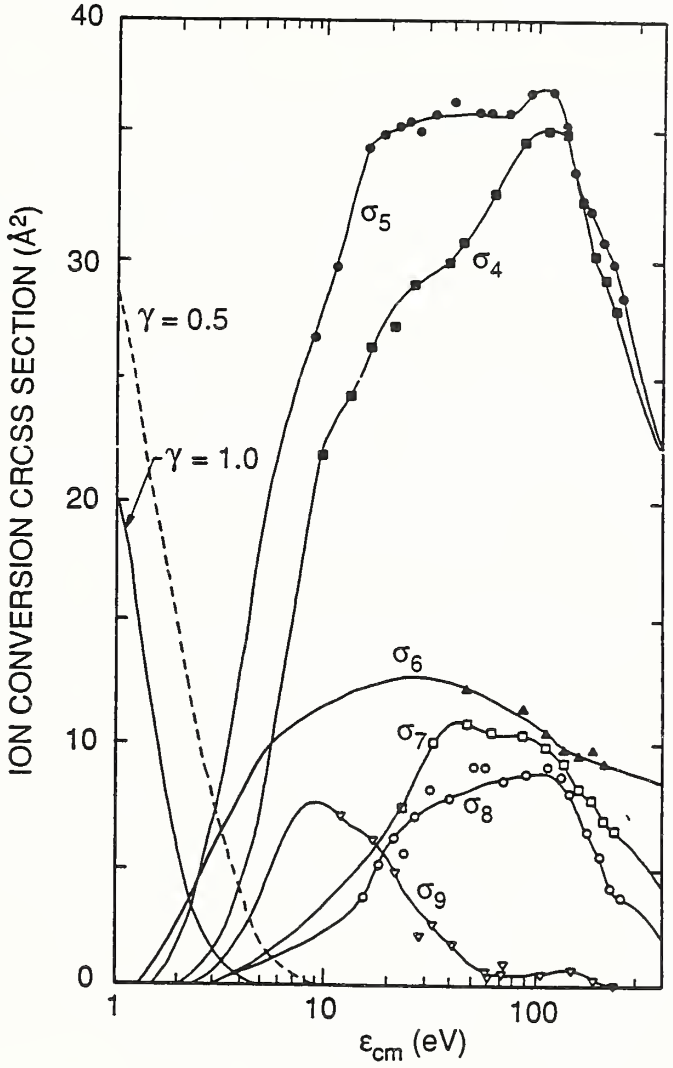

Figure 11. Measured cross sections for collision-induced ion-conversion processes in SF_6 target gas: (o) F^- from SF_5^-; (□) F^- from SF_6^-; (△)SF_5^- from SF_6^-; (o) ions due to charge-transfer reactions of SF_5^-; (□) ions due to charge-transfer reactions of SF_6^-; and (▽)ions due to charge-transfer reactions of F^-. The two exponentially-decaying curves on the left side of the figure represent the kinetic-energy distribution of Eq. (11) for $\gamma = 1.0$ and $\gamma = 0.5$ scaled relative to each other.

both SF_6^- and SF_5^- [34, 42]. It is interesting to note that the ion-conversion processes predominate for $\epsilon_{cm} < 200\,\mathrm{eV}$, i.e., upon collision of an SF_6^- or SF_5^- ion with SF_6, ion conversion is much more likely than electron detachment.

2.2.3 Reaction Rates and Coefficients

The analysis of rates for chemical processes in drift tubes or electrical discharges requires expressing inelastic-collision probabilities in terms of rate coefficients rather than cross sections. For a process where the projectiles have a velocity distribution, $f(v)$, the rate coefficient, k, is given by an averaging of the collision cross section over all velocities, namely

$$k = \int_0^\infty \sigma(v) v f(v) dv, \tag{7}$$

where $\sigma(v)$ is the velocity-dependent cross section for the process and $f(v)$ is subject to the normalization

$$\int_0^\infty f(v) dv = 1. \tag{8}$$

For measurements where charged particles are accelerated in a gas by an electric field (such as in a drift tube), the reaction coefficient, κ, is defined as the reaction probability per unit length in the direction of the electric field, and is related to the rate coefficient by

$$\frac{\kappa}{\mathrm{N}} = \frac{k}{v_d}, \tag{9}$$

where N is the target-gas number density and v_d is the charged particle drift velocity. For the special case of collisional electron detachment from a negative ion, the reaction coefficient is referred to as the detachment coefficient, δ (i.e. $\kappa/\mathrm{N} = \delta/\mathrm{N}$ for collisional electron detachment).

Reaction coefficients for detachment and ion-conversion processes involving SF_6^-, SF_5^-, and F^- in SF_6 can be derived from the measured cross sections, $\sigma_i(\epsilon_{cm})$, presented in Figs. 10 and 11 using

$$\frac{\kappa_i}{\mathrm{N}} = \frac{1}{m v_d} \int_0^\infty \sigma_i(\epsilon_L) f(\epsilon_L)\, d\epsilon_L, \tag{10}$$

where ϵ_L is the projectile energy in the lab frame, m is the mass of the negative ion, and $f(\epsilon_L)$ and $\sigma(\epsilon_L)$ are the ion kinetic-energy distribution and the process cross sections, respectively. The ion drift velocity is assumed to be given by $v_d = \mu \mathrm{E}$, where μ is the ion mobility and E is the applied electric-field strength.

It should be noted that the determination of reaction coefficients from collisional cross sections suffers from certain difficulties, the greatest arising from the assumed form of the ion kinetic-energy distribution, $f(\epsilon_L)$ [44]. While determination of ion kinetic-energy distributions has received considerable theoretical [45] and experimental [46] attention, the theoretical work is hampered by the lack of detailed ion-atom (or molecule) potential-energy surfaces and the experimental work suffers from a lack of reliability [44]. Accurate direct measurements of ion-velocity distributions have been demonstrated in recent optical-probing experiments, [47] but to date no experimental data are available for the kinetic-energy distributions of SF_6^-, SF_5^-, or F^- in SF_6.

In general, experimental work has indicated that ions with masses less than or equal to that of the molecules of the gas in which they are moving exhibit kinetic-energy distributions with high-energy tails [44, 48]. Differences in the velocity distributions at high energies in Eq. (10) will obviously have a large effect upon the calculated reaction coefficients derived from cross sections with threshold energies considerably in excess of the average ion kinetic energies.

An example of the large differences in calculated values of reaction coefficients which can occur when different energy distributions are assumed is shown in Fig. 12, where the collisional-detachment coefficient for F^- in SF_6 (δ_3) has been calculated as a function of E/N using the cross section data (σ_3) from Fig. 10 and several different indicated energy distributions. The solid lines in Fig. 12 represents detachment coefficients calculated using the kinetic-energy distribution of Kagan and Perel [33, 49],

$$f(\epsilon_L) = \frac{\sqrt{6\gamma}}{\pi v_d} \exp\left(\frac{-\gamma \epsilon_L}{\pi m v_d^2}\right), \tag{11}$$

which assumes that charge exchange is the dominant ion-molecule interaction. For the standard Kagan and Perel distribution, $\gamma = 1.0$. However, as will be discussed later, better agreement between ion-conversion reaction coefficients calculated here and those from analysis of drift-tube results is obtained by assuming $\gamma = 0.5$ which introduces a larger high-energy tail in the distribution.

The dashed line in Fig. 12 was obtained using a Maxwellian speed distribution [33] of the form,

$$f(\epsilon_L) = 3\sqrt{\frac{3m}{\pi}} \frac{\epsilon_L}{\bar{\epsilon}^{3/2}} \exp\left(\frac{-3\epsilon_L}{2\bar{\epsilon}}\right), \tag{12}$$

where the mean energy of the ion in the lab frame is given by [50]

$$\bar{\epsilon} = \frac{3kT}{2} + \frac{m}{2} v_d^2 + \frac{M}{2} v_d^2, \tag{13}$$

and M is the mass of the collision-gas molecules. This distribution has been used previously when analyzing discharge-inception data [33] and is similar to a strongly anisotropic velocity distribution derived by Skullerud [51] for ions drifting in a gas composed of molecules of the same mass as the ions under high electric fields.

In addition to the uncertainty associated with the assumed distribution function, another source of uncertainty in deriving reaction coefficients from cross-section data is the choice of experimentally determined values of ion mobilities (μ). Several previous mobility measurements [52–55] for SF_6^- and SF_5^- in SF_6 are not in complete

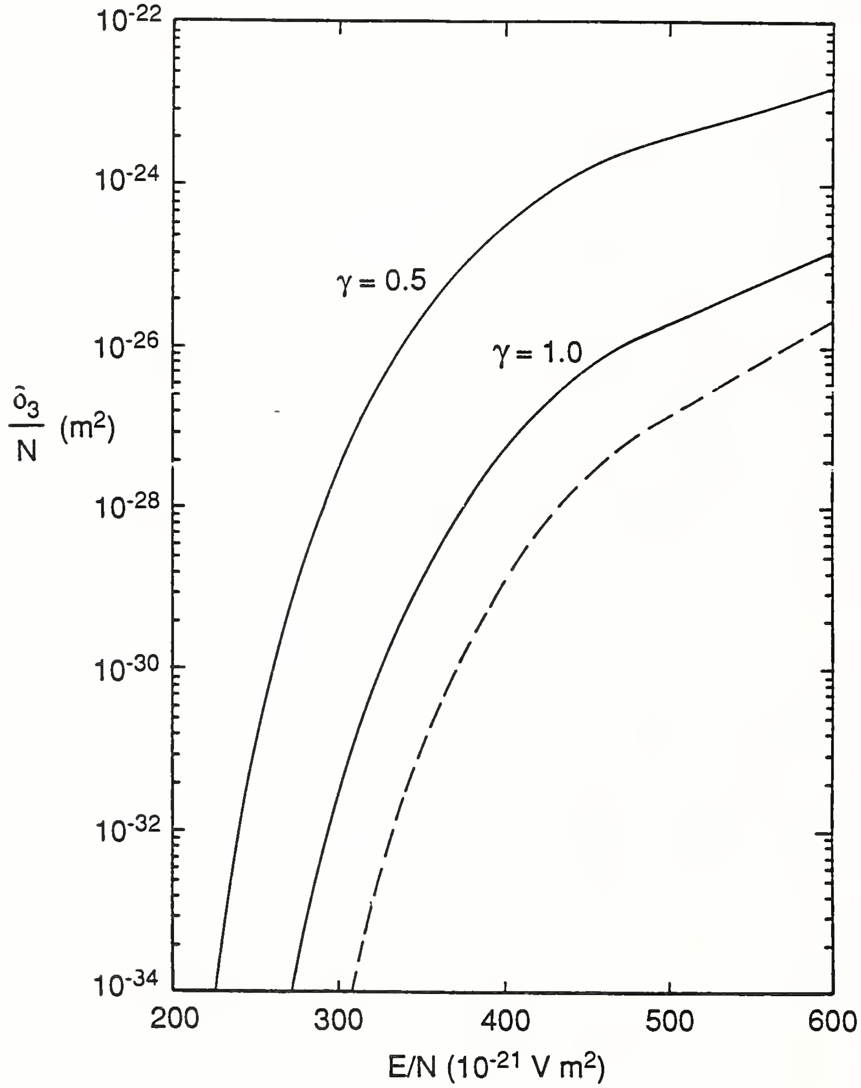

Figure 12. Calculated collisional electron-detachment coefficients for F^- on SF_6 gas using Eq. (10) and $\sigma_3(\epsilon_L)$, and assuming different ion kinetic-energy distributions: (——) Kagan and Perel; (- - -) Maxwellian.

agreement. However, uncertainties in calculated reaction coefficients using different mobilities are significantly smaller than the uncertainties due to the use of different energy distributions as discussed above. For the remainder of this paper, the mobilities used for SF_6^- and SF_5^- are those reported by Brand and Jungblut, [52] and for F^-, the values of Nakamura [55].

As expected, the extremely high apparent thresholds for prompt collisional electron detachment from SF_6^- and SF_5^- yield detachment coefficients from Eq. (10) that are insignificantly small in the E/N range of interest here. Simple estimates of these coefficients using a Kagan and Perel velocity distribution in Eq. (10) indicate that the detachment coefficients for SF_6^- and SF_5^- will be tens of orders of magnitude below the detachment coefficients determined in drift-tube experiments and the detachment coefficients calculated for F^- (Fig. 12). Thus one must conclude that prompt collisional electron-detachment processes for SF_6^- (and SF_5^-) in SF_6 cannot be significant reactions for production of electrons in discharge-inception processes, if, in fact, $\sigma_i(\epsilon_{cm})$ is zero below the apparent thresholds. It should be noted that this conclusion is independent of the assumed kinetic-energy distribution or the ion-mobility data used.

It is clear from Fig. 12, however, that collisional electron detachment from F^- in SF_6 is a significant process, thus suggesting that previously observed electron-detachment processes due to motion of negative ions in SF_6 are very likely from F^-. This agrees with earlier work [56] which indicated that detachment in SF_6 was predominately from F^-, and also with recent reanalysis of pulsed-electron avalanche experiments [57]. In fact, the observed threshold for electron detachment from F^- in SF_6 near 8 eV is consistent with the hypothesized thresholds predicted by discharge-inception experiments [33].

Other discharge-inception experiments have, however, suggested that negative cluster ions [58] involving H_2O or HF may be responsible for discharge initiation in SF_6. In fact, recent measurements [59] of negative ions produced in negative corona discharges, have indicated the presence of several types of cluster ions of the forms $F^-(HF)_n$, $OH^-(H_2O)_n$, and $SF_6^-(HF)$. Further investigations of the collisional detachment cross sections for these ions are necessary to determine their role in discharge initiation.

The conclusions drawn above depend upon the assumption that $\sigma(\epsilon_L) = 0$ at energies below the apparent threshold in Fig. 10. If one assumes that $\sigma(\epsilon_L) = 0.1\,\text{Å}^2$ (i.e., the experimental uncertainty) for energies which extend down to the thermodynamic threshold for electron detachment, then detachment coefficients for SF_6^- and SF_5^- are found to be of the same order of magnitude as those determined by drift-tube experiments. However, detachment coefficients derived with such an assumption are not compatible with previously observed pressure dependencies observed in drift-tube experiments [34, 35] as discussed in the next section.

In order to calculate the reaction coefficients for the ion-conversion processes listed in Table 1, it is necessary to extrapolate the measured cross sections down to assumed thresholds at lower energies. The extrapolations used for the subsequent calculations are shown in Fig. 11. These extrapolations were chosen to agree with known thermodynamic thresholds and to minimize the discrepancies with previously determined reaction coefficients as discussed below. The thresholds for production of F^- from SF_6^- and SF_5^- (σ_4 and σ_5) were determined to be 2.0 eV and 1.5 eV, respectively, by using the observed thresholds for F^- production from collisions of SF_6^- and SF_5^- with the rare-gas targets [25]. The cross sections for SF_5^- production (σ_6) from SF_6^- were extrapolated down to the thermodynamic threshold of 1.35 eV. For the charge-transfer reaction involving F^- and SF_6, the cross sections were extrapolated down to the thermodynamic threshold of 2.25 eV under the assumption that the primary product is SF_6^-. The other charge-transfer cross sections (σ_7 and σ_8) were both extrapolated down to a threshold near 3 eV which corresponds to the thermodynamic threshold for a symmetric charge transfer between SF_6^- and SF_6 as suggested by Hay [60]. There is a large uncertainty in these last assumed thresholds since the identity of the charge-transfer products in these processes are indistinguishable in the present experiment.

The calculated reaction coefficients for processes 5, 6 and 9 of Table 1 are shown in Figs. 13, 14, and 15 respectively, along with reaction coefficients for the same reactions as determined by previous drift-tube experiments. The solid lines represent the coefficients calculated using the standard Kagan and Perel distribution (i.e. $\gamma = 1$) shown in Eq. (11). Note that these calculated reaction coefficients all fall substantially below those determined previously despite the fact that the extrapolated thresholds for these cross sections were all assumed to be thermodynamic thresholds. Any reasonable change in the assumptions concerning the reaction thresholds or the behavior of the cross sections near threshold would necessarily cause the reaction coefficients to be even smaller, thus implying that the discrepancies cannot be resolved by changing the assumed cross-section thresholds or extrapolations.

Despite the fact that the Kagan and Perel distribution produces the largest coefficients of any of the commonly used ion kinetic-energy distributions, better agreement can be obtained between our calculated coefficients and those from previous experiments if one assumes that the kinetic-energy distribution has a longer high-energy tail, in agreement with the previous discussion of kinetic-energy distributions. The Kagan and Perel distribution in Eq. (11) can be conveniently altered by allowing γ to vary between 0 and 1. The dashed lines in Figs. 13 to 15 represent reaction coefficients calculated with $\gamma = 0.5$, while in Fig. 11 the relative magnitudes of the two distributions ($\gamma = 1$ and $\gamma = 0.5$) are shown for comparison.

Obviously, the curves in Figs. 13–15 with $\gamma = 0.5$ are in better agreement with the previously reported coefficients than are the curves calculated using $\gamma = 1$. This may

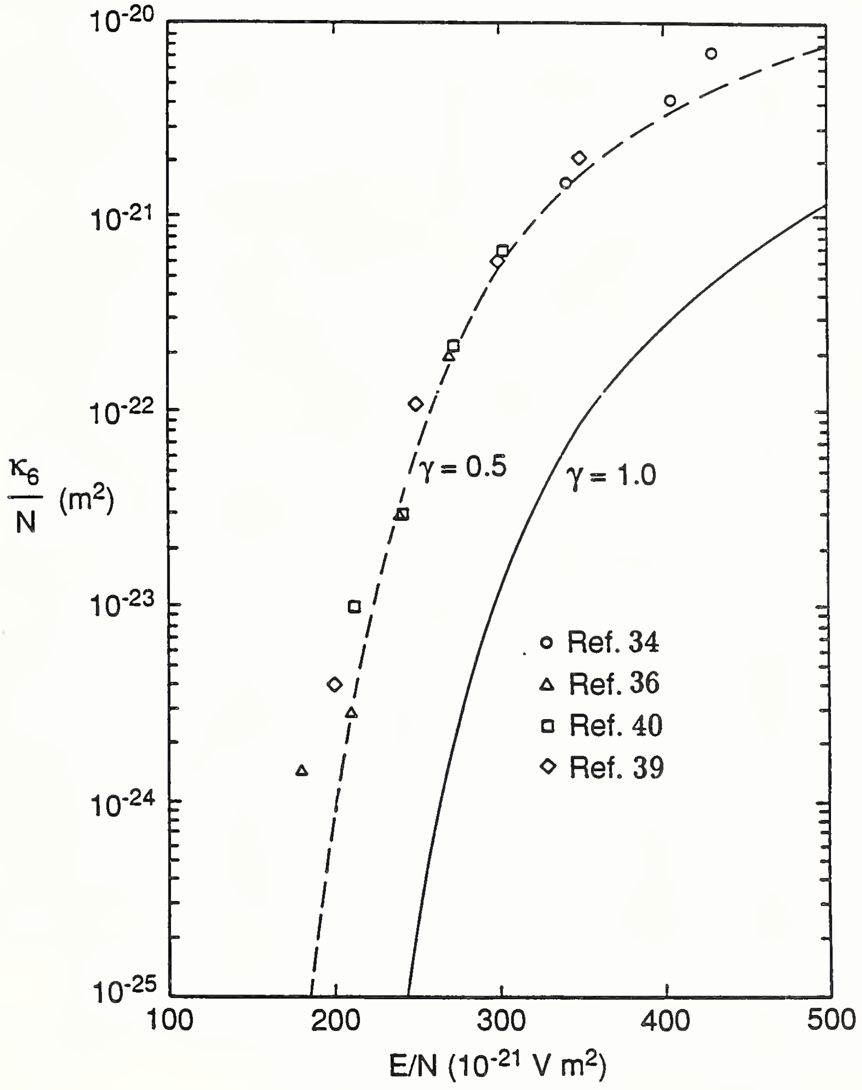

Figure 13. Calculated reaction coefficients for the reaction $SF_6^- + SF_6 \longrightarrow SF_5^- + F + SF_6$ using measured cross-section data $\sigma_6(\epsilon_L)$ and a Kagan and Perel energy distribution. The symbols are previously calculated reaction coefficients for the same process derived from uniform-field drift-tube data.

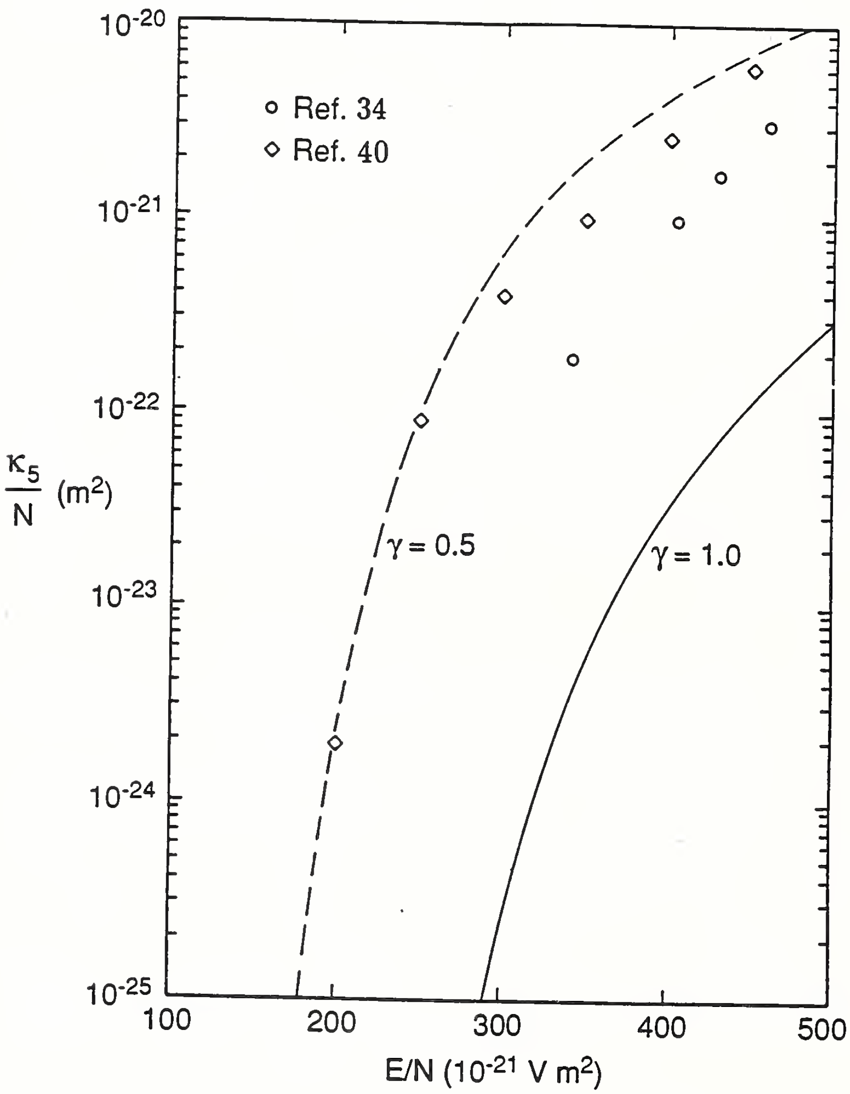

Figure 14. Calculated reaction coefficients for the reaction $SF_5^- + SF_6^- \longrightarrow F^- + SF_4 + SF_6$ using measured cross-section data $\sigma_5(\epsilon_L)$ and a Kagan and Perel energy distribution. The symbols are previously calculated reaction coefficients for the same process derived from uniform-field drift-tube data.

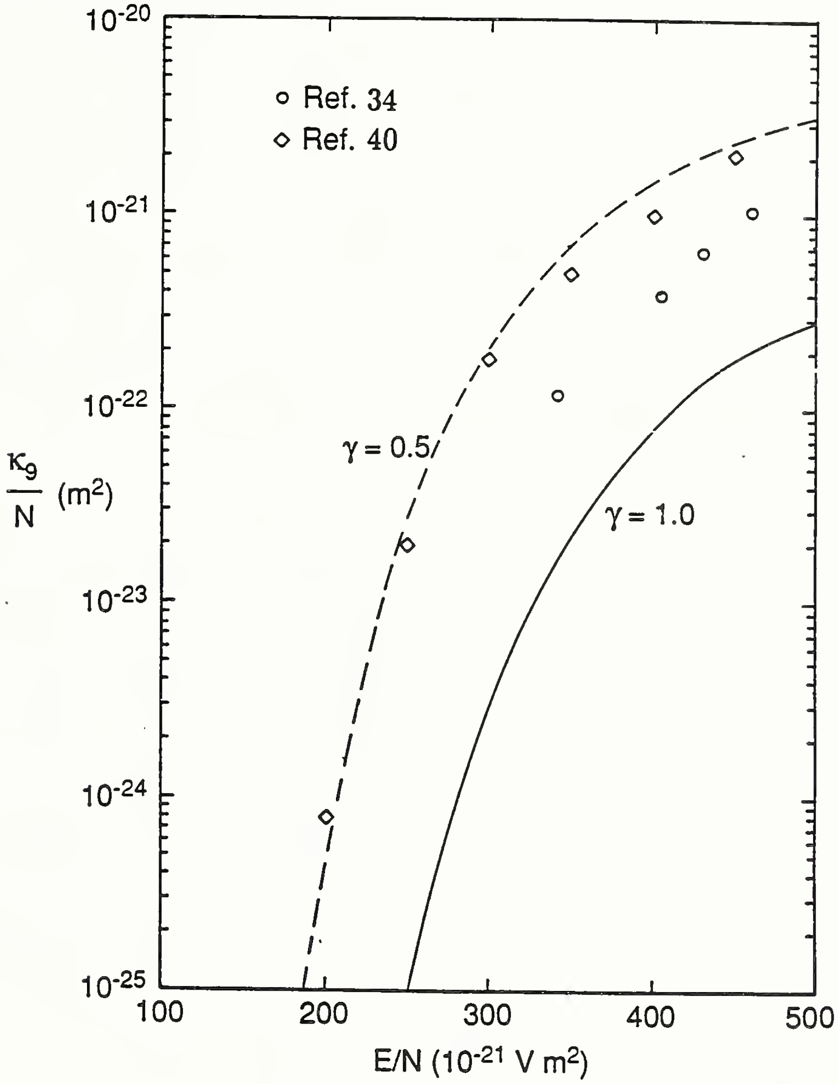

Figure 15. Calculated reaction coefficients for the reaction $F^- + SF_6 \longrightarrow F + SF_6^-$ using measured cross-section data $\sigma_9(\epsilon_L)$ and a Kagan and Perel ion kinetic-energy distribution. The symbols are previously calculated reaction coefficients for the same process derived from uniform-field drift-tube data.

indicate that previously assumed energy distributions need to be modified [33, 35]. However, one must note that the reaction coefficients derived from drift-tube data are model dependent and that only reactions 5, 6, and 9 (table 1) are assumed in the previous analysis of data from drift tubes. Thus discrepancies may also arise because this commonly used model does not consider the collision-induced dissociation of SF_6^- into $F^- + SF_5$ (reaction 4). This reaction is found here to be significant (see Fig. 11) and its omission may produce errors in the reaction rates derived from drift-tube data.

The calculated reaction coefficients for reaction 4 (and for reactions 7 and 8) are shown in Fig. 16 using Kagan and Perel distributions with $\gamma = 1.0$ and 0.5. As stated before, no previously determined coefficients for these processes exist for comparison.

2.2.4 Model for Electron Detachment from Ion Drift in SF_6

A different interpretation of the processes which lead to detachment coefficients derived from drift-tube data [34, 35] and their observed pressure dependence can be obtained if one assumes that electron production in a drift tube is not due primarily to prompt electron detachment from SF_6^-, but arises from either detachment from F^- or from collisionally-excited, energetically-unstable $(SF_6^-)^*$ ions as suggested by the previously presented data. A model can then be developed which assumes that under drift-tube conditions, prompt detachment from SF_5^- and SF_6^- is insignificant, and that a steady state condition exists for intermediate products (i.e. $d[SF_5^-]/dt = d[F^-]/dt = d[(SF_6^-)^*]/dt = 0$). If one analyzes the drift-tube data as done previously [34, 35], assuming that all ejected electrons come from SF_6^- ions, then the measured electron-production rate can be written in terms of an "effective" detachment coefficient (δ_{eff}) according to the expression

$$\frac{d[\mathrm{e}]}{dt} = v_d \left(\frac{\delta_{\text{eff}}}{\mathrm{N}}\right) \mathrm{N}[\mathrm{SF}_6^-], \tag{14}$$

where [e] is the number of free electrons produced per unit volume which can be detected, v_d refers specifically to the drift velocity of SF_6^- in SF_6, and δ_{eff}/N is determined by analysis of drift-tube data [34, 35]. Assuming that the simplified set of processes indicated in Table 2 dominate in a drift tube, an expression for δ_{eff}/N, can be found in terms of the relevant rate coefficients by solving the set of coupled rate equations. The result is

$$k_{\text{eff}} = v_d \left(\frac{\delta_{\text{eff}}}{\mathrm{N}}\right) = k_3 \left(\frac{k_6 + k_4}{k_9 + k_3}\right) + k_{12} \left(\frac{k_{10}}{k_{12} + k_{11}\mathrm{N}}\right). \tag{15}$$

The effective detachment coefficient given by Eq. (15) is seen to consist of two terms, a pressure-independent term which depends upon various ion-conversion and direct-detachment processes involving F^-, and a pressure-dependent term which depends

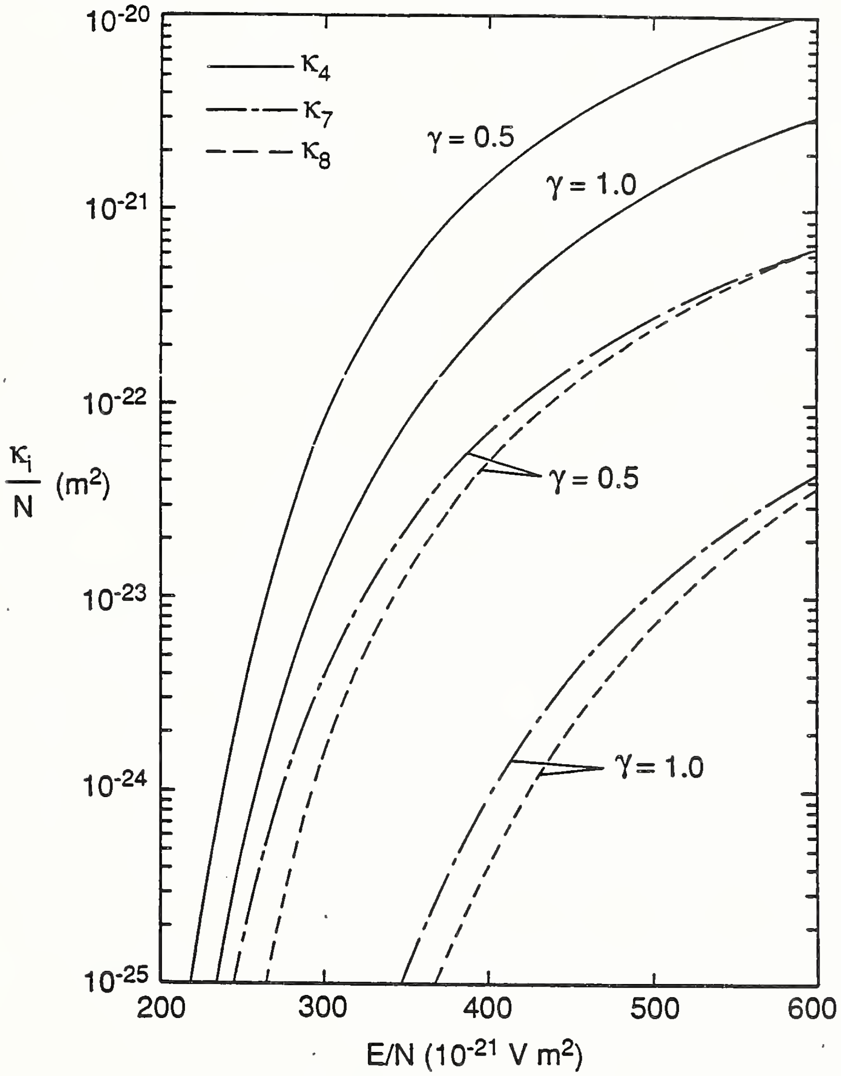

Figure 16. Calculated reaction coefficients using a Kagan and Perel ion kinetic-energy distribution for the following reactions: (——) $SF_6^- + SF_6 \longrightarrow F^- + SF_5 + SF_6$; (— · —) $SF_6^- + SF_6 \longrightarrow$ charge-transfer products; and (- - -) $SF_5^- + SF_6 \longrightarrow$ charge-transfer products.

Table 2. Proposed ion-molecule reactions for drift-tubes containing SF_6

$SF_6^- + SF_6 \longrightarrow SF_5^- + F + SF_6$	k_6	Dissociative Ion Conversion
$SF_6^- + SF_6 \longrightarrow F^- + SF_5 + SF_6$	k_4	
$SF_5^- + SF_6 \longrightarrow F^- + SF_4 + SF_6$	k_5	
$F^- + SF_6 \longrightarrow F + SF_6^-$	k_9	Charge Transfer
$F^- + SF_6 \longrightarrow \mathrm{neutrals} + e^-$	k_3	e^- Detachment
$SF_6^- + SF_6 \longrightarrow (SF_6^-)^* + SF_6$	k_{10}	Excitation
$(SF_6^-)^* + SF_6 \longrightarrow SF_6^- + SF_6$	k_{11}	De-excitation
$(SF_6^-)^* \longrightarrow SF_6 + e^-$	k_{12}	Auto-detachment

upon the rates for collisional relaxation, excitation and auto-detachment of $(SF_6^-)^*$. This expression is more complex than those previously derived [33–35] which assume that direct detachment from SF_6^- was the sole source of electrons.

If $k_{11}N$ is approximately the collision frequency of SF_6^- in SF_6 (e.g., $\sim 10^8$/sec at 1 kPa) and k_{12} is on the order of the inverse of the excited-state lifetime ($\tau \sim 10\mu s$ to 2 ms), [61] then $k_{11}N >> k_{12}$ and the model predicts an inverse pressure dependence for δ_{eff}/N at low N. This inverse pressure dependence is consistent with previous drift-tube measurements [34, 35]. O'Neill and Craggs [34] also report no detachment from F^- or SF_5^- at low pressures in agreement with the dominance of the second term of Eq. (15) for smaller N. The model proposed here is consistent with the observed [35] variations in δ_{eff}/N with the "age" of the SF_6^- ions if a substantial fraction of SF_6 anions are initially in excited energetically-unstable autodetaching states.

At higher pressures, the first term on the right side of Eq. (15) dominates, giving a δ_{eff}/N that is essentially pressure independent. In this pressure regime, electron production involves mainly process (3) with a threshold of 8 eV. These results are consistent with: 1) the lack of pressure dependence [33, 57] for δ_{eff}/N suggested from the analysis of high-pressure electrical discharge initiation data, and 2) previously discussed results [56] suggesting detachment in SF_6 is predominately from F^-.

Ideally, one would like to calculate the effective detachment coefficients using Eq. (15) to compare with the previously determined drift-tube measurements. However, values for k_{10}, k_{11} and k_{12} are not available, so only the contribution to δ_{eff}/N from the first term of Eq. (15) can be calculated using the reaction coefficients derived above. The solid curve in Fig. 17 shows the contribution from the first term of Eq. (15) using a Kagan and Perel distribution with $\gamma = 1.0$. Note that the magnitude of the solid curve is similar to that of the effective detachment coefficient derived from discharge-inception experiments [33] (dot-dashed curve) but is substantially smaller than the coefficients derived from drift-tube experiments [34, 35] (symbols). If one uses the reaction coefficients derived with a Kagan and Perel energy distribution for $\gamma = 0.5$

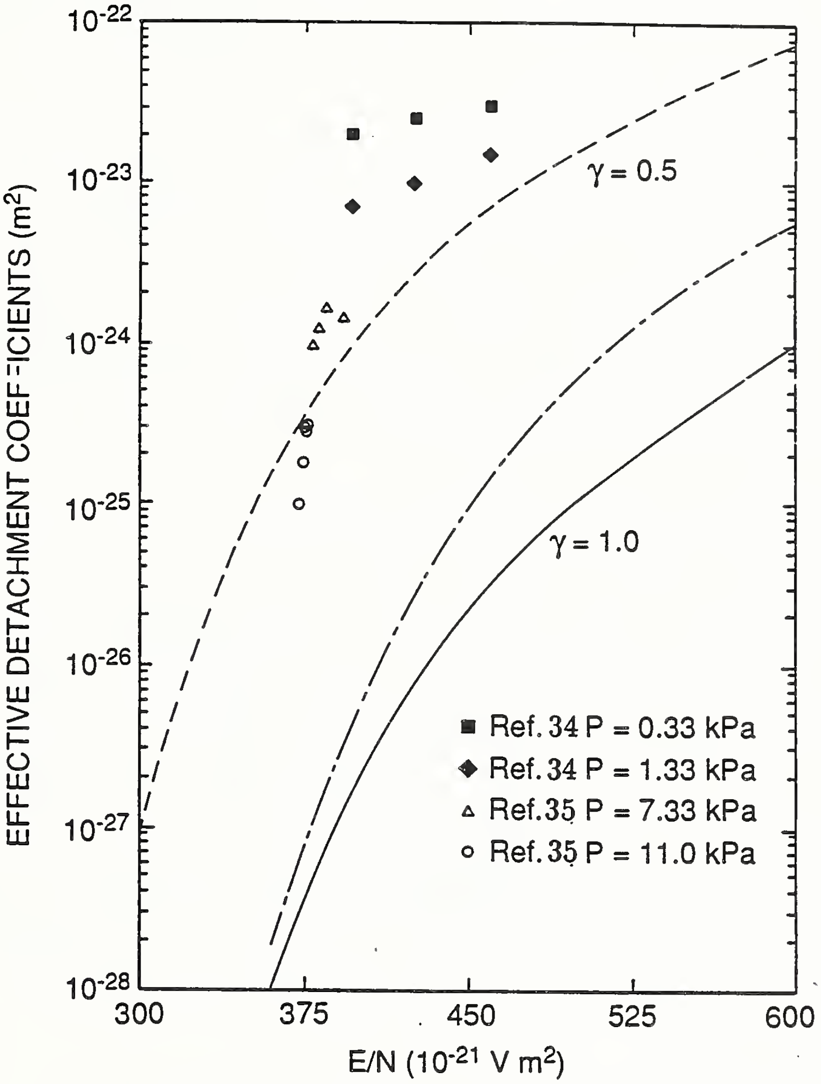

Figure 17. Effective detachment coefficients determined from drift-tube experiments at different pressures are shown as identified by the symbols in the key. Effective detachment coefficients calculated from discharge-inception data from Ref. [33] are also shown (— · —). The contribution to the effective detachment coefficients from the first term of Eq. (15) are shown for $\gamma = 1.0$ (——) and for $\gamma = 0.5$ (- - -).

(dashed curve), then the $\delta_{\rm eff}/N$ derived from the first term of Eq. (15) becomes of the same order of magnitude as the coefficients derived from the highest pressure drift-tube experiments. The fact that the dashed curve actually lies above the smallest measured drift-tube values indicates that taking $\gamma = 0.5$ may overestimate the high-energy tail for the kinetic-energy distribution.

It is also important to note that the above model gives a reasonable pressure dependence for $\delta_{\rm eff}/N$ without invoking "stabilization" of SF_6^- via $(SF_6)SF_6^-$ dimer formation as proposed by Hansen et al. [35] Dimer formation is irrelevant here because: 1) it was introduced to compete with the direct SF_6^- collisional-detachment process, which is of doubtful significance and, 2) as can be shown, it cannot yield the observed pressure dependence. There are also data which suggest that $(SF_6)SF_6^-$ formation is very slow [54] and decreases with increasing E/N [62].

2.2.5 Conclusions

The measured cross sections for collisional electron detachment and ion conversion of negative ions in SF_6 have been used in a theoretical model which invokes detachment from long-lived, energetically-unstable states of collisionally excited SF_6^- to explain the pressure dependence of previously measured detachment coefficients and the high apparent detachment thresholds implied by analysis of breakdown-probability data for SF_6. The model suggests that measured effective detachment coefficients depend upon many different reactions rates, thus implying that detachment processes in SF_6 are more complex than previously assumed. At high pressures, measured detachment coefficients appear to depend primarily upon the rates for ion-conversion and direct-detachment processes involving F^-, consistent with earlier suggestions.

2.3 Stochastic Properties of Partial Discharges

2.3.1 Introduction

Pulsating electrical discharge phenomena such as corona or partial-discharge pulses that occur in highly nonuniform electric fields are generally stochastic processes in the sense that when a discharge pulse ceases it leaves behind an imprint that can influence development of the subsequent discharge pulse. This imprint may, for example, be in the form of a negative-ion space-charge moving in the gas, molecules in excited metastable states, or charges on surfaces. It is therefore the nature of the phenomenon that significant correlations can exist between successive discharge pulses, e.g., one cannot assume that pulse amplitude and time separation from the previous pulse will be independent random variables.

An indication of the stochastic behavior of partial discharge pulses is not readily obtained from present commonly used measurement methods. Earlier partial-discharge measurement schemes utilizing electrical detection have been limited to either discharge pulse-height analysis [63–65], pulse-frequency or period measurements [65–67], or broad-band pulse-shape determinations [68–70], none of which give any indication of the stochastic nature of the phenomenon. A meaningful interpretation of discharge pulse-height distributions often used for evaluating insulation performance is impossible without information about the degree of correlation among successive pulses.

An electrical method of discharge pulse measurement is described here from which direct experimental determinations of a set of various conditional pulse-height and time-separation probability distributions can be made. As will be shown here, these distributions provide a quantitative indication of the degrees of correlation among successive pulses that allow one to evaluate the extent to which the occurrence of any discharge pulse affects the development of subsequent pulses. Examples are shown of data obtained by this method for Trichel pulses [71, 72] in air, N_2/O_2 and SF_6/O_2 gas mixtures. The results clearly demonstrate a high degree of correlation among successive discharge pulses as indicated for example by a strong dependence of discharge pulse amplitude on time separation from the previous pulse. The observed stochastic behavior is consistent with current physical descriptions of the Trichel-pulse phenomenon [72–74], and illustrates the difficulties that can be encountered in attempting to understand measured pulse-height distributions without information about correlation effects [75].

The measurement system described here should be applicable to investigations of the stochastic behavior in other types of pulsating electrical discharge phenomena. Clear evidence of successive discharge pulse correlations are found, for example, in the operation of Geiger counters [76], prebreakdown current in dielectric liquids [77], and for positive burst-type corona in electronegative gases [64]. Partial discharge pulses in cavities [78] within solid insulating materials should also be inherently stochastic since the occurrence of a discharge pulse will invariably leave behind charged surfaces in the cavity which reduce the local electric field below the critical value required to sustain a discharge. Some dissipation of this surface charge will then be required before another partial discharge pulse can develop. The development of a discharge pulse will therefore be affected by residual surface charges from previous pulses. Similar arguments might apply to pulsating dielectric barrier discharges such as used for ozone generation [79].

A detailed description of the measurement system and associated electronic circuitry is given elsewhere [29] and will not be covered here. In this report we consider only the basic theory of the measurement concept with a brief description of the system. Examples of results obtained for pulsating negative corona discharges (Trichel pulses) in electronegative gas mixtures can also be found in Ref's [30–32].

Table 3. Conditional pulse-height and time-separation distributions up to order 2

$$\begin{array}{c}\text{0th}\\\text{Order}\end{array}\left\{\begin{array}{l} p_0(q_i) \\ \\ p_0(\Delta t_i) \end{array}\right\}_{i>0} \qquad \begin{array}{c}\text{1st}\\\text{Order}\end{array}\left\{\begin{array}{ll} p_1(q_i\,|\,\Delta t_{i-j-1}) & p_1(\Delta t_i\,|\,q_{i-j}) \\ \\ p_1(q_i\,|\,q_{i-j-1}) & p_1(\Delta t_i\,|\,\Delta t_{i-j-1}) \end{array}\right\}_{i>2,i\geq j\geq 0}$$

$$\begin{array}{c}\text{2nd}\\\text{Order}\end{array}\left\{\begin{array}{ll} p_2(q_i\,|\,\Delta t_{i-j-1},q_{i-k-1}) & p_2(q_i\,|\,\Delta t_{i-j-1},\Delta t_{i-\ell-1}) \\ \\ p_2(q_i\,|\,q_{i-j-1},q_{i-\ell-1}) & p_2(\Delta t_i\,|\,\Delta t_{i-j-1},q_{i-k}) \\ \\ p_2(\Delta t_i\,|\,\Delta t_{i-j-1},\Delta t_{i-\ell-1}) & p_2(\Delta t_i\,|\,q_{i-j},q_{i-\ell}) \end{array}\right\}_{i>2,i\geq j\geq 0,i\geq k\geq 0,i\geq \ell\geq 0,\ell\neq j}$$

2.3.2 Theory

In this section we define the various conditional pulse-height and time-interval distributions that can be measured by the method described here and indicate how they can be used to determine the degree of correlation among successive discharge pulses. The basic theory of conditional probabilities upon which the following discussion is based can be found in several texts (see for example Ref's [80] and [81]).

The variables of particular interest here are: 1) the discharge pulse magnitude, q_n, as measured by its amplitude expressed in units of picocoulombs (pC) and 2) the time separation between successive pulses, Δt_n, as measured in microseconds (μs). It is assumed that the discharge phenomenon consists of a finite sequence of m pulses denoted by the set of pulse amplitudes and corresponding time separations $\{q_1, q_n, \Delta t_{n-1}\}_m$, where $n = 2, 3, \ldots, m$ and $m \gg 1$. The time separation, Δt_n, is measured between the nth and $(n+1)$st pulses.

The complete sets of possible conditional pulse-height and time-interval probability distribution functions, up to second order, are given in Table 3. The 0th order functions are obviously unconditional and defined such that, for example, $p_o(q_n)dq_n$ is the probability that any discharge pulse occurs with amplitude in the range q_n to $q_n + dq_n$ independent of n. The distributions p_1 and p_2 are conditional, e.g., $p_1(q_n \mid \Delta t_{n-1})dq_n$ is the probability that the nth discharge pulse for arbitrary n will have an amplitude between q_n and $q_n + dq_n$ when its time separation from the preceding pulse is restricted to the value Δt_{n-1}, and $p_2(q_n|\Delta t_{n-1}, q_{n-1})dq_n$ is the same with the added restriction that the amplitude of the preceding pulse is also fixed at a value q_{n-1}. It should be noted that a somewhat simplified notation is used here for probability distribution functions which differs from that often used in standard texts (see the comment attached to Ref. [80]). It must also be emphasized that since there is no way to select particular values for n in the present measurement system, all measured distributions apply only for arbitrary values of n.

For the pulsating type of electrical-discharge phenomenon under consideration here, q_n and Δt_n may not always be independent random variables. An immediate indication that these variables are not independent can be obtained from a discovery that a measured conditional probability distribution is not equal to the corresponding unconditional distribution, e.g., if it is found that $p_1(q_n \,|\, \Delta t_{n-1})dq_n \neq p_0(q_n)dq_n$ for all allowed Δt_{n-1} such that $p_0(\Delta t_{n-1}) \neq 0$, then q_n and Δt_{n-1} are dependent random variables, and a correlation must exist between pulse amplitude and time separation from the previous pulse. A measure of the degree of correlation between two quantities such as q_n and Δt_{n-1} can be found by computing the appropriate correlation coefficient. For the case of the variables q_n and Δt_{n-1}, the correlation coefficient, $R_{q_n,\Delta t_{n-1}}$, is defined by [81]

$$R_{q_n,\Delta t_{n-1}} = \frac{S_{q_n,\Delta t_{n-1}}}{\left[S_{q_n} S_{\Delta t_{n-1}}\right]^{1/2}}, \tag{16}$$

where

$$S_{q_n} = \int_0^\infty p_0(q_n)(q_n - \overline{q}_n)^2 \, dq_n \tag{17}$$

$$S_{\Delta t_{n-1}} = \int_0^\infty p_0(\Delta t_{n-1})(\Delta t_{n-1} - \overline{\Delta t_{n-1}})^2 \, d(\Delta t_{n-1}) \tag{18}$$

$$S_{q_n,\Delta t_{n-1}} = \int_0^\infty \int_0^\infty p_0(\Delta t_{n-1}) p_1(q_n \,|\, \Delta t_{n-1})(q_n - \overline{q}_n)(\Delta t_{n-1} - \overline{\Delta t_{n-1}}) \, dq_n \, d(\Delta t_{n-1}) \tag{19}$$

$$\overline{q}_n = \int_0^\infty p_0(q_n) q_n \, dq_n \tag{20}$$

$$\overline{\Delta t_{n-1}} = \int_0^\infty p_0(\Delta t_{n-1}) \Delta t_{n-1} \, d(\Delta t_{n-1}). \tag{21}$$

Equations (17) and (18) represent the variances of q_n and Δt_{n-1} respectively and Eq (19) gives the covariance of these variables. The correlation coefficient has the property that

$$1 \geq \mid R_{q_n,\Delta t_{n-1}} \mid, \tag{22}$$

where if $R_{q_n,\Delta t_{n-1}} = 0$, then the random variables q_n and Δt_{n-1} are uncorrelated. The correlation coefficient can be computed from Eq's (16)-(21) using the measured distributions $p_0(q_n)$, $p_0(\Delta t_{n-1})$, and $p_1(q_n \,|\, \Delta t_{n-1})$. It should be noted that Eq (20) gives the mean pulse height and Eq (21) the mean time interval from which a repetition rate, $1/\overline{\Delta t_{n-1}}$, can be determined. Both of these quantitites are often obtained directly from existing partial-discharge measurement systems [65].

The probability that the nth pulse in a chain of pulses will have a particular amplitude or time separation from a preceding pulse may depend in general on the amplitudes and time separations of all preceding pulses. For example, the probability that a sequence of pulses represented by the set $\{q_j, \Delta t_j\}_{n-1}$, $j = 1, 2, \ldots, n-1$, will be followed by a pulse with amplitude between q_n and $q_n + dq_n$ is given by the following product of conditional probability functions:

$$\begin{aligned} &p(q_n, \{q_j, \Delta t_j\}_{n-1}) \prod_{j=1}^{n-1} dq_j d(\Delta t_j)\, dq_n = p_0(q_1) p_1(\Delta t_1 \,|\, q_1) p_2(q_2 \,|\, \Delta t_1, q_1) \times \\ &p_3(\Delta t_2 \,|\, q_2, \Delta t_1, q_1) \cdots p_{2n-3}(\Delta t_{n-1} \,|\, q_{n-1}, \{q_j, \Delta t_j\}_{n-1}) \prod_{j=1}^{n-1} dq_j d(\Delta t_j)\, dq_n = \qquad (23) \\ &p_0(q_1) \prod_{j=1}^{n-1} p_{2j}(q_{j+1} \,|\, \{q_i, \Delta t_i\}_j) p_{2j-1}(\Delta t_j \,|\, q_j, \{q_i, \Delta t_i\}_{j-1}) dq_j d(\Delta t_j)\, dq_n \end{aligned}$$

where, for example, $p_{2j}(q_{j+1} \mid \{q_i, \Delta t_i\}_j)$ is the $2j$th order conditional distribution of amplitudes for the $(j+1)$st pulse when the amplitudes and corresponding time separations for all previous pulses have fixed values given by the set $\{q_i, \Delta t_i\}_j$.

If the discharge pulse sequence is jointly a Markov process [80] for the variables q_n and Δt_{n-1} in the sense that all pulses in the sequence are correlated only with their immediate predecessors, then the right hand side of Eq (24) simplifies to:

$$p_0(q_1) p_1(\Delta t_1 \,|\, q_1) \prod_{j=2}^{n-1} p_2(\Delta t_j \,|\, q_j, \Delta t_{j-1}) p_2(q_j \,|\, \Delta t_{j-1}, q_{j-1}) dq_j d(\Delta t_j) dq_n. \qquad (24)$$

An indication of whether or not an observed pulsating discharge phenomenon behaves like a Markov process can be obtained by the measurement system described here which allows determination of the conditional probability distributions $p_1(q_n \,|\, \Delta t_{n-j})$ for $n > j = 1, 2, 3$.

If the pulse sequence is a Markov process, then it is required that

$$p_1(q_n \,|\, \Delta t_{n-j}) = p_0(q_n), \qquad (25)$$

for all allowed Δt_{n-j}, $j \geq 2$, such that $p_0(\Delta t_{n-j}) \neq 0$. For most partial discharge or pulsating corona-discharge phenomena, it can be expected that correlations between adjacent pulses will overwhelmingly predominate so that to a good approximation these phenomena behave like Markov processes. This is found to be the case for Trichel-pulse discharges in gases which will be considered later as an example of an application of the method introduced here.

Independent of whether or not the assumption of a Markov process applies, it is necessary that the measured distributions satisfy the following integral relationships [80]

$$p_0(q_n) = \int_0^\infty p_0(\Delta t_{n-1}) p_1(q_n \,|\, \Delta t_{n-1})\, d(\Delta t_{n-1}) \qquad (26)$$

$$p_0(q_n) = \int_0^\infty \int_0^\infty p_0(q_{n-1})p_1(\Delta t_{n-1}\,|\,q_{n-1})p_2(q_n\,|\,\Delta t_{n-1}, q_{n-1})\,dq_{n-1}\,d(\Delta t_{n-1}) \tag{27}$$

$$p_0(\Delta t_n) = \int_0^\infty p_0(q_n)p_1(\Delta t_n\,|\,q_n)\,dq_n \tag{28}$$

$$p_1(q_n\,|\,\Delta t_{n-1}) = \int_0^\infty p_0(q_{n-1})p_1(\Delta t_{n-1}\,|\,q_{n-1})p_2(q_n\,|\,\Delta t_{n-1}, q_{n-1})\,dq_{n-1}, \tag{29}$$

which follow from the law of total probabilities. If, for example, measurements are made of the three distributions $p_0(q_n)$, $p_0(\Delta t_n)$, and $p_1(q_n\,|\,\Delta t_{n-1})$, then it is desirable to perform the integration indicated in Eq (26) to show that it agrees with the measured $p_0(q_n)$ and therefore that the data on the measured distributions are self consistent.

With the system described here it is also possible to measure the conditional probability distribution $p_1(q_n\,|\,\Delta t_{1,2})$ not indicated in Table 3, where $\Delta t_{1,2} = \Delta t_{n-1} + \Delta t_{n-2}$. This distribution satisfies the condition

$$p_1(q_n\,|\,\Delta t_{1,2}) = C\int_0^{\Delta t_{1,2}} p_0(\Delta t_{1,2} - \tau)p_1(\tau\,|\,\Delta t_{1,2} - \tau)p_2(q_n\,|\,\Delta t_{1,2} - \tau, \tau)\,d\tau, \tag{30}$$

where p_1 and p_2 in the integral correspond respectively to $p_1(\Delta t_{n-1}\mid\Delta t_{n-2})$ and $p_2(q_n\,|\,\Delta t_{n-2}, \Delta t_{n-1})$ obtained from Table 3 and $C \equiv p_0(\Delta t_{1,2})$ is constant for each $\Delta t_{1,2}$ which, although it is not directly measured by the present method, is of no relevance since only the *profiles* of arbitrarily normalized $p_1(q_n\,|\,\Delta t_{1,2})$ are to be compared with integrals on the right-hand side. If it can be assumed that the phenomenon is a Markov process, then

$$p_2(q_n\,|\,\Delta t_{1,2} - \tau, \tau) = p_1(q_n\,|\,\tau), \tag{31}$$

for all allowed $\Delta t_{1,2}$. If correlations between successive time intervals Δt_{n-1} and Δt_{n-2} are also found to be weak such that

$$p_1(\tau\,|\,\Delta t_{1,2} - \tau) \simeq p_o(\tau), \tag{32}$$

then Eq (30) becomes

$$p_1(q_n\,|\,\Delta t_{1,2}) \simeq C\int_0^{\Delta t_{1,2}} p_0(\Delta t_{1,2} - \tau)p_0(\tau)p_1(q_n\,|\,\tau)\,d\tau. \tag{33}$$

A measurement of $p_1(q_n\mid\Delta t_{1,2})$ can therefore also be used to give an indication of whether or not the discharge behaves like a Markov process.

It should be cautioned that Eqs (26–27) may not always be reasonable approximations at all values of τ. In the case of Trichel-pulse corona discharges discussed below, it is found, for example, that there is always a critical minimum time, Δt_c, following any discharge pulse below which no subsequent pulse can occur. Thus, for $\Delta t_{1,2} - \tau < \Delta t_c$, neither Eq (32) nor Eq (33) can hold. It is found [32], however, that Eq (33) still gives a good representation of $p_1(q_n\,|\,\Delta t_{1,2})$ provided the upper limit of integration is replaced by $\Delta t_{1,2} - \Delta t_c$ and $\Delta t_{1,2}$ is not too close in value to $2\Delta t_c$.

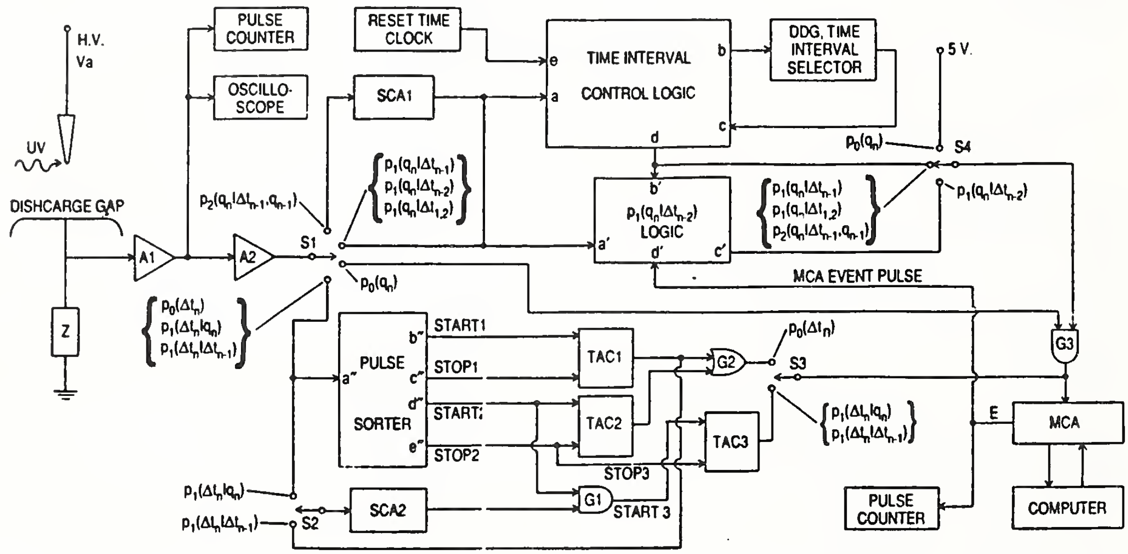

Figure 18. Measurement system giving the switch configurations needed for measurement of the various indicated pulse-height and time-interval distributions.

2.3.3 Measurement System

Figure 18 shows a somewhat simplified block diagram of the measurement system which indicates the configurations required for measurement of the various conditional probability distributions. The distributions that can be measured with this system are listed in Table 4.

The circuits associated with the time-interval control logic, $p_1(q_n\,|\,\Delta t_{n-2})$ logic and pulse sorter indicated in Fig. 18 are unique to this system. Details about the operation and design of these circuits are given in Ref. [29]. The time-to-amplitude converters (TAC$i, i = 1,2,3$), single-channel analyzer (SCA$i, i = 1,2$), digital-delay generator (DDG), and multichannel analyzer (MCA) are all commercially available instruments. The 256-channel MCA is driven by a microcomputer which enables data to be stored on either a floppy or hard disk for subsequent analysis.

The electrical-discharge pulses are detected electrically using a preamplifier (A1) connected to an impedance, Z, in series with the discharge gap. The pulses from A1 can be counted and observed on an oscilloscope. These pulses are sent to an amplifier A2, the gain of which can be adjusted so that the range of observed pulse amplitudes is within the range acceptable for input to the MCA.

The particular type of discharge phenomenon used to test this measurement concept is the well known [71–75] point-to-plane negative (Trichel) pulse corona in an elec-

Table 4. Distributions that can be measured with the present system

$p_0(q_n)$	Unconditional pulse-height and time-interval distributions
$p_0(\Delta t_n)$	
$p_1(q_n \,\vert\, \Delta t_{n-1})$	Conditional pulse-height distributions.
$p_1(q_n \,\vert\, \Delta t_{n-2})$	
$p_1(q_n \,\vert\, \Delta t_{n-3})$	
$p_1(q_n \,\vert\, \Delta t_{1,2})$	
$p_1(q_n \,\vert\, q_{n-1})$	
$p_2(q_n \,\vert\, \Delta t_{n-1}, q_{n-1})$	
$p_1(\Delta t_n \,\vert\, q_n)$	Conditional time-interval distributions
$p_1(\Delta t_n \,\vert\, \Delta t_{n-1})$	

tronegative gas. The discharge gap configuration is indicated in Fig. 18 and consists of a stainless steel point-plane electrode gap. The point electrode was maintained at a constant negative voltage with respect to the plane and the discharge pulse rate was controlled by ultra-violet (UV) irradiation of the point. Calibration of the pulse-amplitude measurement in terms of charge (pC) was performed by the method previously described [64].

By appropriate positioning of the switches shown in Fig. 18, it is possible to configure the system to measure the various indicated distributions directly. Data from all measurement configurations are accumulated by the MCA which contains an analog-to-digital converter for pulse-height analysis. For measurement of $p_0(q_n)$, the discharge pulses from A2 are fed directly to the MCA through gate G3 which is kept open by proper positioning of S4. The measurement of $p_0(\Delta t_n)$ requires use of a pulse sorter connected to two time-to-amplitude converters (TAC1 and TAC2) each of which generates an output pulse of amplitude proportional to the time separation between the indicated start and stop input pulses. The outputs of TAC1 and TAC2 are fed to the MCA through the OR gate G2 for pulse-height analysis. This arrangement permits recording of every sequential time interval, provided all time intervals are greater than the inherent TAC reset time, Δt_r, ($\Delta t_r = 50\,\mu s$ for the instruments used here). The amplitudes of pulses from the TAC's are calibrated on a time scale, and each TAC can be adjusted to cover different time ranges. For proper operation, TAC1 and TAC2 should be set to the same range.

The start pulse from the sorter for TAC1 serves as the stop pulse for TAC2 and vice versa. It is shown [29] that if there exist significant correlations between successive time intervals Δt_n and Δt_{n-1}, then it is possible that $p_0(\Delta t_n)$ will be distorted if $\Delta t_n < \Delta t_r$ for any n. To help determine if this is a problem, a random sampling of time intervals can be performed using a random pulse generator to gate the starting of TAC1 and TAC2 [30]. If there are no errors due to the finite TAC reset time, then $p_0(\Delta t_n)$ should be the same for both normal and random gated operation.

The measurement of $p_1(q_n \mid \Delta t_{n-1})$ requires use of a logic-controlled digital-delay generator (DDG) which restricts transfer of pulses from A2 to the MCA through gate G3 to a preselected time window. Details of the DDG time-interval control logic circuit are given in Ref. [29]. Basically, the system is designed so that the DDG sends a pulse of width $\delta(\Delta t_{n-1})$ to open G3 after a time delay Δt_{n-1} following a discharge pulse, provided no subsequent pulses have occurred within that interval. Thus only pulses that follow an initial pulse within a time range $\Delta t_{n-1} - \delta(\Delta t_{n-1})/2$ to $\Delta t_{n-1} + \delta(\Delta t_{n-1})/2$ are accumulated by the MCA for pulse-height analysis. To minimize errors in the measurement of $p_1(q_n \mid \Delta t_{n-1})$, it is desirable, as discussed in Ref. [29], that the DDG pulse width be selected so that $\delta(\Delta t_{n-1}) \ll \Delta t_{n-1}$.

Measurement of the second order conditional distribution $p_2(q_n \mid \Delta t_{n-1}, q_{n-1})$, requires use of a single-channel analyzer (SCA1) inserted between A2 and the input to the time-interval control logic. The SCA1 restricts the input pulses that trigger the DDG to have amplitudes that lie within a selected range from $q_{n-1} - \delta(q_{n-1})$ to $q_{n-1} + \delta(q_{n-1})$, where again $\delta(q_{n-1}) \ll q_{n-1}$ is a desirable condition to avoid errors.

With the use of SCA2 and TAC3, the system can be configured by the indicated positioning of S1, S2, and S3 to directly measure either $p_1(\Delta t_n \mid q_{n-1})$ or $p_1(\Delta t_n \mid \Delta t_{n-1})$. When measuring the former, SCA2 is used to select a narrow range of q_{n-1} values that will permit triggering the start of TAC3, the output of which is fed to the MCA. The measurement of $p_1(\Delta t_n \mid \Delta t_{n-1})$ requires that SCA2 select a narrow range of pulse amplitudes from the output of TAC1 to start TAC3.

The determination of $p_1(q_n \mid q_{n-1})$ can be performed indirectly by measurement of $p_2(q_n \mid \Delta t_{n-1}, q_{n-1})$, $p_1(\Delta t_n \mid q_n)$, and $p_0(q_{n-1})$ and using the requirement that

$$p_1(q_n \mid q_{n-1}) = \int_0^\infty p_2(q_n \mid \Delta t_{n-1}, q_{n-1}) p_1(\Delta t_{n-1} \mid q_{n-1}) p_0(q_{n-1}) d(\Delta t_{n-1}). \qquad (34)$$

Under some conditions this distribution can be measured directly by configuring the system to measure $p_2(q_n \mid \Delta t_{n-1}, q_{n-1})$ and then selecting the DDG delay and time window widths respectively to be smaller and larger than the expected minimum and maximum pulse-time intervals. There may be cases, however, where these adjustments cannot be made, such as when a significant fraction of the time intervals exceed the maximum possible DDG window setting.

The measurement configuration for determination of $p_1(q_n \mid \Delta t_{1,2})$ requires a rearrangement of the time-interval control logic circuit as discussed in Ref. [29]. The measurement of $p_1(q_n \mid \Delta t_{n-2})$ involves use of the $p_1(q_n \mid \Delta t_{n-2})$ logic circuit shown in Fig. 18 together with configuring the time-interval control logic so that it would otherwise allow measurement of $p_1(q_n \mid \Delta t_{n-1})$. It is also possible to measure $p_1(q_n \mid \Delta t_{n-3})$ by using the $p_1(q_n \mid \Delta t_{n-2})$ logic circuit together with having the time-interval control logic set for a $p_1(q_n \mid \Delta t_{1,2})$ measurement. In the case of a $p_1(q_n \mid \Delta t_{n-2})$ measurement, the indicated $p_1(q_n \mid \Delta t_{n-2})$ logic circuit, when inserted by switch S4 in Fig. 18, acts to inhibit opening of gate G3 until after there has been a coincidence between the digital delay generator pulse selected by the time-interval control logic and a discharge pulse from A2, i.e., until after there has been the occurrence of a pulse time-interval Δt_{n-2}. The next pulse to occur after this coincidence is then allowed to be recorded and analyzed by the MCA through G3 independent of its time separation, Δt_{n-1}, from the previous pulse. After a pulse height is recorded, the MCA sends an "event pulse" to reset the $p_1(q_n \mid \Delta t_{n-2})$ logic circuit.

2.3.4 Results—Trichel Pulses in N_2/O_2

Examples of results obtained for UV-sustained negative point-plane Trichel-pulse corona [71–75] in an $N_2/20\%O_2$ gas mixture are presented here. Figure 19 shows data on the measured distributions $p_0(q_n)$, $p_1(q_n \,|\, \Delta t_{n-1})$, and $p_2(q_n \,|\, \Delta t_{n-1}, q_{n-1})$ for Trichel pulses (data points) together with results of the integrals given by Eq's (26) and (29) for $p_o(q_n)$ and $p_1(q_n \,|\, \Delta t_{n-1})$ (dashed and dot-dashed lines). These data were obtained for an absolute gas pressure of 100 kPa ($\sim$ 1 atm), a point-to-plane gap spacing of 2.08 cm, and a point electrode radius-of-curvature at the tip of 0.094 mm. Both electrodes were made of polished stainless steel. Since the discharge was UV-sustained, the pulse rate (related to mean time interval $\overline{\Delta t_n}$ from Eq. (21)) was controlled by the intensity of the UV radiation directed at the point cathode through a quartz window. The discharge pulses in this case were initiated by photo-electrons released from the cathode, and because the electron release rate is roughly proportional to the UV intensity, $\overline{\Delta t_n}$ should decrease with increasing UV intensity. This trend is evident from the measured data for $p_0(\Delta t_n)$ shown in Fig. 20 that indicate a much broader distribution at the lower UV intensity than at the higher intensity. The high UV-intensity data in Fig. 20 correspond to the same conditions under which the data shown in Fig. 19 were obtained.

The distributions plotted in both Fig's 19 and 20 have again been arbitrarily normalized to the maxima. Values selected for Δt_{n-1} and q_{n-1} used to obtain the conditional pulse-height distributions displayed in Fig. 19 are indicated in the legend with corresponding plotting symbols. Both $p_0(q_n)$ and $p_1(q_n \mid \Delta t_{n-1})$ have been plotted on a logarithmic scale, and $p_2(q_n \mid \Delta t_{n-1}, q_{n-1})$ is shown on a linear scale. The pulse heights are expressed here in units of charge (pC). The solid lines in Fig. 19 represent gaussian profiles that have been fitted to the $p_2(q_n \,|\, \Delta t_{n-1}, q_{n-1})$ data. The dashed and dot-dash lines represent results of the convolutions from Eq's (29) and (26) respectively which required use of the corresponding data for $p_0(\Delta t_n)$ shown in Fig. 20. A gaussian representation of $p_1(q_n \mid \Delta t_{n-1})$ was used in performing the integration of Eq. (26)). As evident from Fig. 19, this assumption leads to errors in the calculated $p_0(q_n)$ at low q_n values where the gaussian representation begins to become inadequate due to increasing asymmetries in the $p_1(q_n \,|\, \Delta t_{n-1})$ profile.

From the results presented here, it can be seen that there are significant memory effects that influence development of Trichel pulses. The data displayed in Fig. 19 clearly indicate that for arbitrary q_n

$$p_0(q_n) \neq p_1(q_n \,|\, \Delta t_{n-1}) \neq p_2(q_n \,|\, \Delta t_{n-1}, q_{n-1}),$$

at allowed values for Δt_{n-1} and q_{n-1}. Thus it must be concluded that q_n, Δt_{n-1}, and q_{n-1} are not independent random variables, i.e., the most probable amplitude of any discharge pulse is influenced by the time separation from and the amplitude of the preceding pulse. It is obvious from the data on $p_1(q_n \,|\, \Delta t_{n-1})$ that the mean discharge-pulse amplitude increases with increasing time separation from the preceding pulse. This behavior is expected if one allows the possibility that the negative-ion space-charge cloud from the preceding pulse [73] has a shielding effect that reduces the electric field in the vicinity of the point electrode. The electric-field strength near

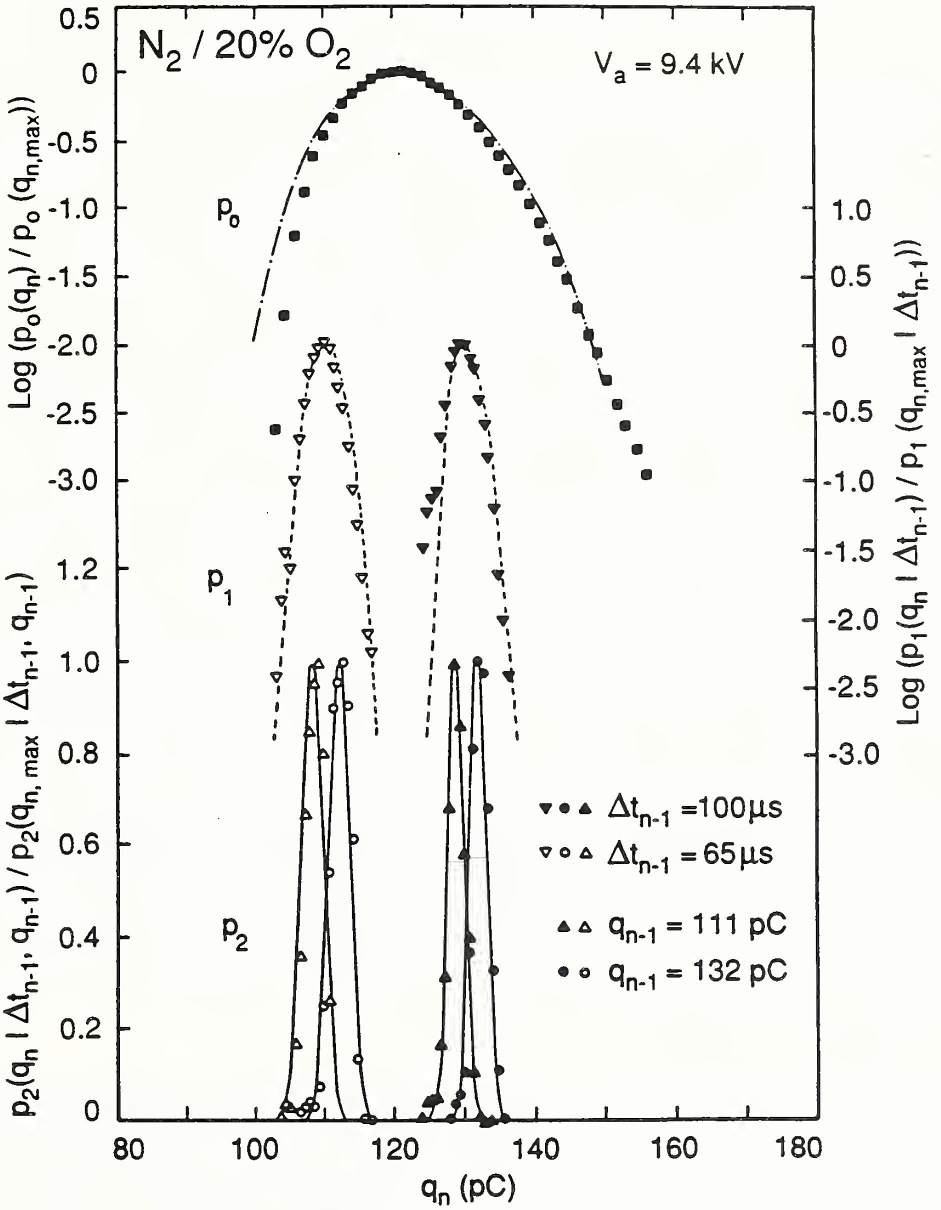

Figure 19. Normalized unconditional (p_0) and conditional (p_1 and p_2) pulse-height distributions for negative, point-plane Trichel-pulse discharges in an $N_2/20\%O_2$ gas mixture at an applied gap voltage (V_a) of 9.4 kV. The data points are from measurements; the dot-dashed curve is from an integration of Eq (26); the dashed curves are from an integration of Eq (29); and the solid curves are gaussian profiles fit to the p_2 data. The conditional distributions were measured at the indicated "fixed" values for Δt_{n-1} and q_{n-1}. The maxima in the distributions are commonly denoted to occur at values $q_{n,\max}$ which are obviously different for each distribution.

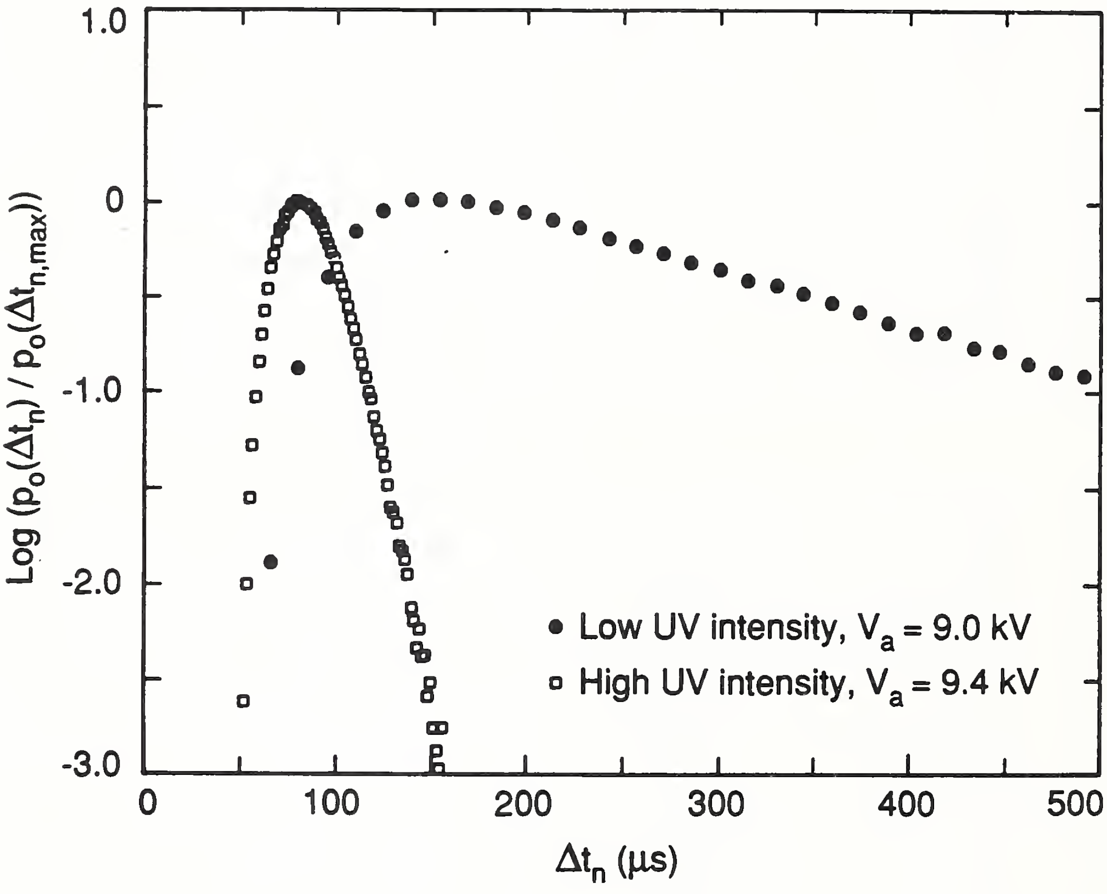

Figure 20. Normalized unconditional discharge pulse time-interval distributions measured at the indicated applied voltages (V_a) and UV intensities for negative, point-plane Trichel pulse discharges in an $N_2/20\%O_2$ gas mixture. The distribution measured at 9.4 kV for high UV intensity corresponds to conditions that are identical to those used to obtain the data in Fig. 19. The maxima in the distributions are commonly denoted to occur at values $\Delta t_{n,max}$ which are obviously different for the two distributions.

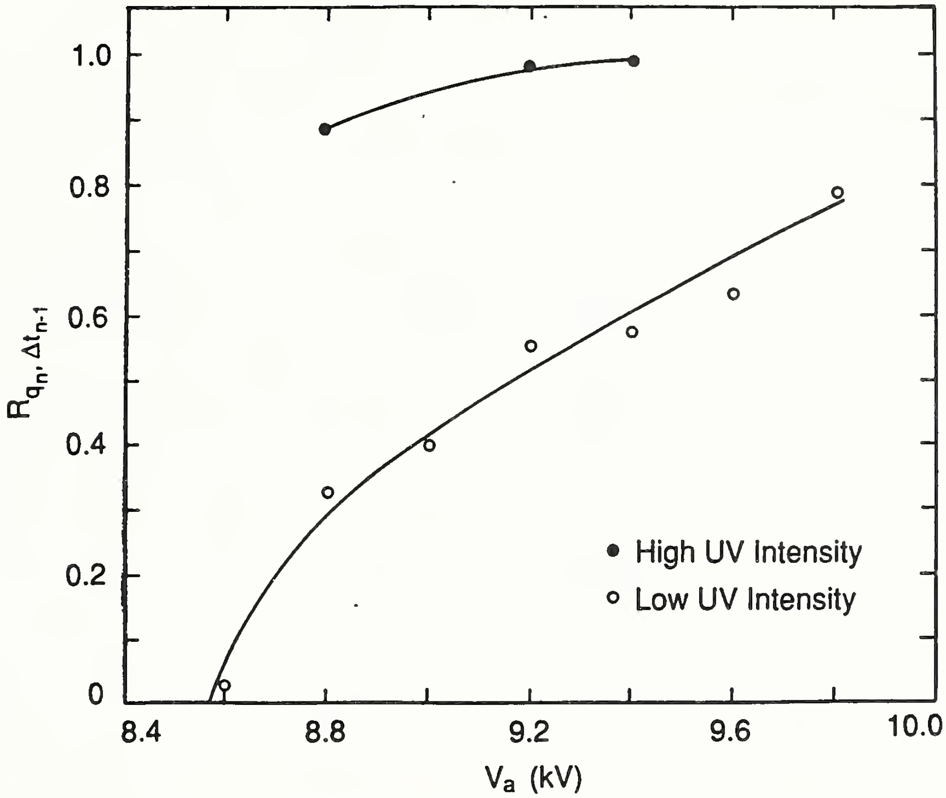

Figure 21. Correlation coefficients for the variables q_n and Δt_{n-1} as functions of discharge gap voltage (V_a) at two different indicated levels of UV intensity for negative, point-plane Trichel-pulse discharges in an $N_2/20\%O_2$ gas mixture. The coefficients are calculated from Eq's (16–21) using measured distributions such as shown in Fig's 19 and 20.

the point will tend to increase as the space-charge cloud moves further away toward the anode. Since the mean discharge-pulse size will increase with increasing field strength, relatively larger pulses can be expected to develop as more time elapses between pulses. A more extensive analysis of the data on $p_1(q_n \mid \Delta t_{n-1})$ in terms of ion space-charge motion in the discharge gap have shown that the experimental results are generally consistent with this interpretation [32].

The corresponding correlation coefficients, $R_{q_n,\Delta t_{n-1}}$, computed from data on $p_0(q_n)$, $p_1(q_n \mid \Delta t_{n-1})$, and $p_0(\Delta t_n)$ for different discharge gap voltages and UV intensities are shown in Fig. 21. These results demonstrate that $R_{q_n,\Delta t_{n-1}}$ approaches unity (thereby indicating a higher degree of correlation between q_n and Δt_{n-1}) as both UV intensity and applied voltage increase. The increase in $R_{q_n,\Delta t_{n-1}}$ with UV intensity is reasonable because, as indicated by the data in Fig. 20, $\overline{\Delta t_n}$ decreases with increasing UV intensity, thus allowing less time for "memory effects" in the gap, e.g., ion space charge, to dissipate. The increase in $R_{q_n,\Delta t_{n-1}}$ with applied voltage is also undoubtedly associated with an observed decrease in $\overline{\Delta t_n}$ with voltage.

The data on $p_2(q_n \mid \Delta t_{n-1}, q_{n-1})$ indicate that for a given Δt_{n-1}, large pulses are preferentially followed by large pulses and small pulses by small pulses. The reasons for this type of correlation are not entirely obvious, but might be related to the formation of neutral metastable species during the discharge pulse that are more readily ionized by electron collisions. Enhancements in the ionization rates for the gas due to the presence of metastables will necessarily lead to an increase in discharge pulse size. Because metastable densities can be expected to increase with increasing discharge magnitude, large pulses will preferentially give rise to larger subsequent pulses. It is also found that the degree of correlation between q_n and q_{n-1} decreases as Δt_{n-1} increases which is expected as more time is allowed for metastables to diffuse away from the immediate vicinity of the point electrode where ionization occurs.

Although not shown here, measurements of the conditional time-interval distributions $p_1(\Delta t_n \mid \Delta t_{n-1})$ and $p_1(\Delta t_n \mid q_n)$ indicate that for Trichel pulses there are measurable, albeit weak, correlations between Δt_n and Δt_{n-1} and between Δt_n and q_n. The results from these measured conditional time-interval distributions can be interpreted in terms of the influence of ion space charge and metastables on the probability for initiating the next discharge pulse [32].

It is also found from measurements of $p_1(q_n \mid \Delta t_{n-2})$ that q_n and Δt_{n-2} are not significantly correlated, i.e., for allowed Δt_{n-2}, $p_1(q_n \mid \Delta t_{n-2})$ does not differ significantly from $p_0(q_n)$. This means that significant memory effects do not extend back in time beyond the most recent pulse and therefore the Trichel-pulse phenomenon behaves like a Markov process. It is, in fact, expected that for this type of phenomenon, the correlations between adjacent pulses will dominate, e.g., the ion space charge from the most recent discharge pulse will have by far the greatest influence on development of any given discharge pulse.

2.3.5 Results—Trichel Pulses in Air

As expected, the stochastic behavior of Trichel pulses in air is found to be nearly identical to that of Trichel pulses in N_2/O_2 mixtures. We show here examples of additional results that indicate how Trichel pulse development is strongly influenced by memory effects.

Shown in Figures 22 and 23 are corresponding sets of measured data on $p_0(q)$ and $p_0(\Delta t)$ respectively at the different indicated discharge point-to-plane gap voltages V_a for Trichel pulses in room air. The point electrode was made of polished stainless steel with a tip radius-of-curvature of 0.01 mm and the point-to-plane gap spacing of 1.92 cm. All of the data in Figures 22 and 23 were obtained with the same level

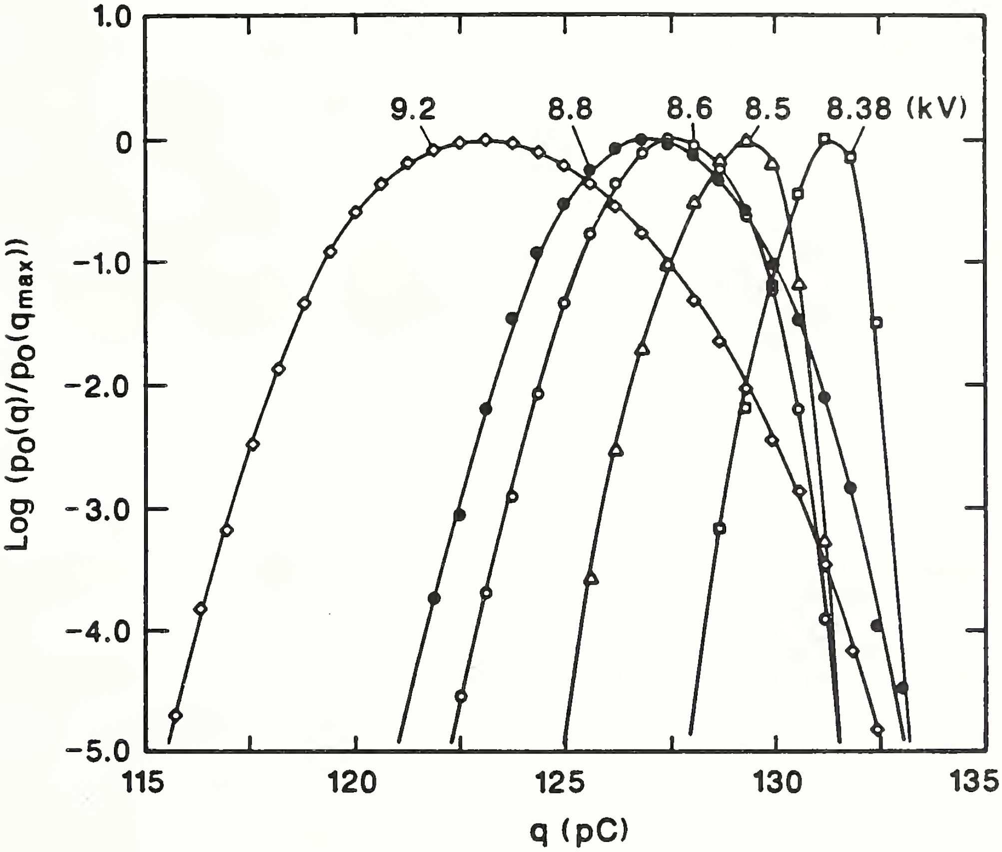

Figure 22. Measured $\log(p_0(q)/p_0(q_{max}))$ versus q at the different indicated gap voltages V_a for a fixed UV intensity. Corresponding data for $p_0(\Delta t)$ and $p_1(q_n \mid \Delta t_{n-1})$ are given in Figures 23 and 26.

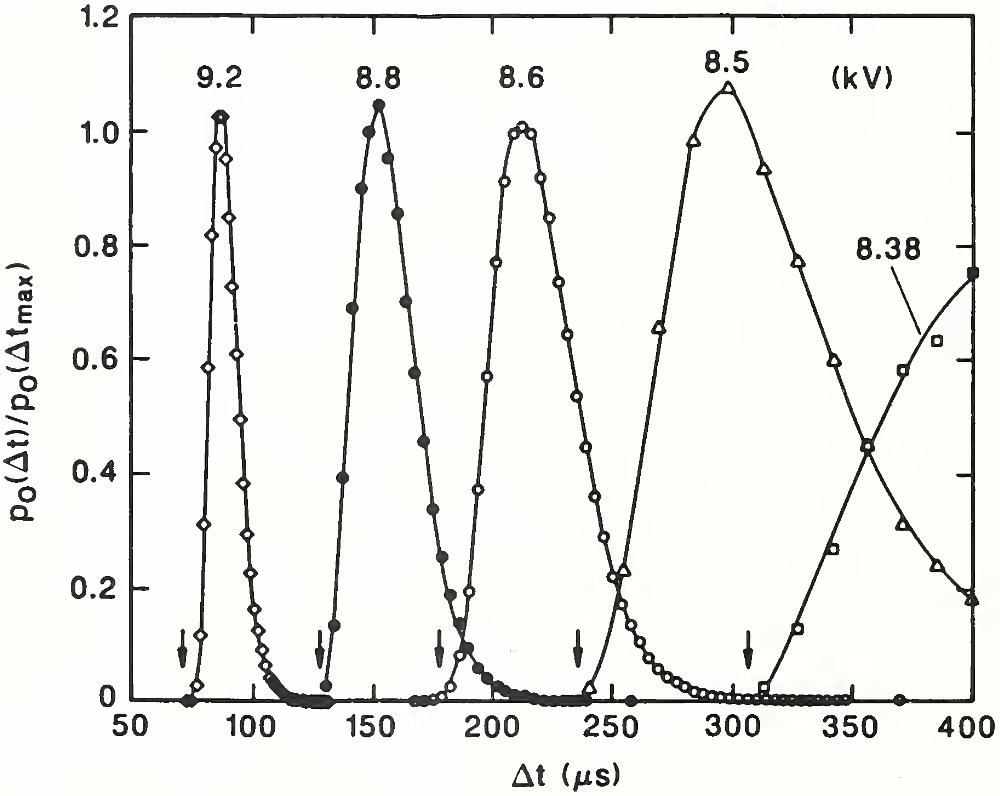

Figure 23. Measured $p_0(\Delta t)/p_0(\Delta t_{max})$ versus Δt at the different indicated gap voltages V_a for a fixed UV intensity. Corresponding data for $p_0(q)$ and $p_1(q_n \mid \Delta t_{n-1})$ are given in Figures 22 and 26.

of UV-irradiation. For ease of plotting, the distribution functions shown have again been normalized to their maxima, e.g., Figure 22 shows $p_0(q)/p_0(q_{max})$ versus q, where q_{max} is the value of q at the maximum in $p_0(q)$.

As indicated by the vertical arrows in Figure 23, there always exists a minimum time interval Δt_c below which no subsequent pulses appear after a given pulse. This minimum interval is evidently related to the time required for the positive and negative ion space charge resulting from a discharge pulse to clear the region near the point electrode enough so that the local electric field is sufficiently restored to allow formation of the next pulse. It can be expected, as observed here, that Δt_c will diminish with applied gap voltage since the ions will be swept away more quickly at higher field strengths.

The profiles of the measured $p_0(\Delta t)$ for $\Delta t > \Delta t_{max}$ nearly exhibit a poisson character as expected if this part of the distribution is determined by the time lags associated with field-enhanced photoelectron release needed to initiate the next pulse. This effect is supported by the data shown in Figure 24 for $p_0(\Delta t)$ measured for different UV intensities $I_i(I_1 > I_2 > I_3)$, where it is seen that the slope of the log $(p_0(\Delta t))$ versus Δt curve for $\Delta t > \Delta t_{max}$ decreases with decreasing I_i.

The data on $p_0(\Delta t)$ in Fig's 23 and 24 together with the corresponding $p_0(q)$ data in Fig's 22 and 25 clearly show a strong correlation between q_n and Δt_{n-1}. Note in Fig. 22 that as the applied voltage increases the mean pulse amplitude $\overline{q}$, as determined by Eq. (20), actually decreases. Similarly, as seen in Fig. 25, $\overline{q}$ also decreases with increasing UV intensity. This is obviously the type of behavior that would be expected if q_n is strongly correlated with Δt_{n-1}. As the mean pulse repetition rate increases there should be a corresponding decrease in $\overline{q}$. The strength of the correlation between q_n and Δt_{n-1} is indicated by the data on $p_1(q_n \mid \Delta t_{n-1})$ displayed in Fig. 26 for different indicated Δt_{n-1} and for $V_a = 9.2$ kV.

The distributions $p_1(q_n \mid \Delta t_{n-1})$ tend to have nearly a gaussian shape. The mean value of q_n can decrease significantly with Δt_{n-1} as illustrated in Fig. 27 which shows a plot of the q_{max} for $p_1(q_n \mid \Delta t_{n-1})$ versus Δt_{n-1} corresponding to the results for $p_0(q)$ and $p_0(\Delta t)$ presented in Figures 20 and 21. The amplitude of the discharge pulse will approach a maximum limiting value, q_{lim}, as the time separation from the previous pulse becomes sufficiently long that the space charge completely clears the gap. This is referred to as the "first pulse condition" [68] and is evident from the data in Fig. 27 as a saturation effect and from the $p_0(q)$ data of Fig. 25 as a sharp peak or abrupt drop-off at $q = q_{\text{lim}}$. Features associated with $q \longrightarrow q_{\text{lim}}$ are apparent in the $p_0(q)$ distribution only if the corresponding $p_0(\Delta t)$ distribution is sufficiently broad so that a significant fraction of the observed discharge events are separated from previous events by times greater than the time for space-charge transport across the gap.

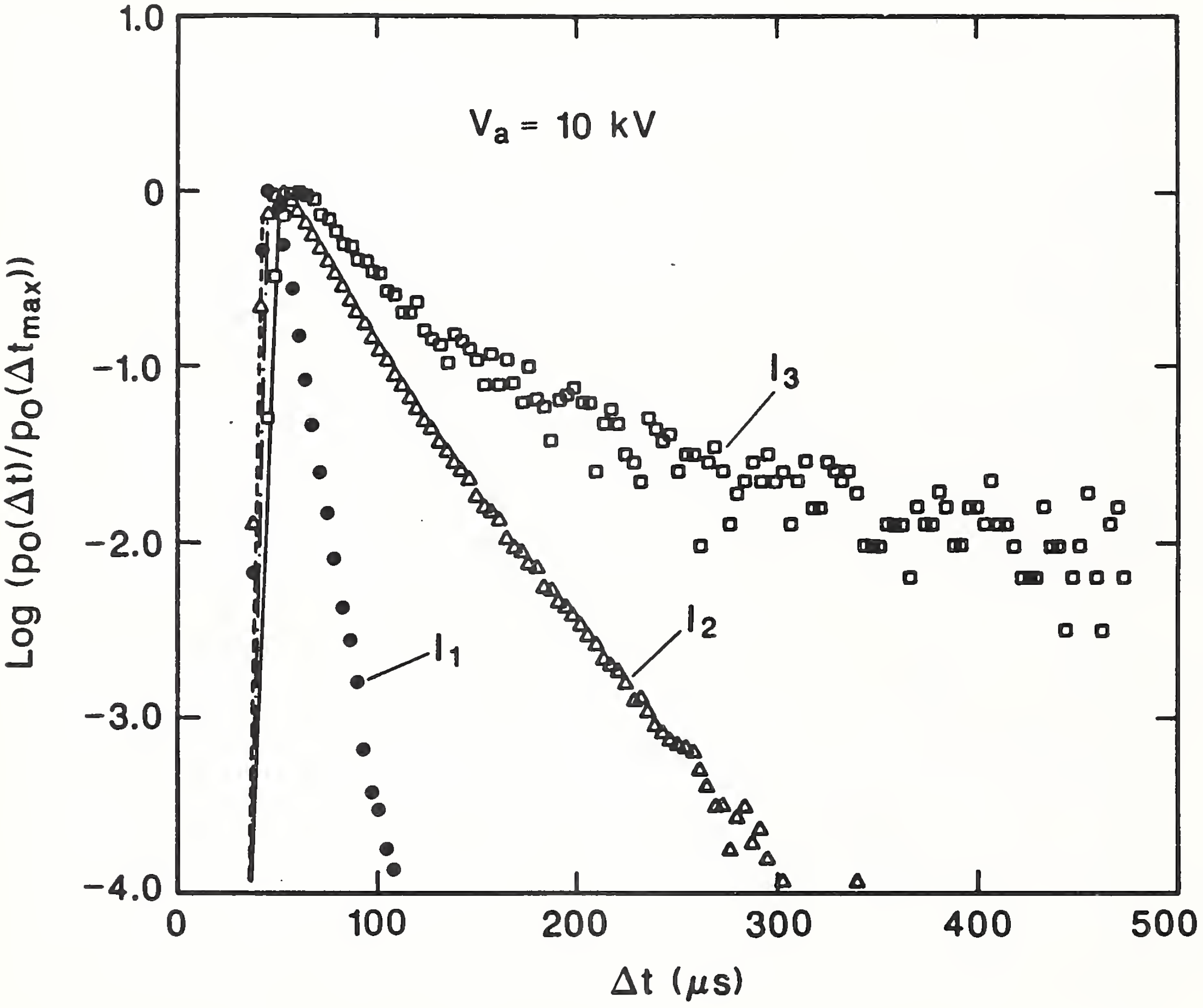

Figure 24. Measured $\log(p_0(\Delta t)/p_0(\Delta t_{max}))$ versus Δt for $V_a = 10\,\mathrm{kV}$ and three different UV intensities, $I_1 > I_2 > I_3$. Corresponding $p_0(q)$ data appear in Fig. 25. The electrode gap configuration was nearly the same as used to obtain the data in Figs. 22 and 23.

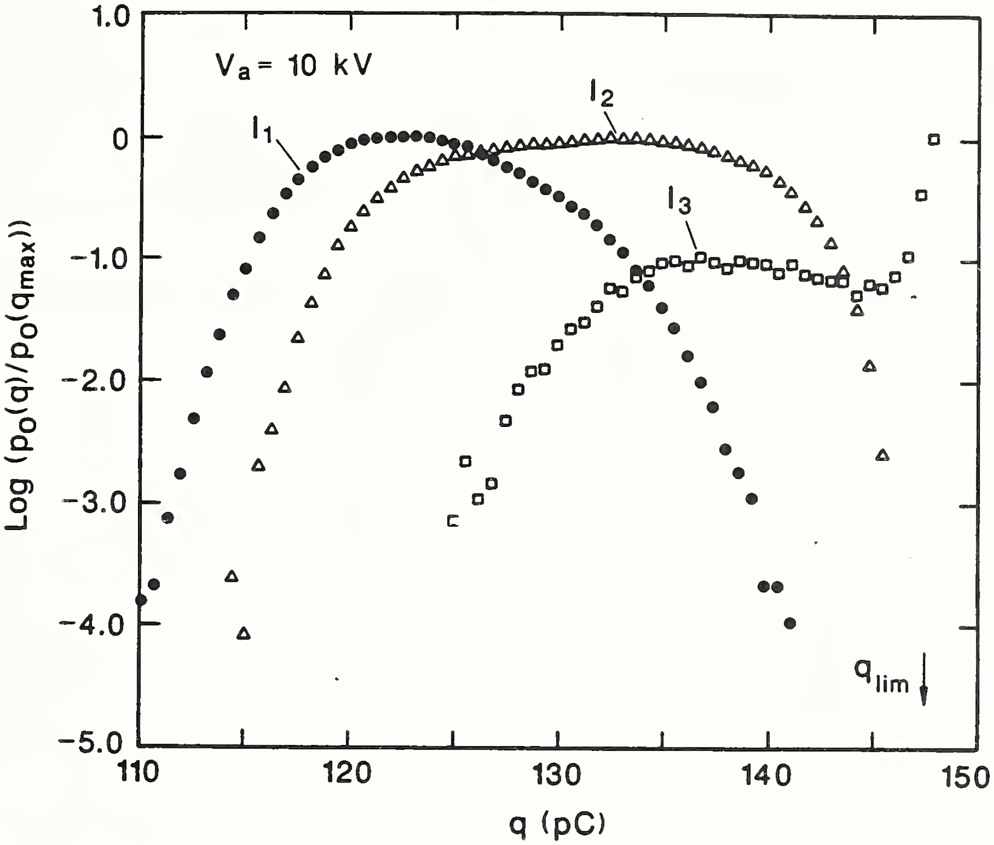

Figure 25. Measured $\log(p_0(q)/p_0(q_{max}))$ versus q for $V_a = 10\,\text{kV}$ and three different UV intensitites, $I_1 > I_2 > I_3$. Corresponding $p_0(\Delta t)$ data appear in Figure 24. The electronde gap configuration was nearly the same as used to obtain the data in Figs. 22 and 23.

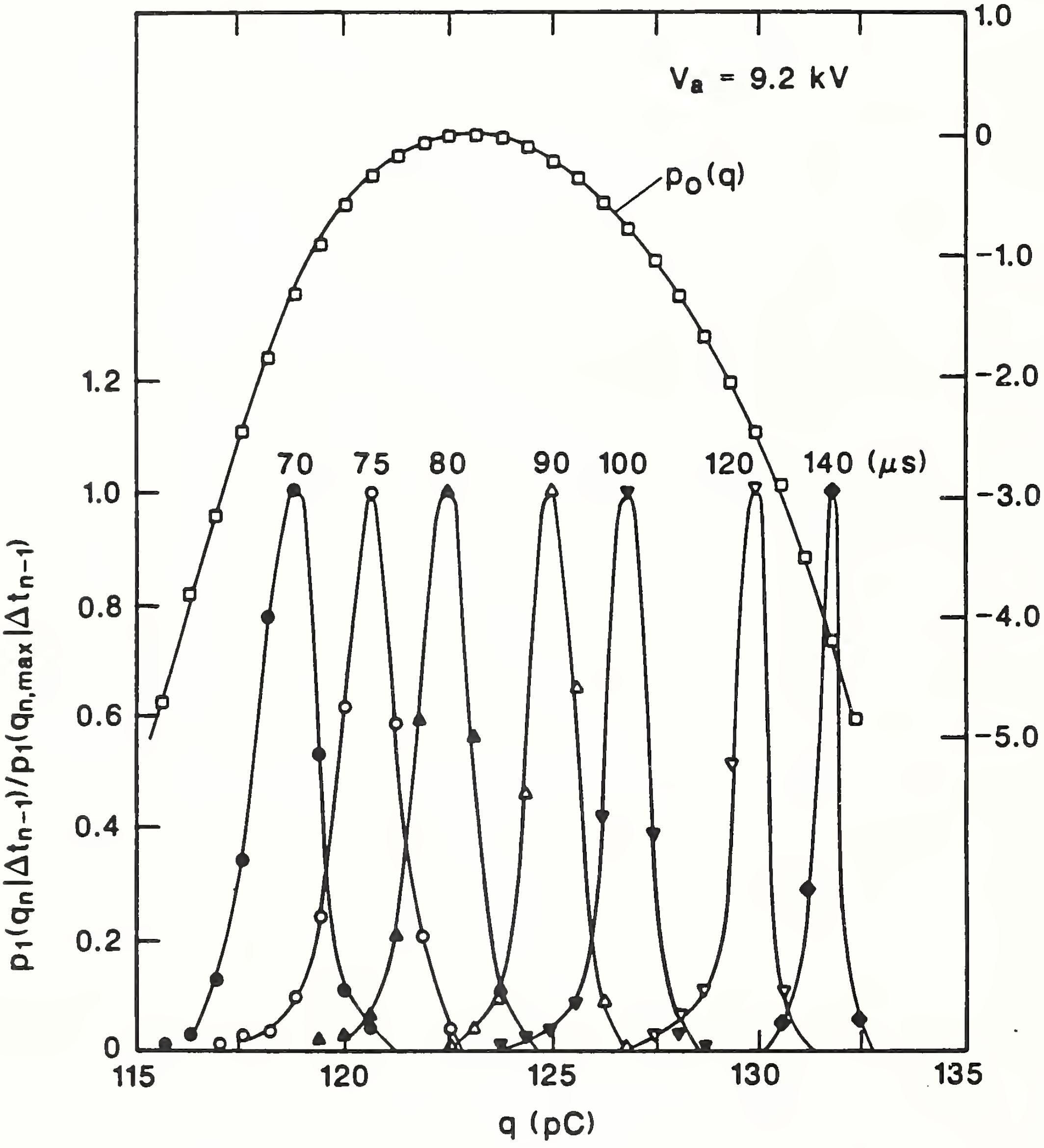

Figure 26. Measured $p_1(q_n \mid \Delta t_{n-1})/p_1(q_{n,max} \mid \Delta t_{n-1})$ versus q for the indicated Δt_{n-1} values in microseconds at $V_a = 9.2$ kV together with the corresponding normalized unconditional pulse height distribution expressed as $\log(p_0(q)/p_0(q_{max}))$. Also see corresponding data in Figs. 22 and 23.

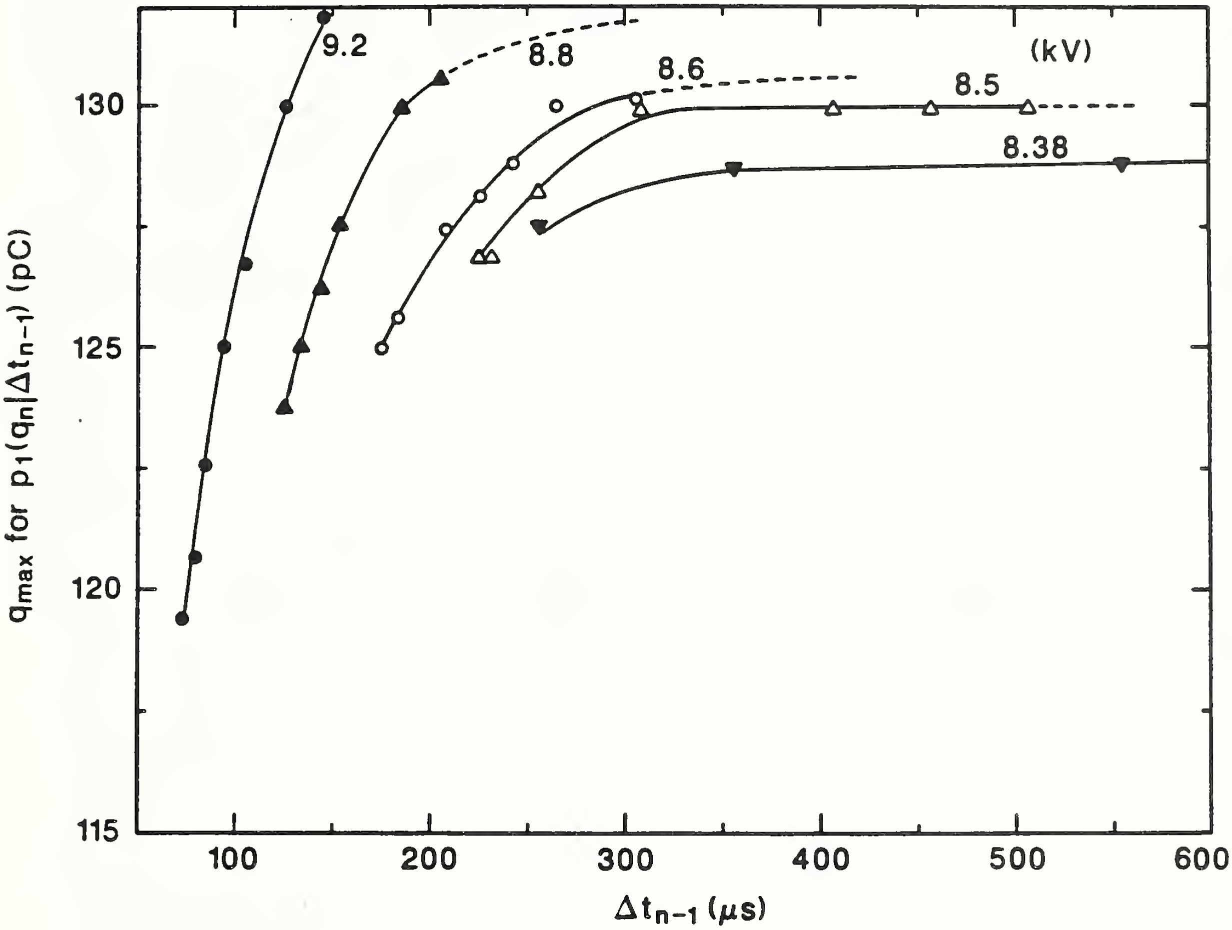

Figure 27. Plot of q_{max} versus Δt_{n-1} for the different indicated V_a corresponding to the data in Figs. 22, 23, and 26. Here q_{max} is the value of q_n at which $p_1(q_n \mid \Delta t_{n-1})$ is at its maximum.

2.3.6 Results—Trichel Pulses in SF_6/O_2

In the past there has been some question about the existence of Trichel pulses in SF_6 [64, 82, 83]. The present measurements were performed to investigate the influence of SF_6 on the stochastic properties of Trichel pulses in oxygen. In general, it was found that the behavior of Trichel pulses in SF_6/O_2 is qualitatively similar in most respects to that found for other electronegative gas mixtures such as the N_2/O_2 mixture discussed above.

Some examples of measured unconditional pulse-height and corresponding pulse-time-interval distributions ($p_0(q)$ and $p_0(\Delta t)$) are shown in Fig. 28. In this case, the discharge was only partially sustained by the UV radiation so that when the UV was turned off, discharge pulses still occurred, but were, on average, much more widely separated in time. It is seen that in the case where the time-interval distribution becomes quite broad (no UV) the corresponding $p_0(q)$ exhibits a sharp peak at $q_{\rm lim}$ as also seen from the data for air. The correlation between q_n and Δt_{n-1} as evident from the data on $p_1(q_n \mid \Delta t_{n-1})$ shown in Fig. 29 is the same as seen for air and N_2/O_2 mixtures. This is expected since the physical mechanism of space-charge motion responsible for this correlation effect is essentially the same for all electronegative gases.

It is found that as the SF_6 content in oxygen increases, the mean discharge pulse height decreases and the mean time separation between pulses increases for any fixed gap voltage, gas pressure, and electrode configuration [31]. Also, as SF_6 content increases the discharge pulses appear more randomly in time. i.e., there is a broadening of the pulse time-interval distribution. It is evident that addition of SF_6 to O_2 has the effect of suppressing the growth of corona discharges due to the increased electronegativity of the gas. In "pure" SF_6 the "Trichel" pulses that occur under self-sustained conditions appear to be quite small (below 20 pC) and exhibit a very broad time-interval distribution. Because of the relatively small size and corresponding spatial extent of the Trichel pulse discharges in pure SF_6, it can be expected that their distributions in $p_0(q)$ and $p_0(\Delta t)$ will be significantly affected by details of electrode geometry and fluctuations in electron release rates, gas density, etc. The present observations and interpretations of negative-corona pulses in SF_6 are consistent with previous work [82, 83]. Previously observed [64] Trichel pulses at over-voltages for SF_6 in the absence of UV irradiation seem to correspond to the first pulse conditions ($q \longrightarrow q_{\rm lim}$) because of the relatively low pulse repetition rates, i.e., long mean time intervals between pulses.

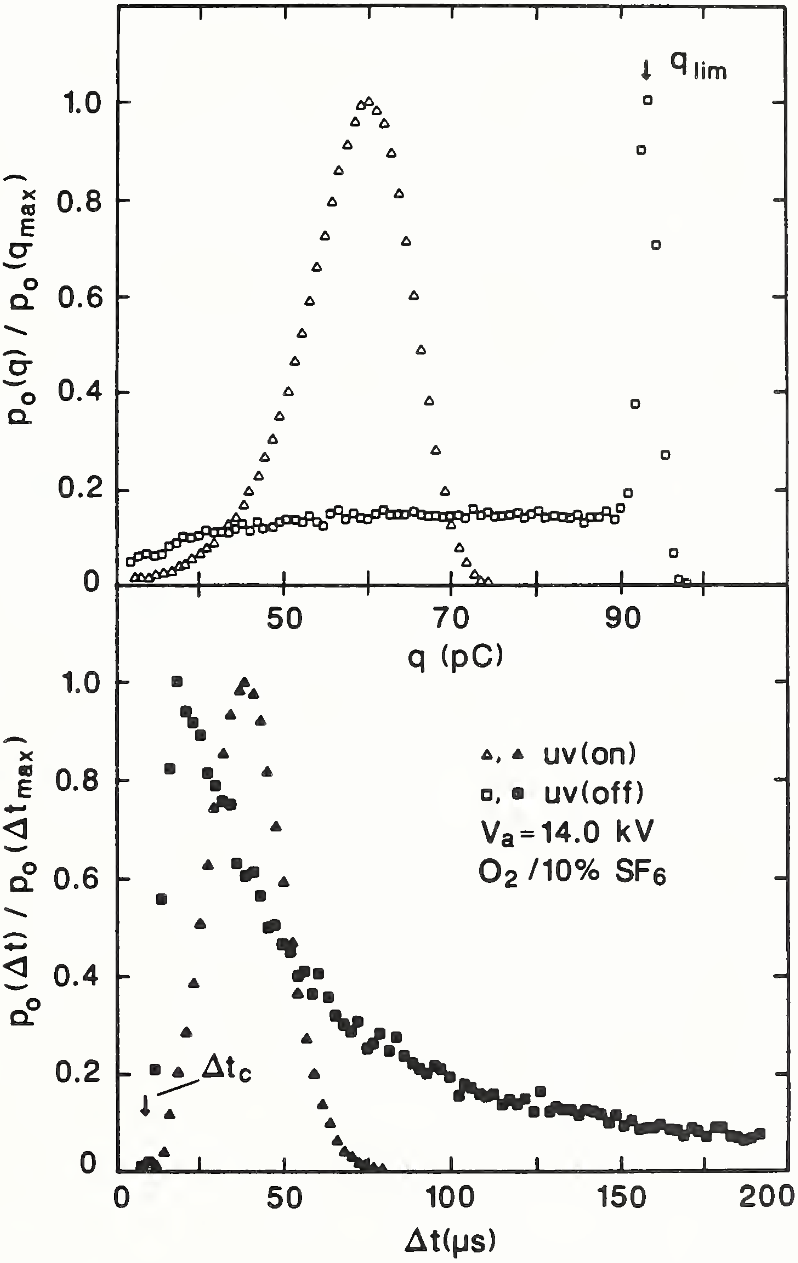

Figure 28. Measured $p_0(q)/p_0(q_{max})$ versus q and corresponding $p_0(\Delta t)/p_0(\Delta t_{max})$ versus Δt at 14.0 kV in O_2/10%SF_6 mixture under two conditions of irradiation (UV = on and UV = off).

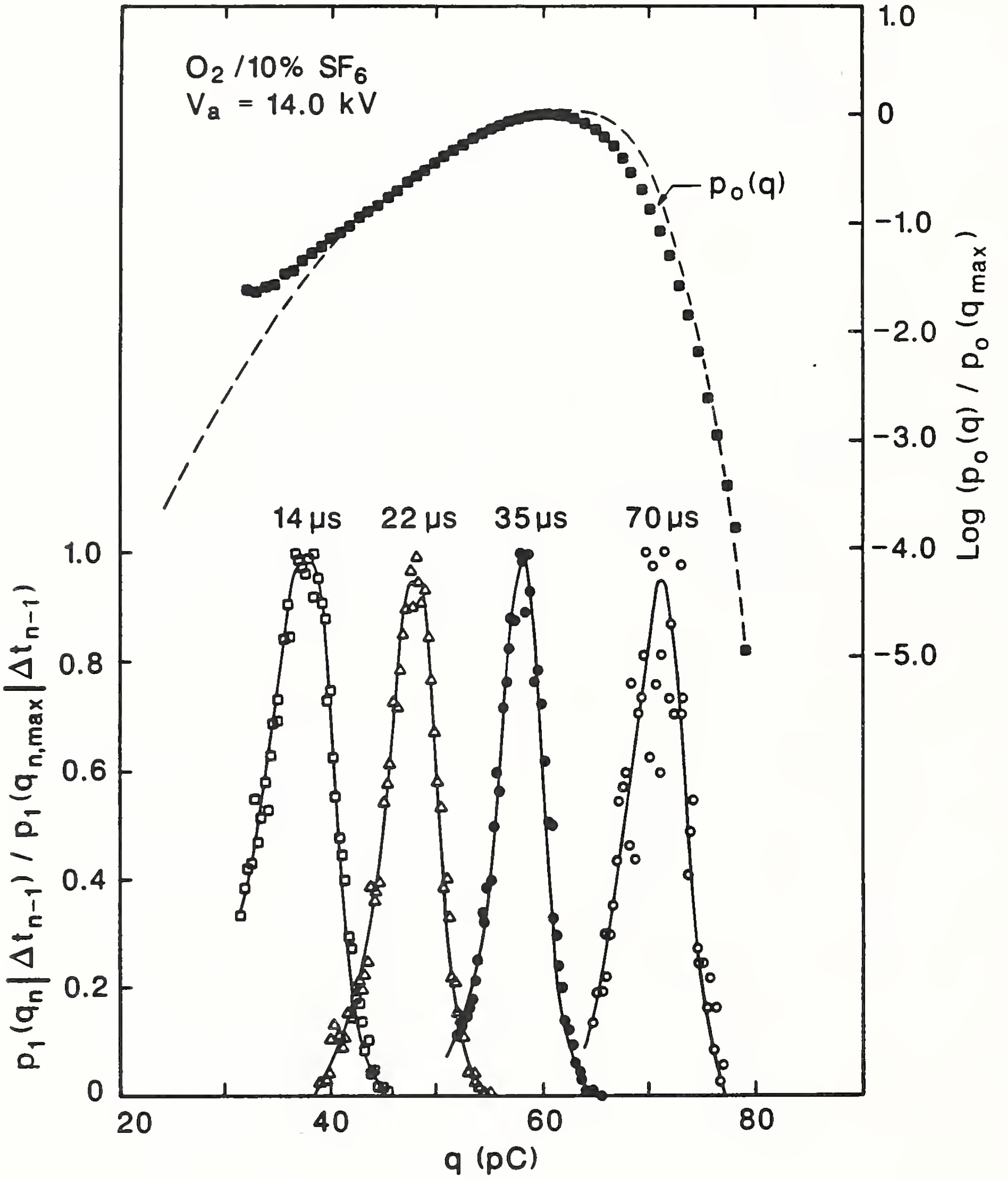

Figure 29. Measured $p_1(q_n \mid \Delta t_{n-1})/p_1(q_{n,max} \mid \Delta t_{n-1})$ versus q for the indicated Δt_{n-1} values at $V_a = 14.0\,\mathrm{kV}$ together with the corresponding measured (closed squares) and calculated (dashed line, using Eq. (26)) unconditional pulse-height distribution $p_0(q)/p_0(q_{max})$ for an $O_2/10\%SF_6$ mixture.

3. INTERFACIAL PHENOMENA IN LIQUIDS

Task 04
Edward F. Kelley
Electricity Division
National Institute of Standards and Technology

3.1 Introduction

The objective of this research is to understand the mechanisms of electrical failure in practical insulation materials used in power systems apparatus. In even the simplest insulation system, there are a large number of factors which influence the electrical breakdown voltage of that system. As the insulation medium becomes more complicated, such as in liquid-solid composite systems, the number of factors which can change the breakdown characteristics increases dramatically. There exists a body of tests and standards for qualifying insulation materials for suitability in power apparatus. However, there often are found to be wide variations in the results from such tests because there are many factors which are not properly controlled. Such variations are indications of a lack of complete understanding of all the factors which contribute to the failure process. It is, therefore, the goal of this research to guide the development of models which serve to quantify the breakdown process based on the physical and chemical properties of the insulation media. New standards can then be created to characterize more adequately the suitability of both new and existing insulation media. The primary tools for providing modeling information are voltage and current measurements coupled with optical observations in the form of light-emission measurements, high-speed photography, or electro-optical measurements.

To this end, three areas of research are presented here: 1) Partial Discharges as a Function of Pressure, 2) Nanosecond Breakdown at a Liquid-Solid Interface, and 3) An Image-Preserving Optical Delay. The third item has been discussed in prior reports without presenting the details of the apparatus. The details are presented in this report essentially as submitted for the 42nd Annual Conference of the Society for Imaging Scientists and Engineers, Boston, May 1989.

3.2 Partial Discharges vs Hydrostatic Pressure

The importance of studying and understanding partial discharge (PD) phenomena cannot be overstressed. PD activity exists in almost all power systems apparatus. It is also anticipated that the initiation of the prebreakdown process is the same

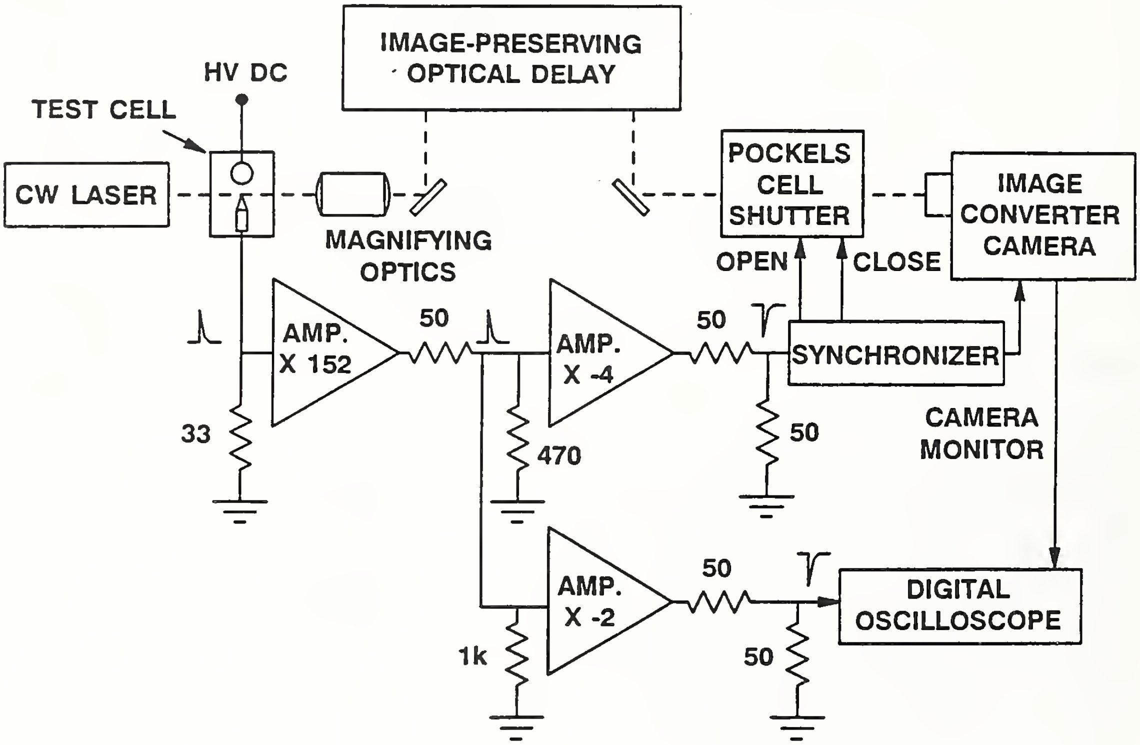

Figure 30. Equipment diagram for observing partial discharges associated with dc.

for steady-state PD as for impulse breakdown. That is, the prebreakdown streamer initiation for impulse or for PD's at their earliest times appear to be identical. This is clearly true for negative polarity, and expected to be true for positive polarity. It is the initiation of the phenomena which is important. The key to improving insulation lies in the prevention of the initiation of the streamer or PD. Furthermore, the modeling required to replicate the phenomena is likely simpler for the initiation than for the growth of the streamer.

A collaborative experiment was conducted with a group from the University of Tennessee headed by Dr. M. O. Pace. Partial discharges in hexane were investigated under the application of dc voltage at different hydrostatic pressures from 27 kPa to 0.3 MPa absolute pressure (27 kPa is slightly above the vapor pressure of hexane at room temperature). This represents an extension of previous observations which were made at atmospheric pressure (0.1 MPa). The experiment is diagrammed in Fig. 30. A needle with a tip radius of 3 μm is placed 5 mm from a sphere. A sensitive amplifier monitors the current supplied to the PD, and an image-converter camera photographs the growth of the PD. In order to capture the initiation of the PD, a random event, it is necessary to employ an image-preserving optical delay to store the image information in air until the camera can be triggered by the random event

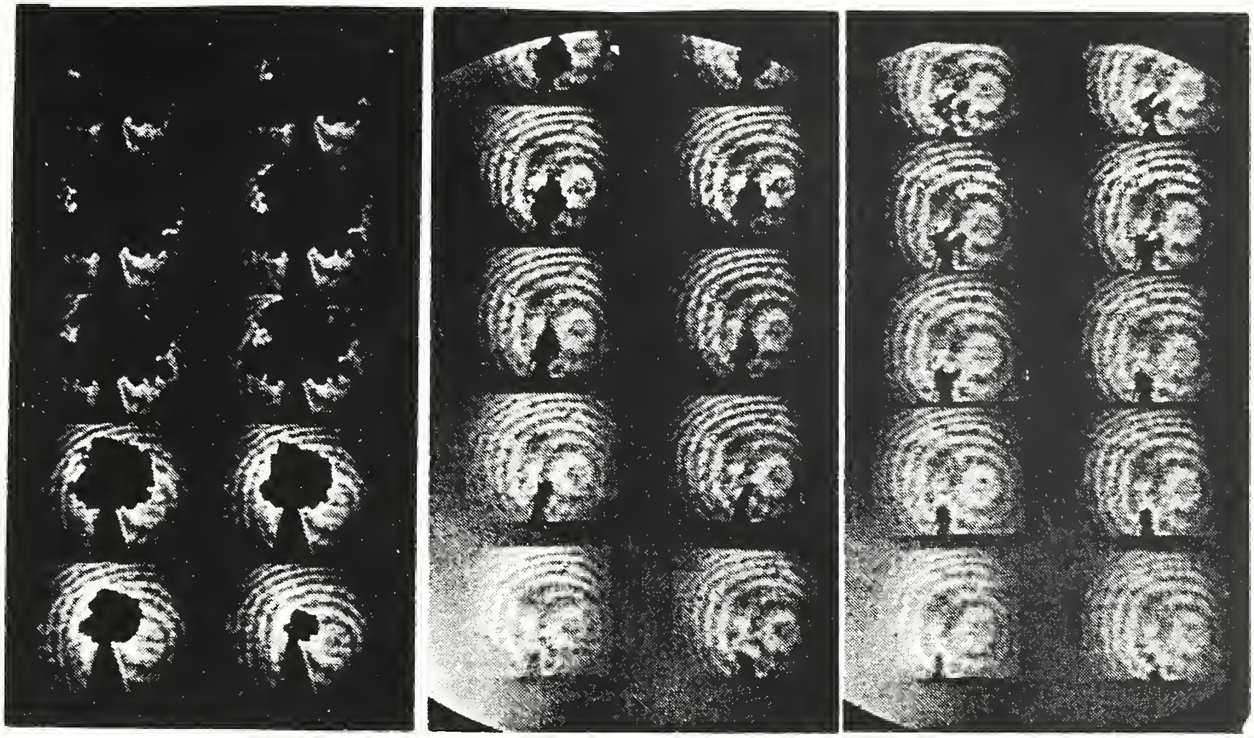

Figure 31. Partial discharge photographs, from left to right: 27 kPa, 2 fs between frames; 0.1 MPa, 200 ns between frames; 0.2 MPa, 200 ns between frames.

and begin taking pictures.

The reason for using hexane is that a large body of experimental results already exists in the literature and the liquid is well-characterized both physically and chemically. Liquids like transformer oil are of more practical interest but suffer from not being well-characterized chemically or physically and large variations can be seen from barrel to barrel. It is anticipated that the results established for hexane or any other simple liquid will be readily applicable to all liquids. However, at this early stage we want to avoid as many complications as possible which arise from the selected liquid.

The results of this experimental study confirm that a PD is a gaseous chamber – a bubble. In general, the size of the bubble decreased with an increase in pressure, and the amount of charge injected during the expansion of the bubble decreased as the pressure increased. Figure 31 shows PD growth at several pressures. The rings observed in each frame have nothing to do with the experiment; they arise from the interference of the laser beam at the surface of the image-converter camera tube. The region viewed by the camera in the direction the needle is pointing is 0.29 mm from one edge of the frame to the other. The smallest particle which could be discerned in the photograph is estimated to be 5 μm in diameter. The growth of the PD near the vapor pressure of hexane is continuous, that is, the PD bubble keeps growing, eventually breaking up into several smaller bubbles which leave the area of the gap and are readily visible to the eye. For higher pressures, the PD is seen to collapse back on itself with at most a few very small bubbles leaving the region of the gap. These small bubbles leave the region of the gap and quickly dissolve into the liquid.

The initiation of PD's under the application of impulses has been studied before in nitrobenzene [84]. A hypothetical model for streamer initiation was proposed: There is a favorable site on the tip of a needle at which charge injection is large. As the field increases, the "jet" of charge injection increases until the joule heating of the liquid causes a bubble to initiate. The bubble grows and branches becoming the streamer. The rapid changing of a small portion of a liquid into a gas represents a small explosion in the liquid. The initial bubble would be at high pressure. This hypothesis explains the observation of an initial, spherical shock wave emanating from the tip of the needle at the moment of initiation as observed in many photographs of streamer growth under the application of impulses. To what extent this picture can be applied to PD's under the application of steady-state voltages remains to be seen.

Attempts have been made to apply various models to the growth of a PD [85]. Watson [86], Alexeff [87], and Fenimore [88] have developed models which are based on Coulombic repulsion of the charges on the surface of the bubble or the heating of the gas within the bubble due to the discharges as the bubble expands. An additional complication would be the initial explosion of the liquid into a gas at the initiation site. It is difficult to determine exactly what process is causing the expansion of the PD bubble. It may be a combination of the initial explosion, Coulombic repulsion, heating of the gas within the bubble, and further vaporization of liquid at the boundary of the bubble. Each of these processes may play a role, and the respective importance of each process may change as the PD develops into a streamer and the streamer grows across the gap. Only further quantitative results will provide insight to distinguish or combine these pictures.

Regarding future developments: At the beginning of the experiment, attention was paid to particulate content of the hexane. Ultrapure hexane was used at first in combination with circulating the hexane through a $1-\mu$m polytetrafluoroethylene particle filter. With such purity, it was difficult to observe any partial discharges. When the cell system was refilled with spectroscopic grade hexane and no particle filtration was attempted, partial discharges were readily observed. This suggests that small particles play an important role in the generation of partial discharges. To explore this area further, a redesigned high-magnification optical system will be needed in order to provide micron or sub-micron optical resolution. Such a system will be implemented next year. In addition, a calibration of the amplifier system will be made to determine the charge deposited in the PD during its growth. It is hoped that these data will provide some quantitative measure to guide the development of a model for PD generation and growth.

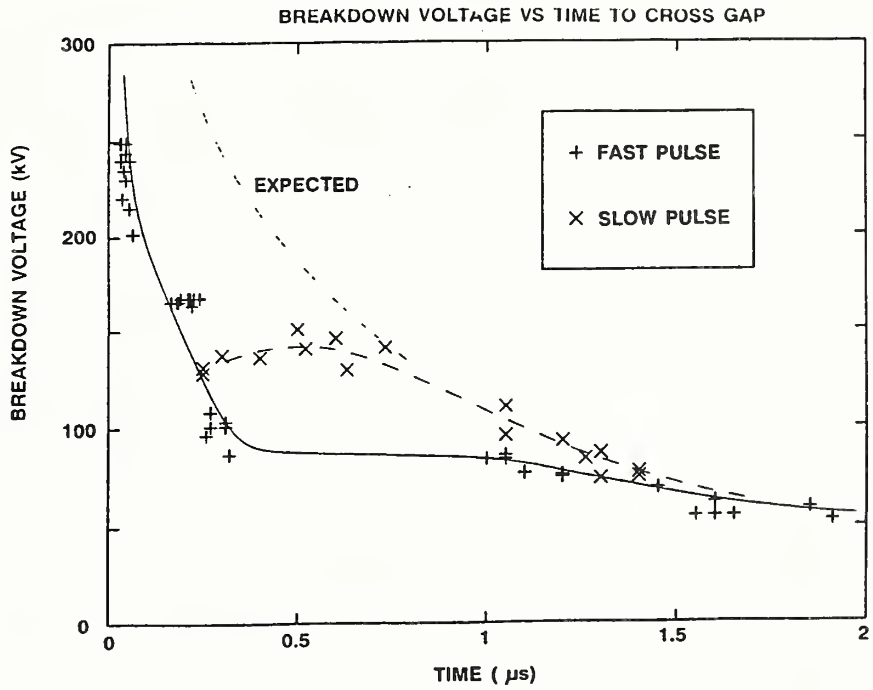

Figure 32. Liquid breakdown data showing the decrease in breakdown voltage as the time-to-breakdown is reduced.

3.3 Nanosecond Breakdown At A Liquid-Solid Interface

In previous reports it has been shown that breakdown characteristics in the sub-microsecond regime differ from those in the microsecond regime. Specifically, the breakdown voltage does not increase steadily as the time-to-breakdown decreases. In the case of a needle-sphere electrode system with a 5 mm gap in transformer oil, as the breakdown time decreases to the range of a few microseconds, the breakdown voltage begins to decrease. When the breakdown times become significantly shorter than one microsecond, the breakdown voltage again increases as the breakdown time decreases, as seen in Fig. 32. An explanation was proposed: As the voltage increases, the streamer spends less time in the slower propagation modes. If the voltage increases fast enough, the slower modes may be circumvented almost entirely and the streamer is exclusively comprised of fast phenomena. It is because of this faster mode that the breakdown voltage decreases slightly as the time-to-breakdown is made to decrease. However, the decrease is short-lived, and the breakdown voltage again increases dramatically when the streamer is entirely in the fast mode and the time-to-breakdown is forced to decrease further.

It is believed that the faster propagation modes are more energetic in some sense than the slower modes. A piece of paper insulation may stop the slower mode, but

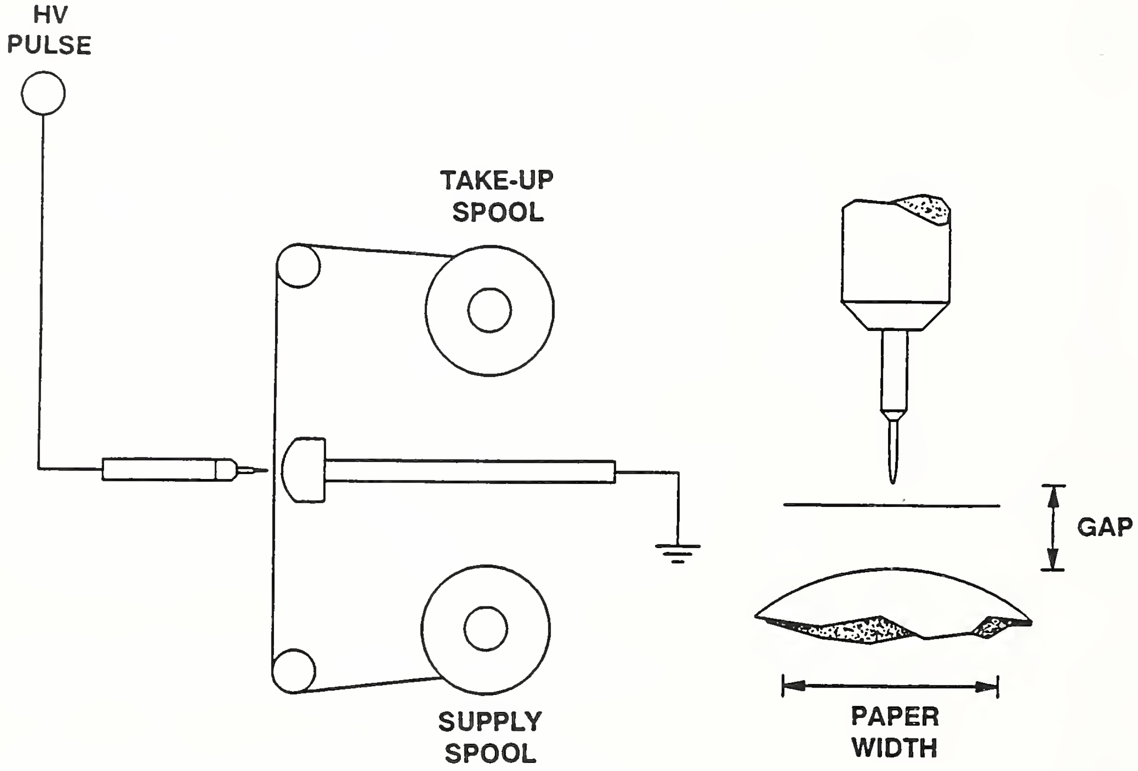

Figure 33. Experimental configuration of paper interface placed in the gap between the needle and the sphere electrodes.

it may not stop the faster mode. If the fast mode can be initiated early in the life of the streamer due to the application of a fast, nanosecond rise-time pulse, the paper insulation may fail at a lower voltage than for a slower, microsecond pulse where only a slow process would be generated. It is the purpose of this experiment to shed some light on the difference of fast and slow streamer processes in their interaction with interfaces.

The present experiment adds a paper interface between the needle electrode and the spherical electrode (a strip 13 mm wide having a thickness of 64 μm). The position of the paper in the gap can be varied relative to the needle and the sphere, (see Fig. 33). An image-converter camera is used to photograph the time-evolution of the streamers in the gap, and an image-preserving optical delay can be employed to temporally isolate the faster phenomena. We were unable to determine whether or not a fast pulse can break down an interface at a lower voltage than a slow pulse can. There were two difficulties: 1) The slower streamers existed long enough that they could spread to the outer edge of the paper and then jump across the gap, and 2) the breakdown voltages needed to completely test the hypothesis exceeded the 300 kV peak capabilities of the present system, (see Fig. 34). Thus, more work will

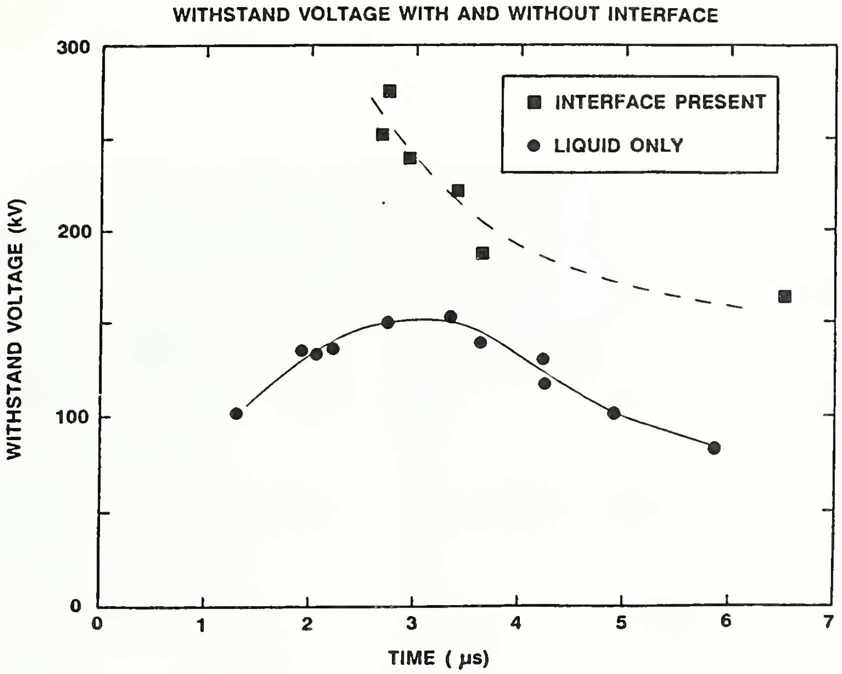

Figure 34. Increase in breakdown voltage with interface present using 7 μs wide pulse.

be necessary to determine the answer. However, there is some evidence that fast pulses can produce anomalously low failures of an interface.

Figure 35 shows three photographic sequences. The left two are taken under identical voltage conditions of a 7 μs width pulse having a peak of 103 kV. The only difference is the position of the interface. The left photograph shows a fast streamer quickly penetrating the interface which is far away from the tip. In the middle photograph, the slower streamer process is stopped by the paper interface which is near the tip of the needle. The right photograph shows the penetration of the paper by a fast event where the camera operated at ten times the framing rate of the other two photographs and the pulse had a peak voltage of 178 kV. In the right photograph the liquid was purposely made dirty by generating many breakdowns in the oil thus producing a large number of fine carbon particles suspended in the oil. The difference between the fast event in the left photograph and the fast even in the right should be noted: the particles tend to reduce the number of branches of the fast event and may speed it up. The extent of the slow event varies from shot to shot before the onset of the fast event. In general, the time spent in the slower mode is reduced with the addition of particles or increasing the rise-time of the voltage pulse.

What is clear from these results is this: 1) If a fast streamer is generated, it readily punctures the paper insulation. 2) The presence of dirt enhances the probability of

Figure 35. Photographic sequences showing interaction of streamers with the paper interface. Two left photographs have a frame spacing of 500 ns, the right photograph has a frame spacing of 50 ns.

initiating a fast streamer and the speed of the fast streamer is increased. 3) Fast streamers are very difficult to initiate in clean liquids without first producing the slow streamer process. How any of these factors combine in a practical insulation system remains to be seen. If partial discharge activity is present in power apparatus, then there are particles being generated and the above results would indicate an increased susceptibility to anomalous failure due to fast pulses which generate the fast streamer processes. However, more work is needed to isolate the parameters which may combine to permit an anomalous failure.

3.4 An Image-Preserving Optical Delay

An image-preserving optical delay (IPOD) is described which delays an image from reaching a high-speed camera for several hundred nanoseconds. This device permits the photography of phenomena preceding fast, random events by using the event as a trigger for a high-speed camera.

The need for delayed images arises when information is desired concerning the development of very fast, random phenomena having durations from nanoseconds to microseconds. Consider a random event which occurs during an interval of time. The longer the time interval, the more difficult it is to synchronize a high-speed camera with the event under study. Delaying the image from reaching the camera permits the camera to photograph events back in time. If the image delay is long enough, the camera photographs phenomena which preceded the event triggering the camera. Several ways have been successfully employed to delay an image [89, 90]. This paper presents another alternative which has the potential of producing delays up to a few microseconds in a relatively small space.

Details of the Apparatus:

Figure 36 shows the use of the IPOD in an experiment to observe photographically electrical breakdown in liquids. Such breakdown processes are examples of fast, random phenomena like lightning. A high-voltage (HV) pulse having a duration of 7 fs is applied to a needle-sphere electrode system with a gap separation of 7 mm. The electrodes are placed within a cell (not shown) filled with liquid hexane. A xenon flashtube provides illumination to permit shadowgraph photography using an image-converter camera which records the time evolution of the breakdown process. At some random time during the application of the electrical pulse, a streamer will begin at the tip of the needle and grow across the electrode gap. When the streamer reaches the grounded spherical electrode breakdown occurs. The camera is triggered by means of a pulse transformer which senses the high current pulse of several hundred amperes in the ground line generated by the breakdown. While the camera is preparing to take the first frame, the image of the process occurring in the electrode gap is delayed by

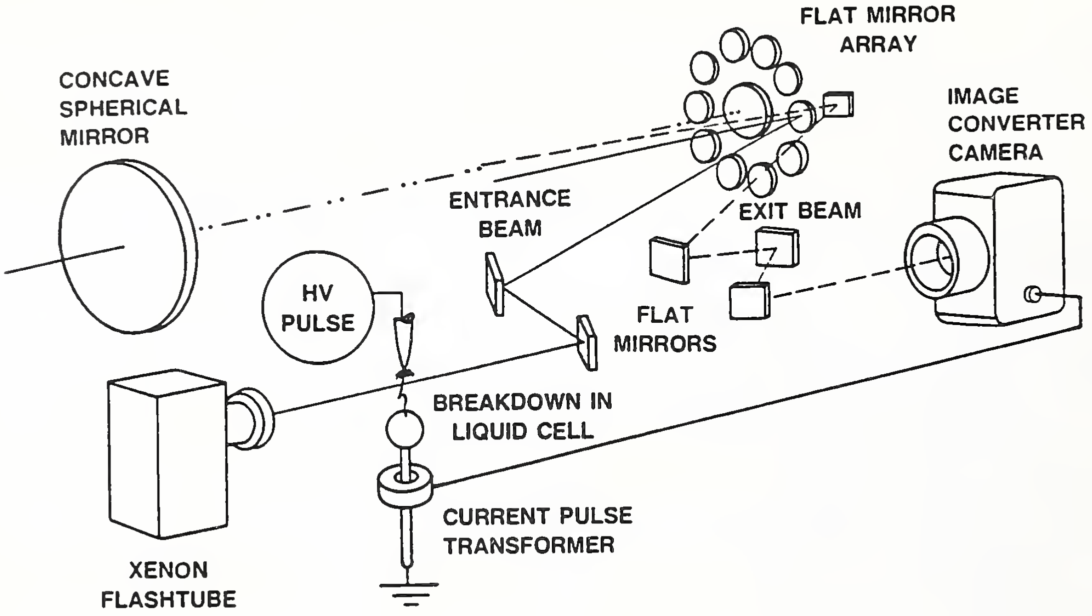

Figure 36. Image-preserving optical delay orientation in a liquid breakdown experiment.

the IPOD so that when the camera begins taking pictures, it records prebreakdown images.

The IPOD is the arrangement of mirrors between the object (the region between the electrodes) and the camera. Its main elements are an array of flat mirrors and a large-diameter concave spherical mirror. The image of the object is repeatedly refocused and collimated by the interplay of the flat mirror array and the spherical mirror. The operation of the IPOD is best understood by considering an equivalent lens system each of which has a focal length f. When an object is placed a distance 2f from a lens, an unmagnified image will be produced at a distance 2f on the other side of the lens. If another lens is placed at the location of the image, the second lens only serves to collimate the light from the first lens. Repeating this two-lens arrangement with a separation of 2f provides a means of relaying an image over a long distance with unit magnification. In the IPOD, the lenses are replaced with the concave mirror, and the flat mirror array serves to direct the repeated reflections.

The alignment of the IPOD is accomplished by placing the center of the flat mirror array at the on-axis focal point of the concave mirror. Alignment is accomplished using a He-Ne laser by passing it through the electrode gap to the two flat entrance mirrors which steer the beam into the array. The two flat entrance mirrors are adjusted so that the distance from the object to the first mirror of the array (see Fig. 37) is equal to one focal length of the concave mirror. Since off-axis imaging from a mirror introduces astigmatism, it is necessary to exploit the entire surface of

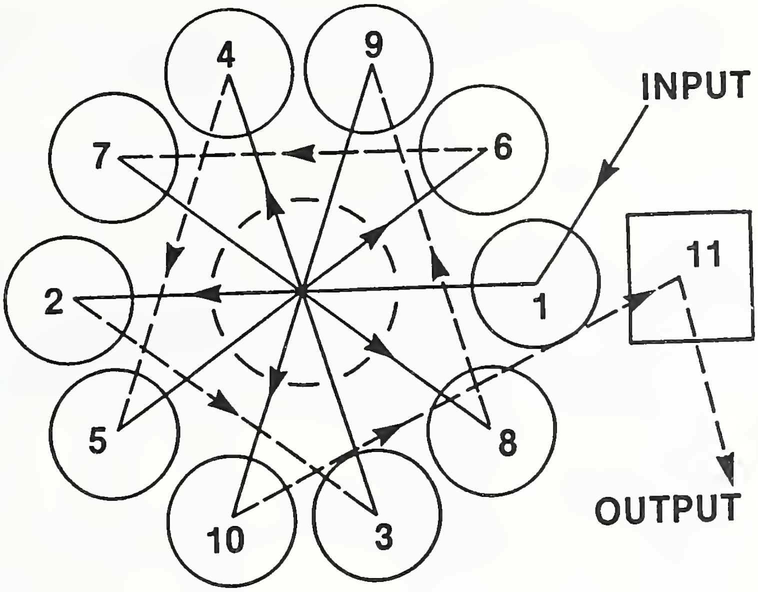

Figure 37. Flat mirror array as viewed from the concave mirror. The solid lines represent the long path, and the dashed lines, the short path. The central mirror of the array is depicted by a dashed circle.

the concave mirror in a symmetrical manner so that the net astigmatism associated with the final image after the array is almost zero. This is accomplished in the following manner: Mirror #1 is adjusted so that the reflected beam hits the concave mirror along a line which parallels the axis of the concave mirror. The return beam will then hit the central mirror of the array. The beam returns to the concave mirror and is reflected back to mirror #2. This is referred to as a long path. Mirror #2 is adjusted to reflect the beam back to the concave mirror so that the return beam hits mirror #3, a short path. The long path hits the concave mirror twice, the short path hits it once. This sequence is repeated until the output mirror #11 is reached, then the beam is directed into the image-converter camera by the flat exit mirrors. The distance between mirror #11 and the photocathode of the camera is one focal length of the concave mirror. It must be noted that the short path to mirror #3 skips the mirror adjacent to mirror #1. Only by skipping the adjacent mirror in this manner for each short path can it be assured that the beam symmetrically passes across the concave mirror equally in all directions whereby astigmatism is virtually eliminated.

In like manner, an IPOD can be made with $6, 10, 14, 18, 22, ... 4n+2 = N(n = 1, 2, 3, ...)$ mirrors in the circle around the central mirror and with one extra mirror $(N + 1)$ outside the circular array. This produces $3n + 1$ images on the concave mirror and one image, the final image, outside the array. A total of $3n + 2$ images are produced over a path length of $(12n+8)f$. For such an array, the long-path-short-path sequence

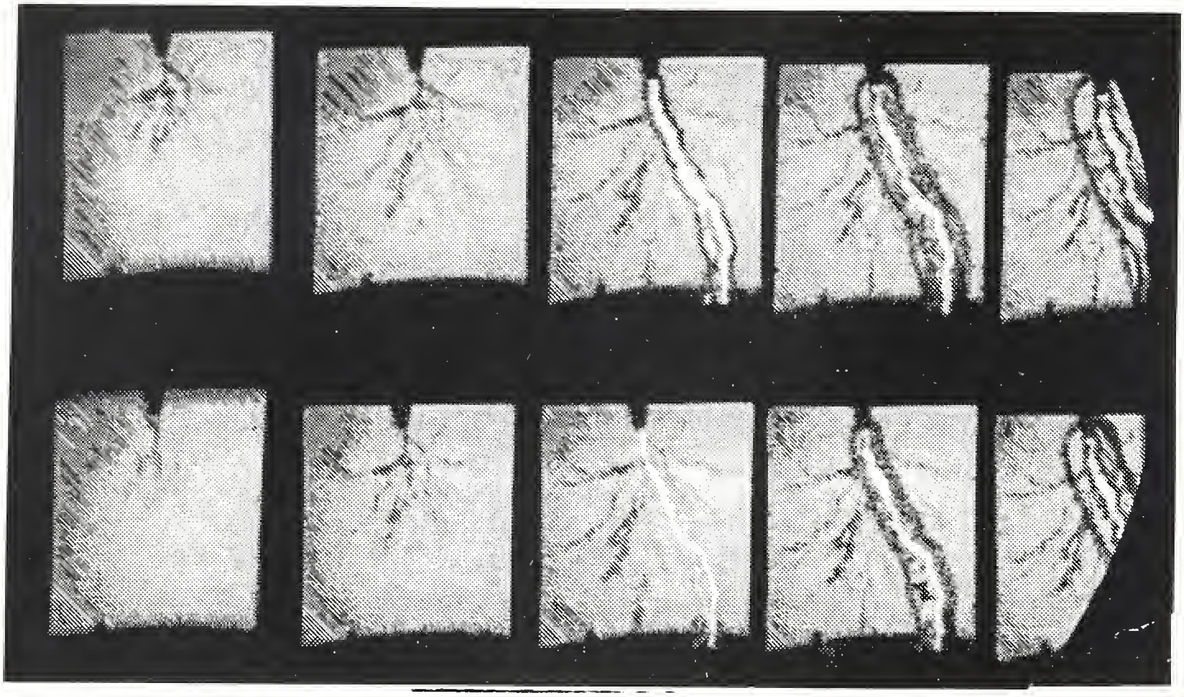

Figure 38. Results of the image-preserving optical delay, 50 ns between frames.

must always be maintained where the adjacent mirror is skipped as described above. In the case of the IPOD presented here, the focal length of the 30-cm diameter concave mirror is f = 372 cm; the flat mirror array contains 10 (with n = 2), 2.5-cm diameter, small mirrors around a 5-cm diameter center mirror. The total path length from object to final image is 119 m which provides for an image delay of 397 ns. The central array mirror is larger than the circumferential mirrors to expedite the alignment process.

The IPOD functions as a long focal-length mirror with a small aperture. The resolution of the device is limited not by the large-diameter mirror, but by the circumferential array mirrors acting as apertures. With the 2.5-cm mirrors, a resolving power of the IPOD can be calculated and measured to be approximately 5 line-pairs per millimeter (lp/mm). To improve the net resolution of the IPOD without replacing the small array mirrors with larger ones, it is a simple matter to magnify the image before the IPOD, then demagnify it by a factor of two or more after the IPOD. The net resolution will be 10 lp/mm or better at the camera.

Figure 38 shows the results of using a premagnification of 5.4X before the IPOD and a demagnification of 2X after the IPOD. Most of the frames shown in the photograph were stored in the air by the IPOD: The camera was triggered a few nanoseconds after the breakdown occurred, at this point the phenomena in the gap appeared as shown in frame five. The camera began taking pictures approximately 150 ns later, when the process had advanced to the stage shown in frame eight or nine. Because of the IPOD delaying the arrival of the image to the camera, it is able to photograph the phenomena before the camera was triggered, that is, the IPOD permits the camera "see" back in time several hundred nanoseconds.

The success of the IPOD depends upon the quality of the mirrors used. Because of the many reflections involved, it is necessary to use high-reflectivity, dielectric mirrors. There is a reflection at each distance f for a total of $12n + 7$ reflections ($n = 2$ for 10 circumferential array mirrors, see above). Adding an additional three entrance mirrors and three exit mirrors results in a total of $12n + 13$ reflections. If each mirror had a reflectivity of 97% (accounting for dust, scratches, etc.), the transmittance of the IPOD would be 32%.

Adding more mirrors to the circumferential array will increase the delay but reduce the transmittance. If the 10 small mirrors were replaced with 14 ($n = 3$) mirrors of 5-cm diameter using the same 372-cm focal length concave mirror, a delay of 546 ns would be provided with a resolution of 10 lp/mm, a resolution commensurate with or better than many high-speed recording devices. However, there would be up to 49 reflections (using six insertion mirrors) which would provide for a transmittance of 22% through the IPOD assuming 97% reflectance of the mirrors. It may be possible to increase the delay further by making two concentric circumferential arrays. For example, a 10-mirror inner array with a 16 mirror outer array would provide for a 993 ns delay. However, a small amount of astigmatism will be introduced since a way has not yet been discovered to exploit such a compound array in a fully symmetrical manner. Such an array ($n = 6$, 26 circumferential mirrors) would have 85 reflections giving a transmittance of 7.5% with a mirror reflectance of 97%. The delay can also be lengthened by increasing the focal length of the concave mirror. However, to avoid a loss of resolution, the diameter of the mirrors must be increased proportionately.

4. FAST TRANSIENT PHENOMENA

Task 05

Gerald J. FitzPatrick, Robert E. Hebner, Ronald H. McKnight, John E. Lagnese,
Charles Fenimore, and Yixin Zhang
Electricity Division
National Institute of Standards and Technology

4.1 Introduction

The design of free-standing voltage dividers that are used to measure lightning and switching surges in power equipment testing generally result in dividers of large physical dimensions in order to withstand voltages from several hundred kilovolts to megavolts. These devices typically exhibit resonances due to stray capacitances and inductances associated with the leads connecting them to the voltage source. Problems arise when there is significant energy in the pulses to excite these inherent resonances, distorting the measurement. The IEC [91] and IEEE [92] standards concerning the use of these dividers for high voltage impulse measurements recommend evaluation of their measurement fidelity through step-response tests and alternatively, through simultaneous comparison measurements made with a well-characterized reference device. There is no guidance provided by the standards with regard to interactions between dividers, i.e., how resonances due to the presence of one of the dividers in the circuit affects the measurements made with the other. These interactions affect the measurements of peak voltage and consequently the evaluation of the scale factor for the divider under comparison.

The work reported here addresses these problems in the measurement of fast voltage transients through an assessment of the magnitude of divider interactions in simultaneous measurement configurations and makes recommendations for their minimization. This study is reported in greater detail in reference [93]. The results show that interaction effects are most significant in step-response measurements and less important in the measurement of standard-lightning impulses. The following sections describe the purpose, experimental design, and results of the study on divider interactions in comparison measurements.

4.2 Interactions Between Two Dividers Used in Comparison Measurements

4.2.1 Introduction

The accuracy of an impulse measurement is determined by the dynamic behavior of the complete electrical system including the divider, the test object, the impulse generator, interconnecting leads, recording instrument, and chopping gap, if used. IEC [91] and IEEE [92] standards concerning impulse voltage measurement techniques recommend that step-response parameters be evaluated as one approach to characterize the measuring system's dynamic behavior. This approach has difficulties since systems having step-response parameters within the limits prescribed by the standard can still have unacceptable errors in the actual impulse measurements [94]. Alternatively, it is recommended that evaluation be made through a simultaneous comparison measurement between a standard reference divider and the one to be evaluated. IEC publication 60–4 [95] calls for the independent reference system to have overall measurement errors of less than 1% over its range of use. This study was undertaken because, although the standards specify less than 1% measurement uncertainty, no indication is provided concerning the types of interactions between dividers and no guidance given on what precautions are to be taken to insure that they do not affect the divider comparison.

Previous comparisons between dividers where one divider was used as a standard to determine the accuracy of the other have been published [96–99] including some which discussed divider interactions. In this study, interactions arising from the simultaneous use of two dividers and resultant distortion of the signals have been measured. Two resistive dividers considered to be of reference quality, a pure capacitive divider, and a damped capacitive divider, were used. The comparisons were made using both independent and simultaneous measurements of the step responses, standard-lightning impulses, and chopped-lightning impulses. The experimental approach is described in the next section.

4.2.2 Experimental Approach

The two resistive divider measuring systems used in this study are designated NBS1 and NBS3, rated at 1 MV and 0.3 MV, respectively, for chopped-lightning impulses. Both dividers have high-voltage arms consisting of 10 kΩ and low-inductance resistors. Each has a top ring to grade the distributed capacitances. The capacitances for the top rings measured to ground are 69 pF for NBS1 and 22 pF for NBS3.

Two laboratory model capacitive dividers were constructed to obtain responses that were very different from those of the resistive dividers, NBS1 and NBS3. One is a pure capacitive divider having a slow rise time and 46% overshoot. The second is a damped capacitive divider with a high-impedance arm consisting of a total capacitance of 430 pF and total resistance of 510 Ω in series. Its step-response rises very slowly and has no overshoot.

The experiments utilized two different pulse generators: a triggered-gap generator that produced pulses of several kilovolts in amplitude and one using silicon-controlled rectifiers (SCR's) for pulses up to 400 volts. The generators produced both full standard lightning and chopped-lightning impulses. Two identical scan-converter digitizers with a 400 MHz bandwidth and stated digital resolution of 9 bits were used for the step-response measurements. For the impulse voltage measurements, a third digitizer having a 125 MHz bandwidth was added. Computer programs were written to calculate the time parameters from the step-response and lightning-impulse digital data records according to the standards [91, 92]. The data were smoothed using cubic splines under least-squares constraints.

A mercury-wetted relay having a nanosecond closure time was used with a dc-voltage supply to generate the step-response signals. The measuring system was charged to a preset dc voltage and then discharged to ground through the relay.

4.2.3 Step Response Measurements

Step responses of the measurement systems were determined using the horizontal-loop and square-loop configurations. For the horizontal-loop configuration, shown in Figure 39, the signal source was mounted on a platform at a height of 2 m so that the connecting lead between the source and the divider ran perpendicularly to the divider's vertical axis. The source was connected to the ground plane by a low-inductance copper strip, labeled G in the figure. The angular separation between the two horizontal divider leads (θ) was about 60 degrees and the distances, between dividers (ℓ_c and ℓ_a) were 3.2 m. Preliminary measurements using angular separations of 60, 90, and 180 degrees showed that changing angular separation made little difference in the results.

For the square-loop configuration, the signal source was placed on the ground plane and the connecting lead was run vertically up from the generator to a height of 2 m and then across horizontally to the divider. The same circuit geometry as used for the horizontal loop configuration was preserved, but with the signal source at a different location in the loop. The horizontal connecting leads were 4.6 m long for the NBS1 divider and 3.8 m long for the others. A 50 Ω attenuator was connected to measure the output of the signal source directly. The same circuit geometry as shown in Figure 39 was used for the full- and chopped-lightning impulse measurements but with a different signal source.

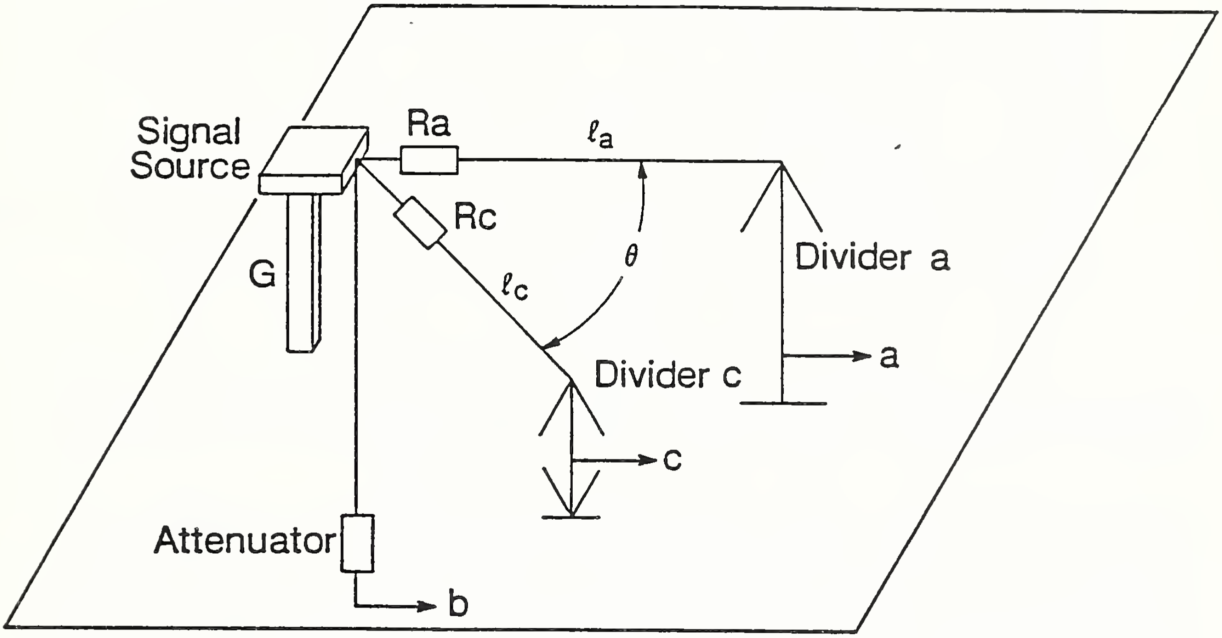

Figure 39. Experimental horizontal loop configuration used to investigate simultaneous measurements using different dividers. Shown are the two divider systems and the damping resistors (R_a and R_c) used with each individual divider. For the square-loop configuration, the signal source is placed on the ground plane.

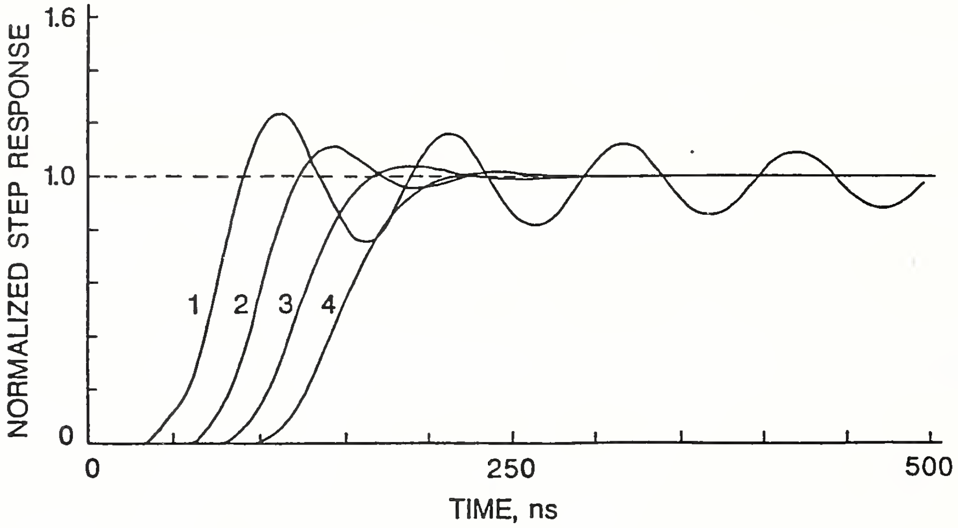

Figure 40. Step-response of the independent NBS3 divider for different damping resistors, R_{d3}: (1) $R_{d3} = O\,\Omega$; (2) $R_{R_{d3}} = 150\,\Omega$; (3) $R_{d3} = 350\,\Omega$; (4) $R_{d3} = 550\,\Omega$.

Thirteen different test configurations were investigated. During preliminary tests, measurements were made with the dividers separated by 1.65, 3.8, and 8.6 m. No significant changes in interaction effects were observed for divider separations of 3.8 and 8.6 m. All the experiments reported here were performed with divider separations of 3.8 m.

Figure 40 shows step-response measurements for the independent NBS3 divider in the horizontal-loop configuration, i.e., with no other dividers present in the circuit. The oscillations around unit amplitude result from the resonance produced by the inductance of the high-voltage lead and its associated capacitance along with the capacitance of the top ring of the divider. For the NBS3 divider, this top ring capacitance is smaller, requiring a larger resistance for critical damping of the step-response and resulting in a higher resonant frequency than that for NBS1 which has a larger top ring capacitance. The waveforms in this figure and in subsequent figures have been displaced along the time axis for better comparison.

The step-responses of the capacitive dividers are shown in Figure 41. The pure capacitive divider had highly resonant behavior with a resonant frequency of about 2.3 MHz while the damped capacitive divider had a very slow rise time, but no overshoot. Note that the time scale of Figure 41 is four times greater than that of Figure 40. Table 5 summarizes some of the time parameters including T_n (experimental response time), T_α (partial response time), and T_0 (initial distortion time) which were evaluated according to the present standards [91, 92] for the two NBS resistive dividers, NBS1 and NBS3, as a function of the damping resistor and for the

Table 5.

R_d (Ω)	T_n (ns)	T_α (ns)	T_o (ns)	Overshoot (%)
		NBS1		
0	23	27	2.9	39
50	29	30	2.4	28
150	33	36	2.7	14
250	41	44	1.7	6
400	52	53	1.8	2
		NBS3		
0	19	17	2.6	24
150	23	20	1.8	11
350	28	29	1.3	3
550	36	36	0.8	2
		Damped Capacitive Divider		
0	128	128	−0.7	0
		Pure Capacitive Divider		
0	−23	46	0	49

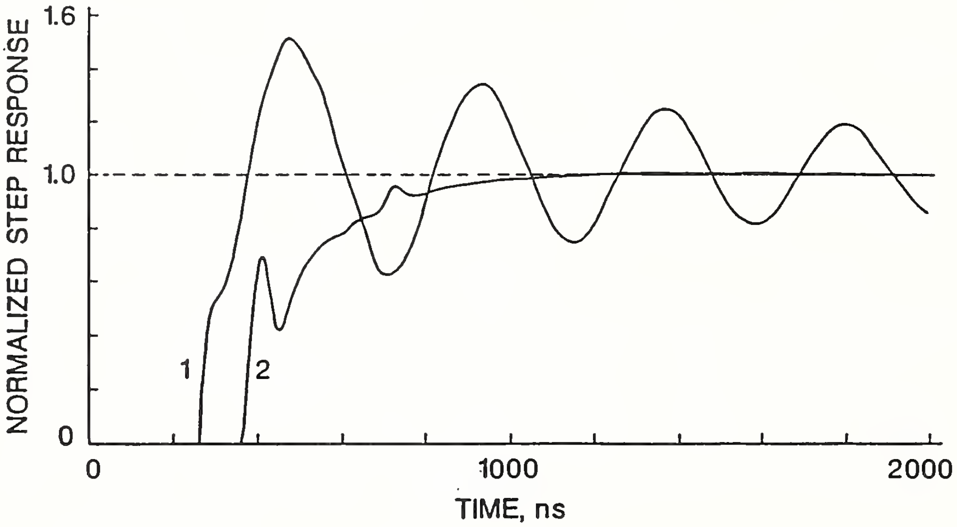

Figure 41. Step-responses for (1) the pure capacitive divider, $R_{dc} = 0\,\Omega$; and (2) the damped capacitive divider, $R_{ddc} = 0\,\Omega$.

damped and pure capacitive dividers with no damping resistor.

Figure 42 shows examples of step-response measurements for selected configurations of NBS1 with other dividers. For the results shown in Fig. 42(a) no damping resistors were used while in Fig. 42(b), NBS1 was critically damped. Independent step-response measurements are shown for reference. It is clear that there are interactions between the dividers, and that the degree of interaction depends on the damping resistors. The pure capacitive divider had the greatest influence on the step-response measured for NBS1 for the undamped case. When NBS1 was critically damped, there was strong interaction observed with each of the other undamped dividers. If both dividers were critically damped, then no interactions were observed in the step response. The distance between the dividers did not greatly affect the response until the two dividers were located less than 1 m apart.

Undamped oscillations in the individual loops are the main source of interaction between the dividers. The divider system which has the larger resonance amplitude has the larger effect on the other divider. Among the four dividers, the pure capacitive divider had the largest resonance amplitude. The damped capacitive divider has no resonant behavior so it was not expected to and did not greatly influence the step responses of any of the other three dividers.

Figure 43 shows examples of step-response measurement for NBS3 combined with NBS1 for different damping conditions. The step-response for NBS3 is significantly distorted by an undamped NBS1 as seen in Fig. 43(a) as is the response for a critically damped NBS3 (see Fig. 43(b)).

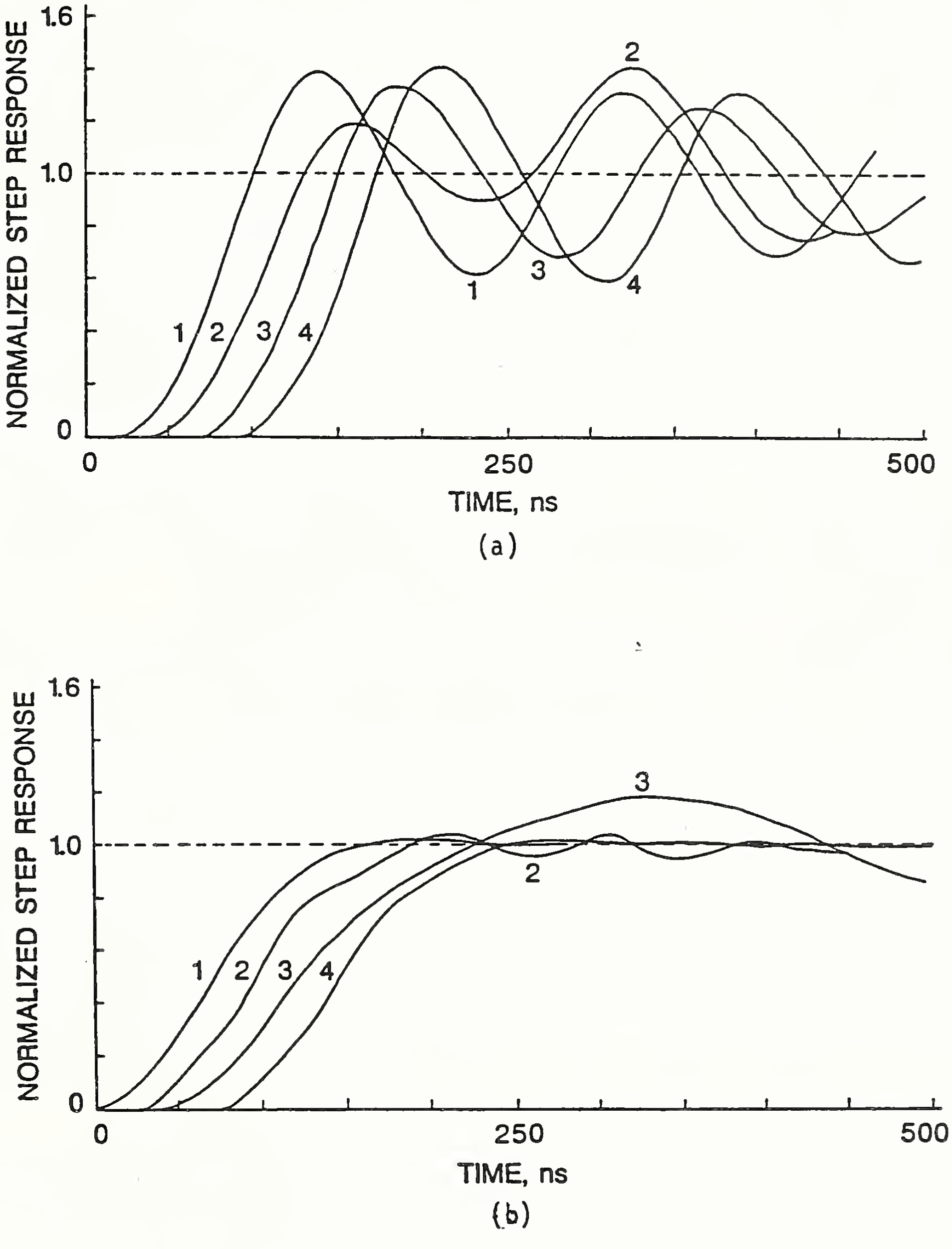

Figure 42. Comparison of independent and combined step-responses for NBS1.

(a) $R_{d1} = 0\,\Omega$
  (1) Independent divider
  (2) Combined with pure capacitive divider, $R_{dc} = 0\,\Omega$
  (3) Combined with damped capacitive divider, $R_{ddc} = 0\,\Omega$
  (4) Combined with NBS3, $R_{d3} = 0\,\Omega$
(b) $R_{d1} = 400\,\Omega$
  (1) Independent divider
  (2) Combined with NBS3, $R_{d3} = 0\,\Omega$
  (3) Combined with pure capacitive divider, $R_{dc} = 0\,\Omega$
  (4) Combined with the damped capacitive divider, $R_{ddc} = 0\,\Omega$

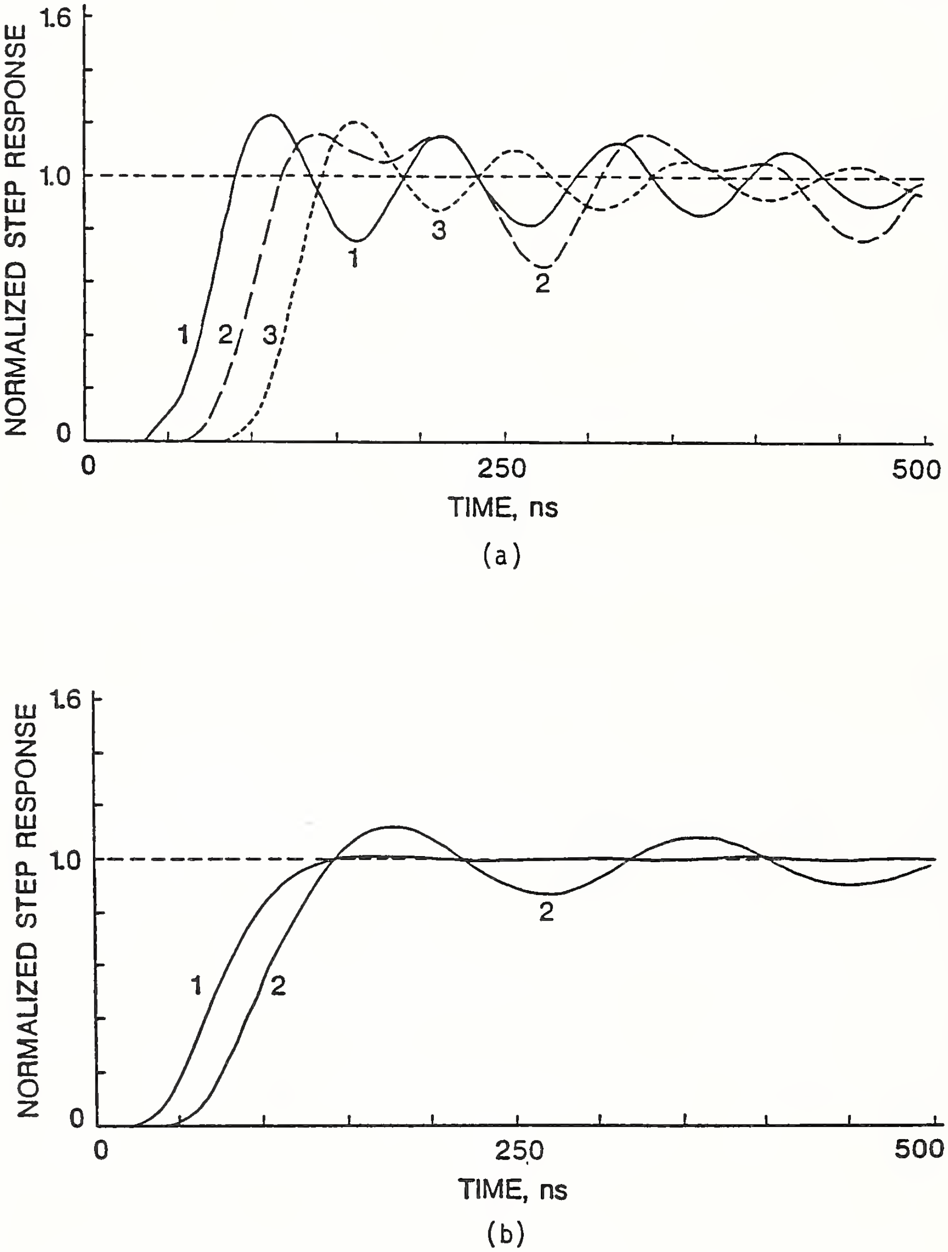

Figure 43. Comparison of independent and combined step-responses for NBS3.

(a) $R_{d3} = 0\,\Omega$

- (1) Independent divider
- (2) Combined with NBS1. $R_{d1} = 0\,\Omega$
- (3) Combined with NBS1. $R_{d1} = 400\,\Omega$

(b) $R_{d3} = 550\,\Omega$

- (1) Independent divider
- (2) Combined with NBS1. $R_{d1} = 0\,\Omega$

Using damping resistors appears to be a simple and efficient way to limit the interaction caused by oscillations, especially for the divider measuring system which has the greater overshoot. When both divider measuring systems had critical damping resistors, the response from a combined measurement was nearly the same as the response observed from an independent measurement.

It may not always be necessary to isolate the two measuring systems with damping resistors because the internal resistance of the impulse generator contributes to the damping of oscillations in the measuring systems. However, we do need to know the interaction between two divider measuring systems when they are simultaneously measuring the same signal, either a standard full- or chopped-lightning impulse. Observable interactions may introduce errors in a comparative calibration. By studying the step response for the dividers connected for a simultaneous measurement, we can obtain guidance as to which configurations offer the smallest interaction.

4.2.4 Equivalent Circuits of Measurement Systems

Equivalent circuit models were developed to evaluate the effects of the interactions of the dividers when an arbitrary voltage waveshape was applied. The model for the independent divider NBS1 with the step response generator is illustrated in Figure 44, for which the circuit parameters were found from either measurement or from calculation. A similar model was developed for NBS3. The calculated step response parameters evaluated with these models agreed to within 5% of the values evaluated from actual measurements for the NBS1 divider while the differences between the parameters evaluated from the circuit model for the NBS3 divider and from the actual measurements were slightly larger.

The equivalent circuits for the two dividers were connected as shown in Figure 45. The inductance of the common lead was estimated by calculation from the ringing frequency and measured inductance of the horizontal lead. A small coupling capacitance between the two dividers was also included in the model. This model was then used to simulate the simultaneous measurement of the step response.

In general, the calculations showed a slightly larger interaction than those actually observed, as seen in Figure 46 which shows the measured step response and that computed from the circuit model. It was shown through model iterations that both the inductance in the branch of the connecting leads common to both dividers and the coupling capacitance between them were necessary components in the circuit model to obtain agreement with the measured step responses, providing further evidence that the divider interaction is a strong consideration in comparison measurements.

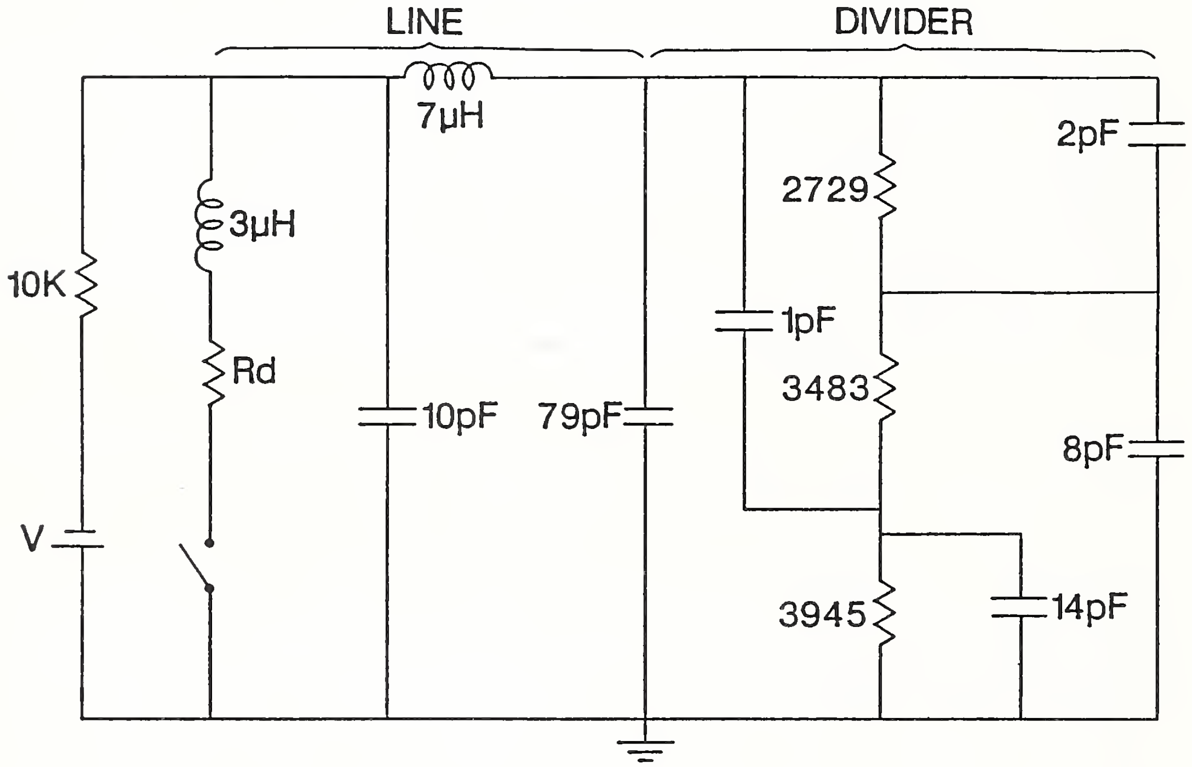

Figure 44. Equivalent circuit model for NBS1 divider. The circuit model includes parameters for the 4.6 m lead to the relay and dc supply used for the step response measurements. The 79 pF capacitance is that of the top ring of the divider and half of the lead.

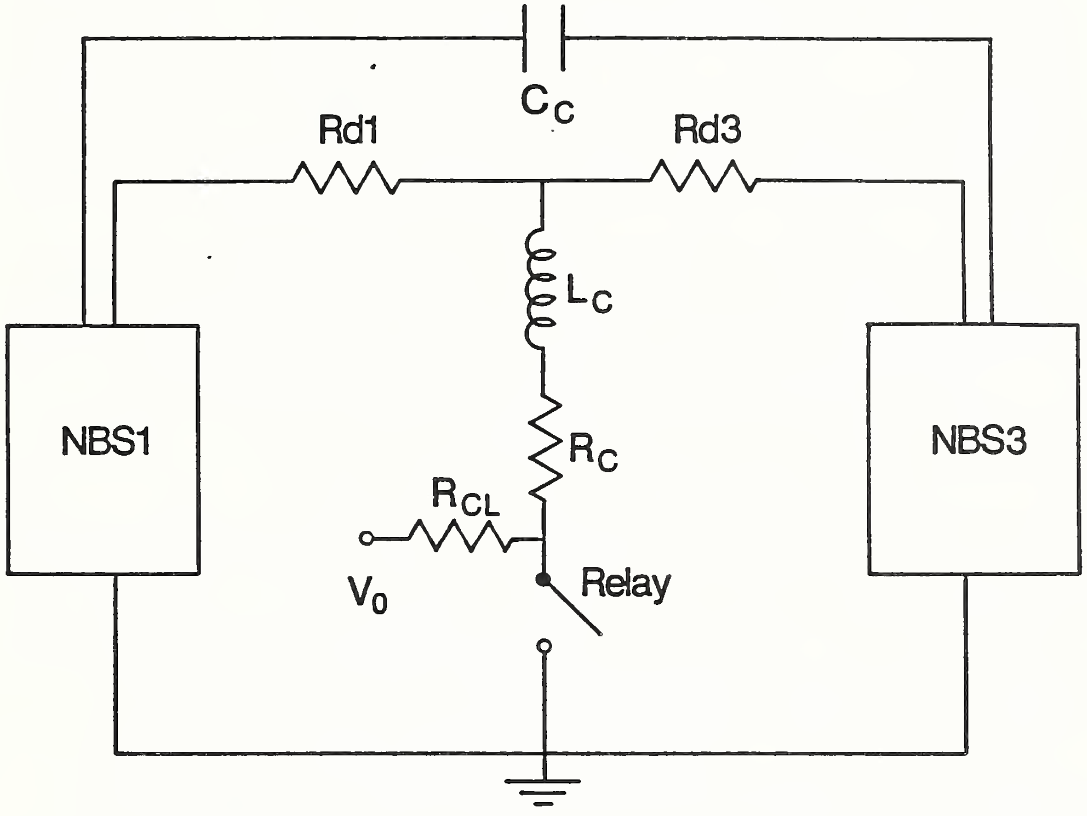

Figure 45. Equivalent circuit used in calculation of coupled response of NBS1 and NBS3. Blocks contain equivalent circuits for NBS1 and NBS3 (see Figure 44). Elements involved in coupling between dividers are C_C, L_C, and R_C. R_{CL} is a current-limiting resistor.

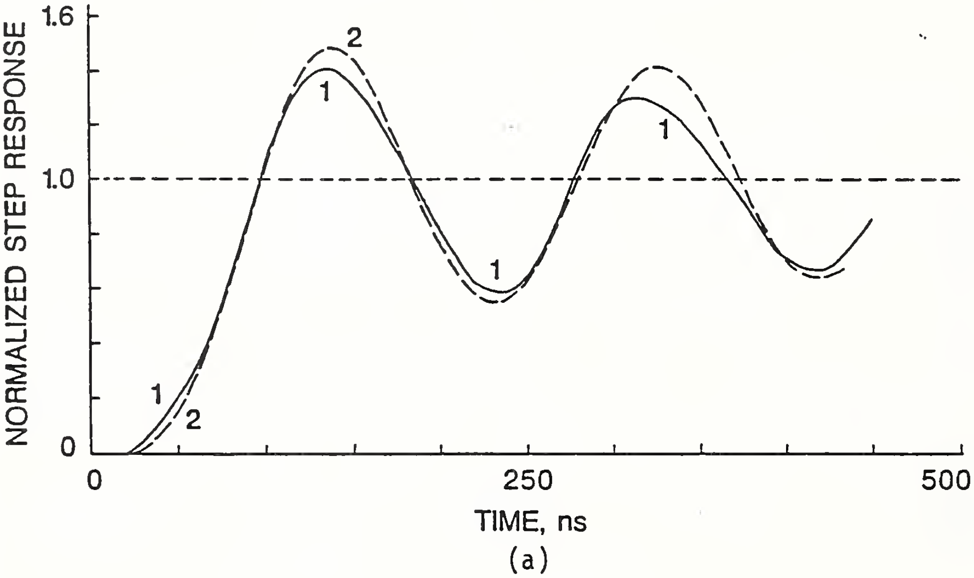

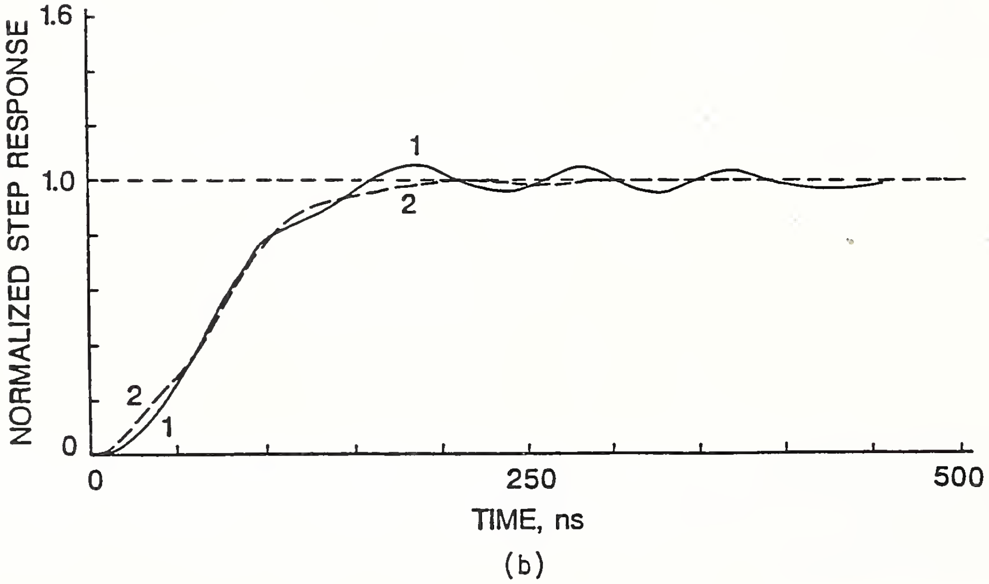

Figure 46. Comparison of calculated and measured NBS1 step responses for simultaneous measurements using NBS1 and NBS3.

(a) $R_{d1} = R_{d3} = 0\,\Omega$
  (1) Measured
  (2) Calculated

(b) $R_{d1} = 400\,\Omega$, $R_{d3} = 0\,\Omega$
  (1) Measured
  (2) Calculated

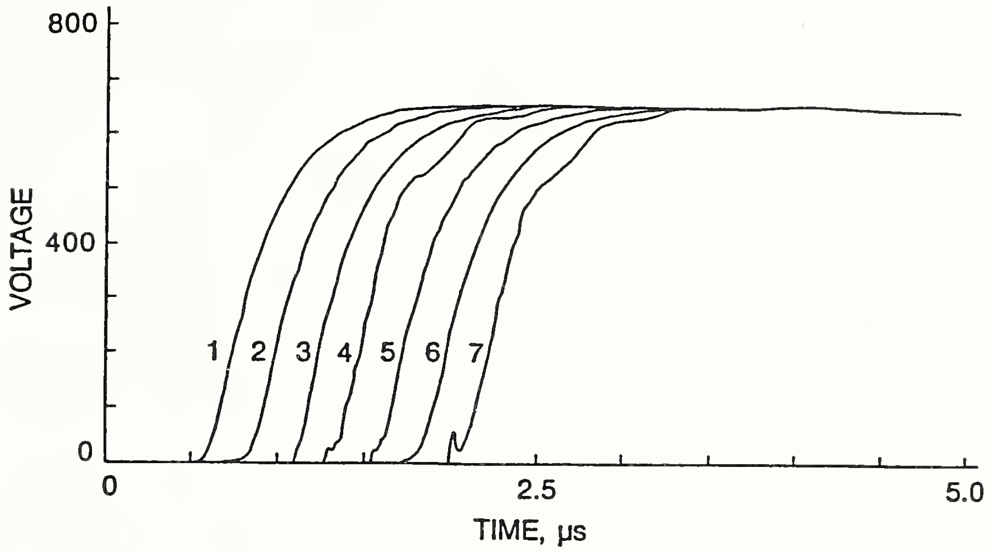

Figure 47. NBS1 divider, full standard lightning waveform.

(1) Input
(2) Independent divider, $R_{d1} = 0\,\Omega$
(3) Combined with NBS3 divider, $R_{d1} = R_{d3} = 0\,\Omega$
(4) Combined with pure capacitive divider, $R_{d1} = R_{dc} = 0\,\Omega$
(5) Combined with pure capacitive divider, $R_{d1} = 0, R_{dc} = 350\,\Omega$
(6) Independent divider, $R_{d1} = 350\,\Omega$
(7) Combined with pure capacitive divider, $R_{d1} = 350\,\Omega, R_{dc} = 0\,\Omega$

4.2.5 Standard Lightning-Waveform Measurements

The interactions between dividers is clearly seen in the step response measurements discussed in the previous section. Although these interactions can be mitigated through the use of damping resistors in the connecting leads at the generator end, it is not always feasible to do this in practice. Simultaneous measurements of full and chopped lightning waveforms for different combinations of dividers and circuit topologies were made to observe the interactions and how they can be minimized.

The output of the NBS1 divider for various combinations with other dividers and damping resistances for a full standard lightning impulse voltage of $0.95\,\mu s$ rise time and $60\,\mu s$ time-to-half-value are given in Figure 47. Although there are differences in the wavefront measured with the capacitive divider when compared to the independent divider, the virtual front time as evaluated in accordance with the standards [91, 92] is not significantly changed: the average for all measurements was $0.95\,\mu s$ with a standard deviation of 1%.

Measurements made with the pure and damped capacitive dividers for comparison with NBS1 and NBS3 are shown in Figure 48. The output of the damped capacitive divider is significantly distorted due to this divider's slow response time. The average virtual front time, T_1 found from these measurements was 1.1 μs with a standard deviation of 0.62%. This represents a 14.4% front-time error which exceeds the 10% error limit for the time parameters prescribed by the standards [91, 92]. This error would only be revealed through the comparison measurements made here and not through step-response measurements since the divider's measured unit step-response time of 129 ns fell well within the 200 ns limit required by the IEC standard [91].

The results for all four dividers in independent and combined measurement of standard lightning impulses were not significantly different except when the pure capacitive divider was in the circuit. The implication of this is that the interactions observed in the step-response measurements do not affect the measurement of lightning waveforms except when one of the dividers is highly resonant, such as the pure capacitive divider. For standard-lightning impulses chopped at or near the voltage crest, the measurements of time-to-chop and crest voltages agreed very well when the NBS1 and NBS3 dividers were simultaneously used. The measurements for the impulse voltages chopped near the crest did not agree so well when the capacitive divider was in the circuit. The oscillations present in this case, as the step-response measurements indicate, give rise to crest voltage values that are too high, since the time-to-chop inadvertently coincided with the crest of an oscillation.

The problems associated with evaluating the crest voltage with oscillations present, whether due to the divider interactions or caused by the input waveform itself, are clearly seen in Figure 49(a), where measurements made with the NBS1 divider in combination with the pure capacitive divider are shown for chopped impulse voltages. The undamped pure capacitive divider modifies the waveshape so that the crest voltage is almost 2% lower than the individual measurement and the undershoot on the voltage collapse is much larger.

Figure 49(b) shows the results from the combination of the NBS1 divider in the critically damped configuration and the pure capacitive divider. The oscillations are nearly absent in this configuration and the crest voltages are lower as a result of the slower response time of the critically damped divider.

For the front-chopped waveforms, measurements made with the NBS1 divider in various combinations with other dividers, is shown in Figure 50. The measurement of the crest voltage depends upon the time-to-chop for the undamped divider due to the severe oscillations on the wavefront (Figure 50(a)). Figure 50(b) indicates that these problems are not so severe for the critically damped NBS1 divider. Only the pure capacitive divider affects the measurement for this case with the oscillations seen in Figure 50(a) absent, as was anticipated from the step response measurements.

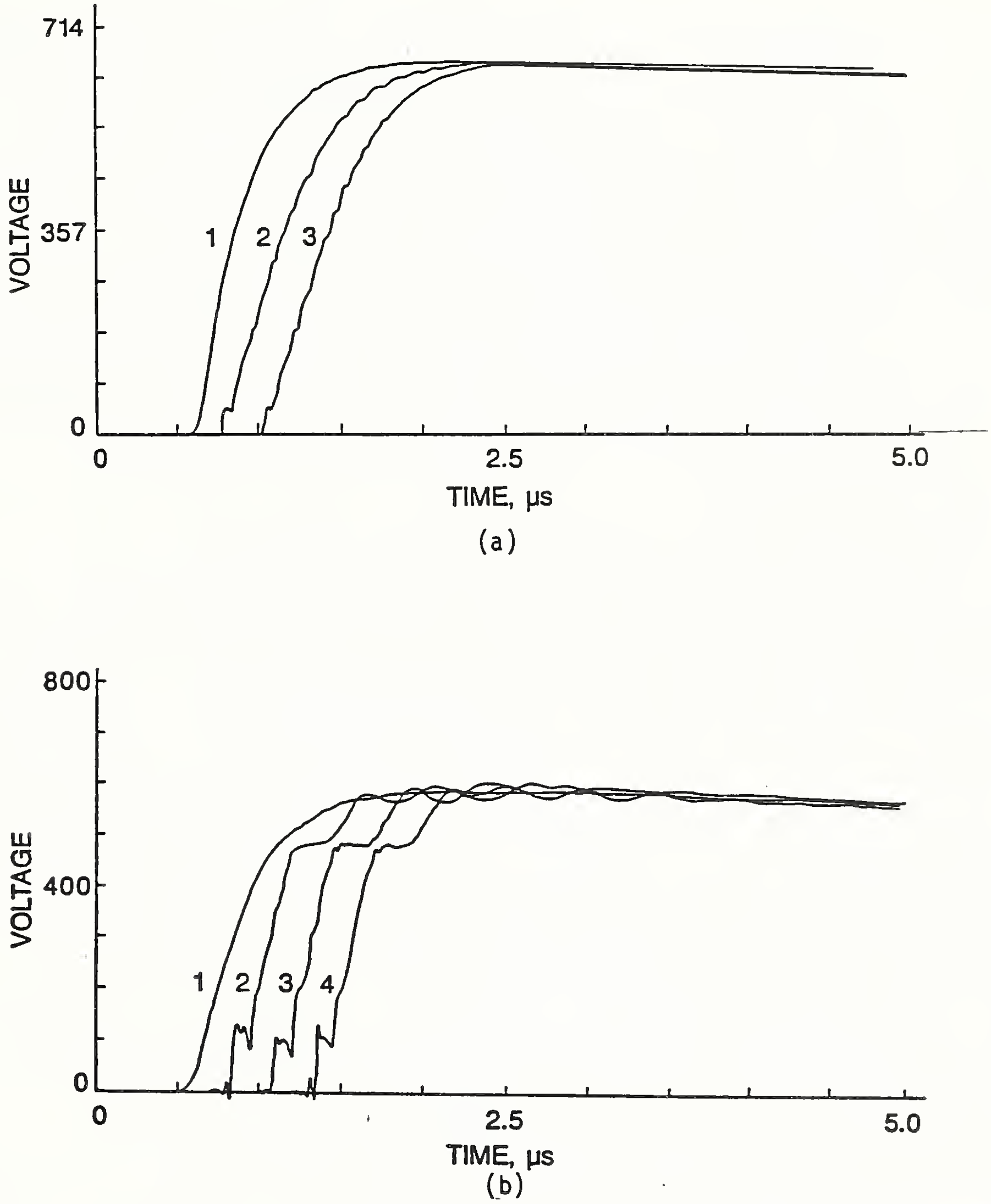

Figure 48. Response of damped and pure capacitive dividers to standard lightning impulses.

(a) Damped capacitive divider
  (1) Input waveform
  (2) Independent divider
  (3) Combined with NBS1 divider, $R_{d1} = 0\,\Omega$

(b) Pure capacitive divider
  (1) Input waveform
  (2) Independent divider
  (3) Combined with NBS1, $R_{d1} = 0\,\Omega$
  (4) Combined with NBS1, $R_{d1} = 350\,\Omega$

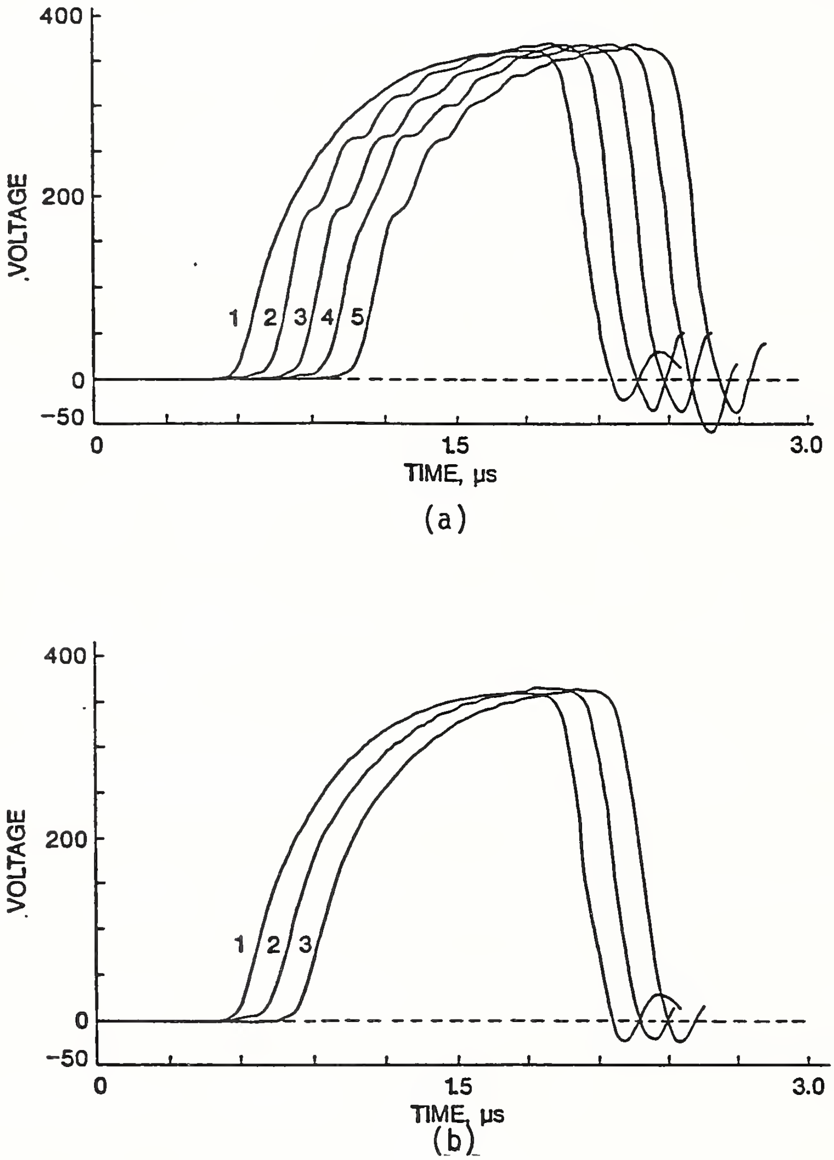

Figure 49. NBS1 divider, chopped lightning impulse, chop at crest.

(a) $R_{d1} = 0\,\Omega$

(1) Input waveform
(2) Independent divider
(3) Combined with NBS3 divider, $R_{d3} = 0\,\Omega$
(4) Combined with pure capacitive divider, $R_{dc} = 0\,\Omega$
(5) Combined with pure capacitive divider, $R_{dc} = 550\,\Omega$

(b) $R_{d1} = 400\,\Omega$

(1) Input waveform
(2) Independent divider
(3) Combined with NBS3, $R_{d3} = 0\,\Omega$

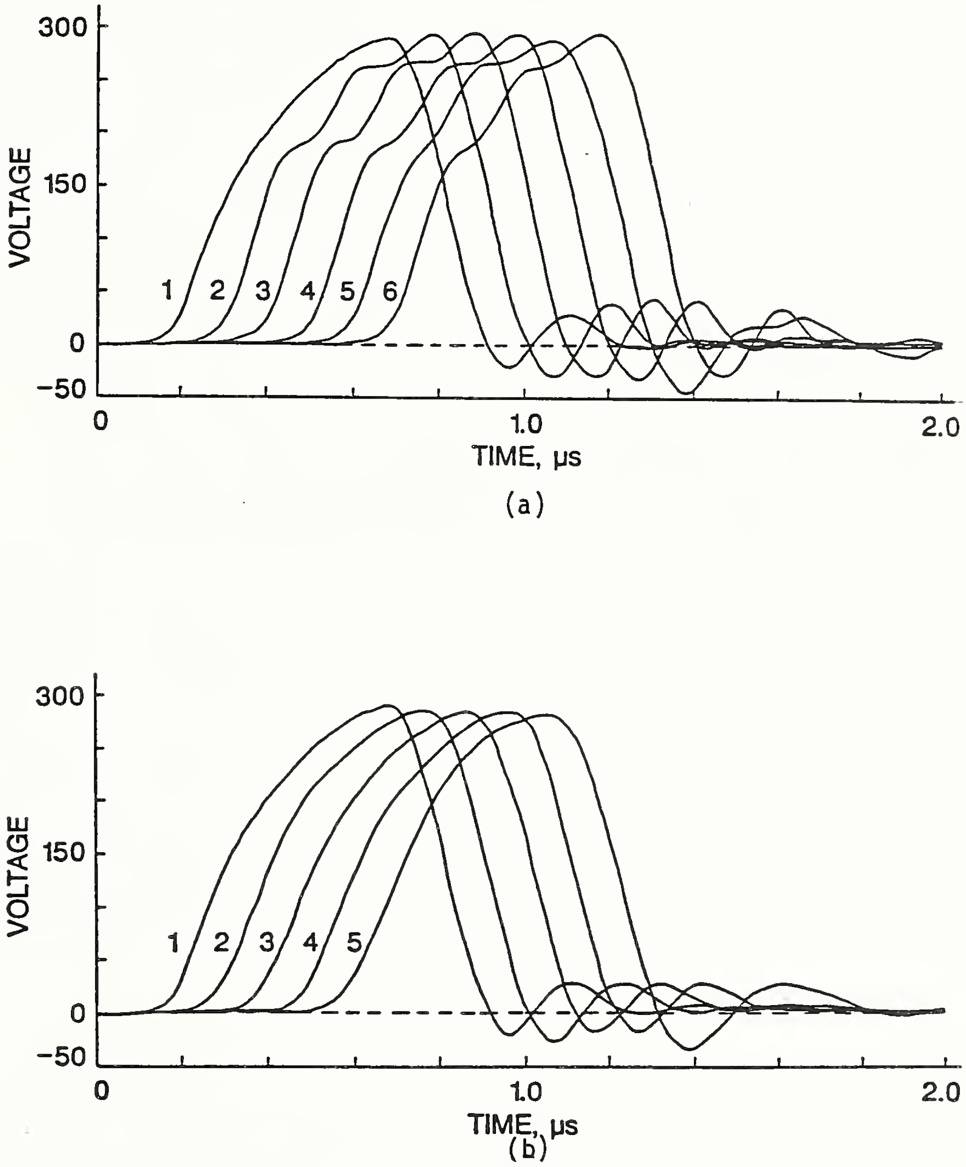

Figure 50. NBS1 divider, chopped lightning impulse, chop at front.

(a) $R_{d1} = 0\,\Omega$
  (1) Input waveform
  (2) Indepenent divider
  (3) Combined with NBS3 divider, $R_{d3} = 0\,\Omega$
  (4) Combined with NBS3, $R_{d3} = 550\,\Omega$
  (5) Combined with pure capacitive divider, $R_{dc} = 0\,\Omega$
  (6) Combined with pure capacitive divider, $R_{dc} = 550\,\Omega$
(b) $R_{d1} = 400\,\Omega$
  (1) Input waveform
  (2) Independent divider
  (3) Combined with NBS3, $R_{d3} = 0\,\Omega$
  (4) Combined with NBS3, $R_{d3} = 550\,\Omega$
  (5) Combined with pure capacitive divider, $R_{dc} = 0\,\Omega$

The strong interactions observed in the step-response measurements were less important in the measurement of standard full standard lightning impulses than in the measurement of chopped-lightning impulses. This is due to the differences in the frequency spectra of the two types of waveforms as illustrated in Figure 51. The spectrum for the full standard lightning waveform has a 3 dB bandwidth of 10 kHz and has very small frequency components above 1 MHz, while that for the chopped lightning waveforms has significant components up to 10 MHz. The resonant oscillations for the divider systems had frequencies greater than 2.3 MHz indicating that for the full standard lightning impulse there is not enough energy in the frequency components above 1 MHz to excite resonance even for the undamped case, while for the chopped-lightning impulse there is.

4.2.6 Conclusions

The interaction between two divider measuring systems in a simultaneous comparison measurement can produce distortions in the step-response waveforms that are unacceptably large according to the relevant international standards [91, 92]. This is especially of concern when the resonances due to the inductances of the connecting leads and the stray capacitances of the leads and divider themselves are undamped.

Although the divider interactions were large in the step-response measurements, they were smaller for the systems studied here for full standard lightning impulse measurement. The interactions produced errors in the determination of the crest value, time-to-chop, and collapse time of chopped-lightning impulses. The dominant source of error was the lower frequency and higher amplitude oscillation of the individual undamped dividers.

The differences in the degree of interaction observed in the measurements of step-response, full standard lightning, and chopped-lightning waveforms is explained qualitatively through the differences in their frequency spectra with respect to the resonant frequencies of the dividers. The dividers' resonant frequencies are a few megahertz and the normalized full standard lightning waveform frequency spectrum has very small components in this range. The normalized chopped-lightning waveform has larger amplitude components in this range and has still larger ones for the step-voltage waveform. Thus, the interaction effects are most noticeable in the step-response measurements, less noticeable in the chopped-lightning impulse measurements, and least noticeable in the full standard lightning impulse measurements.

The purpose of this study has been to observe the interactions of dividers used in simultaneous measurements in which one divider is compared with a reference divider to observe its dynamic response and for evaluation of its scale factor (divider ratio). To perform this assessment accurately, it must be demonstrated that significant interactions do not exist. This can be shown in the following manner: first, by measuring

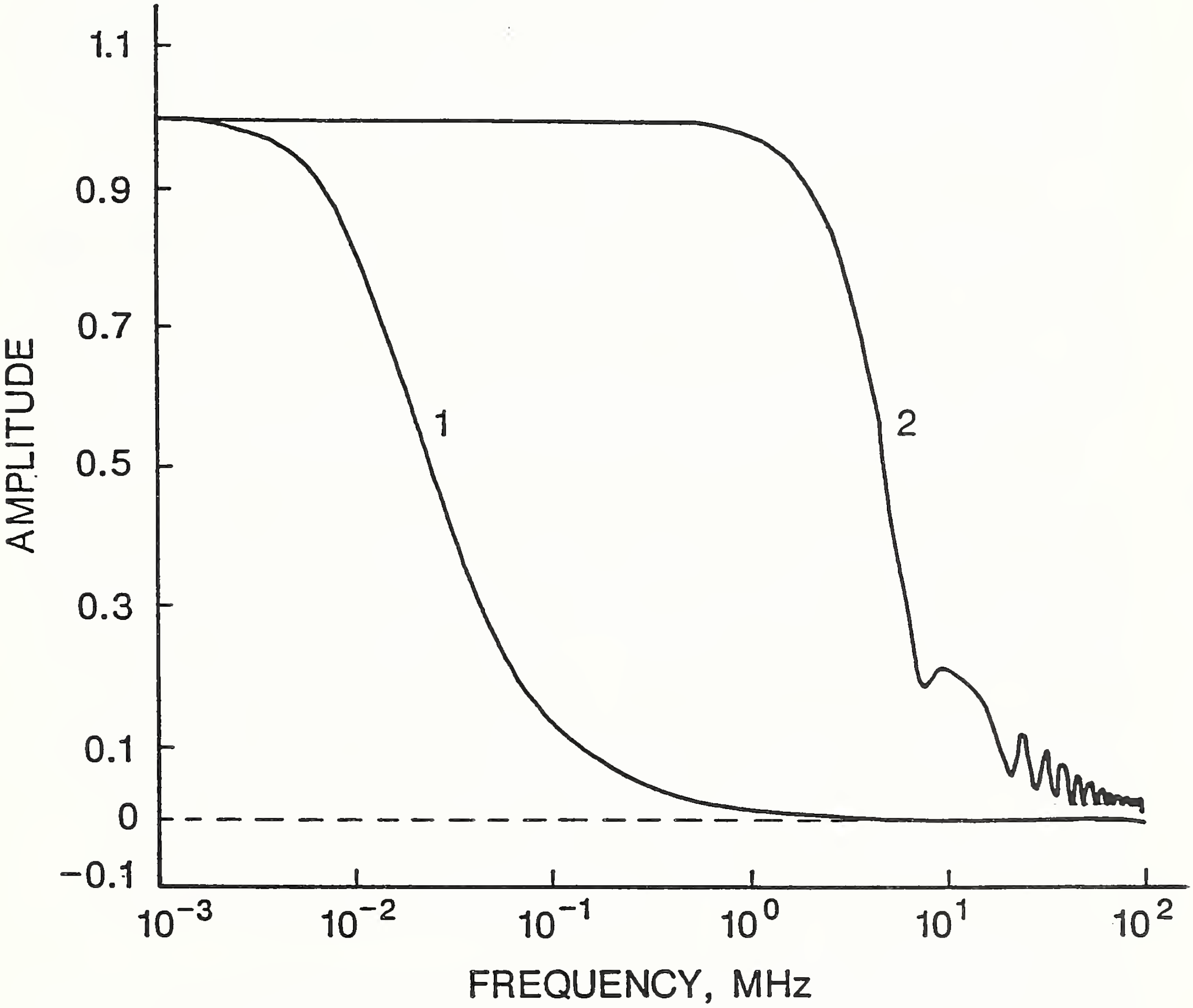

Figure 51. The power spectra of (1) a standard 1.2/60 μs lightning impulse and (2) a chopped-lightning impulse. The waveform was chopped at a voltage 0.9 of the crest and the collapse time was 100 ns.

the voltage waveform of interest in an undamped condition. Then by damping one of the divider systems and observing changes in measurements made with the other and by repeating the procedure with the role of the damped and undamped systems reversed. If significant interactions exist, they may be minimized through the use of damping resistors or, in some cases, through changing the relative positions of the divider systems. In any event, the interactions must be proven negligible in order to accurately perform the comparison measurement.

5. REFERENCES

[1] M. Misakian, W. E. Anderson, and O. B. Laug, "Drift tubes for characterizing atmospheric ion mobility spectra using ac, ac-pulse, and pulse time-of-flight measurement techniques," Rev. Sci. Instrum., Vol. **60**, pp. 720–729 (1989).

[2] M. Misakian and R. H. McKnight, "DC Electric Field Effects During Measurements of Monopolar Charge Density and Net Space Charge Density Near HVDC Power Lines," Paper 89 WM 110–8 PWRD presented at IEEE/PES 1989 Winter Meeting, to be published in IEEE Trans. Power Delivery.

[3] G. W. Griffen, I. Dzidic, D. I. Caroll, R. N. Stillwell, and E. C. Horning, "Ion Mass Assignments Based on Mobility Measurements," Anal. Chem., Vol. **45**, pp. 1204–1209 (1973).

[4] H. Bohringer, D. W. Fahey, W. Lindinger, F. Howorka, F. C. Fehsenfeld, and D. L. Albritton, "Mobilities of Several Mass-Identified Positive and Negative Ions in Air," Int. J. Mass. Spectrom. Ion Phys., Vol. **81**, pp. 44–65 (1987).

[5] F. L. Eisele, "Direct Tropospheric Ion Sampling and Mass Identification," Intl. J. Mass Spectrometry and Ion Processes, Vol. **54**, pp. 119–126 (1983).

[6] National Institute of Standards and Technology Report, NISTIR88–3886, "Research for Electric Energy Systems - - An Annual Report," R. J. Van Brunt, Editor, December, 1987.

[7] M. Misakian, "Generation and Measurement of dc Electric Fields with Space Charge," J. Appl. Phys., Vol. **52**, pp. 3135–3144 (1981).

[8] A. M. Tyndall and C. F. Powell, "The Mobility of Ions in Pure Gases," Proc. Roy. Soc., Vol. **129**, pp. 162–180 (1930).

[9] H. Israel, *Atmospheric Electricity*, Vol. **1**, translated from the second German edition (1970), available from the National Technical Information Service, Springfield, VA 22151.

[10] B. Vonnegut, and C. B. Moore, "A Study of Techniques for Measuring the Concentration of Space Charge in the Lower Atmosphere," Final Report to Air Force Cambridge Research Center, Contract 19 (604) 1920, January 1958.

[11] R. V. Anderson, "Absolute Measurements of Atmospheric Charge Density," J. Geo. Res., Vol. **71**, pp. 5809–5814 (1966).

[12] W. F. G. Swann, "On Certain Matters Relating to the Theory of Atmospheric Electric Measurements," Terr. Magnet. Atmos. Elect., Vol. **19**, pp. 205–218 (1914).

[13] M. Misakian, R. McKnight, and C. Fenimore, "Calibration of Aspirator-Type Ion Counters and Measurement of Unipolar Charge Densities," National Bureau of Standards Technical Note 1223, 1986. Available from Superintendent of Documents, U. S. Government Printing Office, Washington, D.C. 20402, Stock No. 003–003–02732–4.

[14] M. Misakian, R. McKnight, and C. Fenimore, "Calibration of Aspirator-Type Ion Counters and Measurement of Unipolar Charge Densities," J. Appl. Phys., Vol. **61**, pp. 1276–1287 (1987).

[15] T. D. Bracken, A. S. Capon, and D. V. Montgomery, "Ground Level Electric Fields and Ion Currents on the Celilo-Sylmar ±400 kV DC Intertie During Fair Weather," IEEE Trans. Power Appar. Syst., Vol. PAS-**97**, pp. 370–378 (1978).

[16] T. D. Bracken and B. C. Furumasu, "Fields and Ion Current Measurements in Regions of High Charge Density Near Direct Current Transmission Lines," in *Proceedings of the Conference on Cloud Physics and Atmospheric Electricity,* Issaquah, Washington, August 1978 (American Meteorological Society, Boston), pp. 544–551.

[17] W. F. G. Swann, "The Theory of the Action of the Earth's Potential Gradient In Measurements With the Ebert Ion-Counter," Phys. Rev., Vol. **21**, pp. 449–455 (1922).

[18] R. H. McKnight, and P. M. Fulcomer, "Operation of Ion Counters Near High Voltage DC Transmission Lines," in *Proceedings of the 4th International Symposium on High Voltage Engineering,* Athens, Greece, (1983).

[19] S. C. Coroniti, A. J. Parziale, R. C. Callahan, and R. Patten, "Effect of Aircraft Charge on Airborne Conductivity Measurements," J. Geo. Res., Vol. **57**, pp. 197–205 (1952).

[20] J. H. Kraakevik, "The Airborne Measurement of Atmospheric Conductivity," J. Geo. Res., Vol. **63**, pp. 161–169 (1958).

[21] R. B. Bent, "The Testing of Apparatus for Ground Fair-Weather Space-Charge Measurements," J. Atmos. Terr. Phys., Vol. **26**, pp. 313–318 (1964).

[22] R. H. McKnight, "The Measurement of Net Space Charge Density Using Air Filtration Methods," IEEE Trans. Power Appar. Syst., Vol. PAS-**104**, pp. 971–976 (1985).

[23] W. D. Crozier, "Electrode Effect During Nighttime Low-Wind Periods," J. Geo. Res., Vol. **68**, pp. 3451–3458 (1963).

[24] J. K. Olthoff, R. J. Van Brunt, Y. Wang, R. L. Champion, and L. D. Doverspike, J. Chem. Phys., Vol. **91**, no. (4), pp. 2261–2268 (1989).

[25] Y. Wang, R. L. Champion, L. D. Doverspike, J. K. Olthoff, and R. J. Van Brunt, J. Chem. Phys., Vol. **91**, no. (4), pp. 2254–2260 (1989).

[26] J. K. Olthoff, R. J. Van Brunt, Y. Wang, R. L. Champion, and L. D. Doverspike, *Proc. 9th Int. Conf. on Gas Discharges and Their Applications*, Venice, published by Benetton Editore, Padova, Italy (1988), pp. 363–366.

[27] Y. Wang, R. L. Champion, L. D. Doverspike, J. K. Olthoff, and R. J. Van Brunt, *Proc. 41st Annual Gaseous Electronics Conference*, Minneapolis, Bull. Am. Phys. Soc., Vol. **34**, no. (2), pp. 299 (1989).

[28] J. K. Olthoff, R. J. Van Brunt, Y. Wang, R. L. Champion, and L. D. Doverspike, *Proc. 6th Int. Swarm Seminar*, New York, published by Plenum Press, NY (submitted, 1989).

[29] R. J. Van Brunt and S. V. Kulkarni, Rev. Sci. Instrum. Vol. **60**, no. (9), pp. 3012–3023 (1989).

[30] R. J. Van Brunt and S. V. Kulkarni, *Conference Record of the 1988 IEEE International Symposium on Electrical Insulation*, Cambridge, Massachusetts (IEEE, New York, 1988), pp. 233–237.

[31] S. V. Kulkarni and R. J. Van Brunt, *Proceedings of the 9th International Conference on Gas Discharges and Their Applications*, Venice, Italy, (Benetton, Padova, 1988) pp. 227–230.

[32] R. J. Van Brunt and S. V. Kulkarni, *Proceedings of the 41st Annual Gaseous Electronics Conference*, Minneapolis, Bull. Am. Phys. Soc., Vol. **34**, no. (2), pp. 322 (1989).

[33] J. Kindersberger, Ph.D. Thesis, Technical University of Munich, Munich, W. Germany, (1986) (unpublished); N. Wiegart, L. Niemeyer, F. Pinnekamp, W. Boeck, J. Kindersberger, R. Morrow, W. Zaengl, M. Zwicky, I. Gallimberti, and S. A. Boggs, IEEE/PES 1987 Winter Meeting, New Orleans, LA (1987); N. Wiegart, IEEE Trans. Electr. Insul., Vol. **EI-20**, pp. 587 (1985).

[34] B, C. O'Neill and J. D. Craggs, J. Phys. B: At. Mol. Phys., Vol. **6**, pp. 2634 (1973).

[35] D. Hansen, H. Jungblut, and W. F. Schmidt, J. Phys. D: Appl. Phys., Vol. **16**, pp. 1623 (1983).

[36] K. B. McAfee, Jr. and D. Edelson, Proc. Phys. Soc. (London), Vol. **81**, pp. 382 (1963).

[37] R. N. Compton, D. R. Nelson, and P. W. Reinhardt, Int. J. Mass Spectrom. Ion Phys., Vol. **6**, pp. 117 (1971).

[38] J. P. McGeehan, B. C. O'Neill, A. N. Prasad and J. D. Craggs, J. Phys. D: Appl. Phys., Vol. **8**, pp. 153 (1975).

[39] J. Urquijo-Carmona, I. Alvarez, and C. Cisneros, J. Phys. D: Appl. Phys., Vol. **19**, pp. L207 (1986).

[40] Y. Nakamura and T. Kizu, *Proceedings of 5th International Swarm Seminar*, Birmingham, U. K., pp. 126 (1987).

[41] N. R. White, D. Scott, M. S. Huq, L. D. Doverspike, and R. L. Champion, J. Chem. Phys., Vol. **80**, pp. 1108 (1984).

[42] C. Lifshitz, T. O. Tiernan, and B. M. Hughes, J. Chem. Phys., Vol. **59**, pp. 3182 (1973).

[43] M. S. Foster and J. L. Beauchamp, Chem. Phys. Lett., Vol. **31**, pp. 482 (1975).

[44] D. L. Albritton, I. Dotan, W. Lindinger, M. McFarland, J. Tellinghuisen, and F. C. Fehsenfeld, J. Chem. Phys., Vol. **66**, pp. 410 (1977).

[45] S. L. Lin and J. N. Bardsley, J. Chem. Phys., Vol. **66**, pp. 435 (1977); J. H. Whealton and S. B. Woo, Phys. Rev. A, Vol. **6**, pp. 2319 (1971).

[46] M. H. Khatri, J. Phys. D.: Appl. Phys., Vol. **17**, pp. 273 (1984); P.P. Ong and M. J. Hogan, J. Phys. B: At. Mol. Phys., Vol. **18**, pp. 1897 (1985); H. A. Fhadil, A. T. Numan, T. Shuttleworth, and J. B. Hasted, Int. J. Mass Spectrom. Ion Process., Vol. **65**, pp. 307 (1985); T. Makabe and H. Shinada, J. Phys. D: Appl. Phys., Vol. **18**, pp. 2385 (1985).

[47] R. A. Dressler, J. P. M. Beijers, H. Meyer, S. M. Penn, V. M. Bierbaum, and S. R. Leone, J. Chem. Phys., Vol. **89**, pp. 4707 (1988).

[48] J. L. Moruzzi and L. Harrison, Int. J. Mass Spectrum. Ion Phys., Vol. **13**, pp. 163 (1974).

[49] I. M. Kagan and V. I. Perel, Doklady Akad. Nauk S.S.S.R., Vol. **98**, pp. 575 (1954).

[50] G. H. Wannier, Phys. Rev., Vol. **83**, pp. 281 (1951); Phys. Rev., Vol. **87**, pp. 795 (1952).

[51] H. R. Skullerud, J. Phys. B Atom. Molec. Phys., Vol. **6**, pp. 728 (1973).

[52] K. P. Brand and H. Jungblut, J. Chem. Phys., Vol. **78**, pp. 1999 (1983).

[53] R. Morrow, IEEE Trans. Plasma Sci., Vol. **PS-14**, pp. 234 (1986).

[54] P. L. Patterson, J. Chem. Phys., Vol. **53**, pp. 696 (1970).

[55] Y. Nakamura, J. Phys. D: Appl. Phys., Vol. **21**, pp. 67 (1988).

[56] M. Eccles, A. N. Prasad, and J. D. Craggs, Electronics Lett., Vol. **3**, pp. 410 (1967); B. H. Crichton, G. C. Crichton, and D. J. Tedford, *Proceedings of 2nd International Conference on Gas Discharges*, London, pp. 385 (1972).

[57] T. H. Teich (private communication); also see D. W. Branston, Thesis, University of Manchester, UK (1973).

[58] R. J. Van Brunt, J. Appl. Phys., Vol. **59**, pp. 2314 (1986).

[59] I. Sauers, M. C. Siddagangappa, and G. Harman, *Proc. 6th Int. Symposium High Voltage Eng.*, New Orleans, 1989.

[60] P. J. Hay, J. Chem. Phys., Vol. **76**, pp. 502 (1982).

[61] R. W. Odom, D. L. Smith, and H. H. Futrell, J. Phys. B: Atom. Molec. Phys., Vol. **8**, pp. 1349 (1975); J. E. Delmore and L. D. Appelhans, J. Chem. Phys., Vol. **84**, pp. 6238 (1986).

[62] S. Chowdhury and P. Kebarle, J. Chem. Phys. Vol. **85**, pp. 4989 (1986); L. W. Sieck, J. Phys. Chem., Vol. **90**, pp. 6684 (1986).

[63] R. Bartnikas and J. H. E. Levi, IEEE Trans. Instrum. Meas., Vol. IM–**18**, pp. 341 (1969); R. Bartnikas and J. H. E. Levi, Rev. Sci. Instrum., Vol. **37**, pp. 1245 (1966); R. Bartnikas, IEEE Trans. Electr. Insul., Vol. EI-**7**, pp. 3 (1972); Vol. EI-**18**, pp. 2 (1973).

[64] R. J. Van Brunt and D. Leep, J. Appl. Phys., Vol. **52**, pp. 6588 (1981).

[65] R. Bartnikas, IEEE Trans. Electr. Insul., Vol. EI-**22**, pp. 629 (1987).

[66] J. C. Bapt, Bui-Ai, and C. Mayoux, *1973 Annual Report, Conf. on Electrical Insulation and Dielectric Phenomena* (National Academy of Sciences/NRC), Washington, D.C., 1974) pp. 282–288.

[67] R. J. Van Brunt and M. Misakian, IEEE Trans. Electr. Insul., Vol. EI-**17**, 106 (1982).

[68] J. A. Cross, R. Morrow, and G. N. Haddad, J. Phys. D: Appl. Phys., Vol. **19**, pp. 1007 (1986).

[69] S. V. Kulkarni and R. S. Nema, *Conference Record of the 1988 IEEE International Symposium on Electrical Insulation*, Cambridge, Massachusetts (IEEE, New York, 1988), pp. 364–367; S. V. Kulkarni and R. S. Nema, *Gaseous Dielectrics V, Proc. of 5th Int. Symp. Gaseous Dielectrics*, Knoxville (Pergamon Press, New York, 1987) pp. 637–642.

[70] M. Cernak and T. Hosokawa, Japan. J. Appl. Phys., Vol. **27**, pp. 1005 (1988); Appl. Phys. Lett., Vol. **52**, pp. 185 (1988).

[71] G. W. Trichel, Phys. Rev., Vol. **54**, pp. 1078 (1938).

[72] L. B. Loeb, A. F. Kip, G. G. Hudson, and W. H. Bennett, Phys. Rev., Vol. **60**, pp. 714 (1941).

[73] L. Lama and C. F. Gallo, J. Appl. Phys., Vol. **45**, pp. 103 (1974).

[74] R. Morrow, Phys. Rev. A, Vol. **32**, pp. 1799 (1985).

[75] N. H. Malik and A. A. Al-rainy, IEEE Trans. Electr. Insul., Vol. EI-**22**, pp. 825 (1987); A. A. Al-rainy, N. H. Malik, and Al- Bahloul, IEEE Trans. Electr. Insul., Vol. EI-**24**, pp. 699–707 (1989).

[76] H. G. Stever, Phys. Rev., Vol. **61**, pp. 38 (1942); C. G. Montgomery and D. D. Montgomery, Phys. Rev., Vol. **57**, pp. 1030–1040 (1940).

[77] A. L. Wintenberg, M. O. Pace, and T. V. Blalock, *Conference Record of the 1988 IEEE International Symposium on Electrical Insulation*, Cambridge, Massachusetts (IEEE, New York, 1988), pp. 383–386.

[78] J. H. Mason, IEEE Trans. Elec. Insul., Vol. EI-**13**, pp. 211 (1978).

[79] B. Eliasson, M. Hirth, and V. Kogelschatz, J. Phys. D: Appl. Phys., Vol. **20**, pp. 1421 (1987).

[80] J. L. Melsa and A. P. Sage, *An Introduction to Probability and Stochastic Processes* (Prentice-Hall, Englewood Cliffs, New Jersey, 1973) pp. 89–106. The notation adopted here for probability distributions differs somewhat from that given in this reference where, for example, the probability for any pulse to have amplitude between q_n and $q_n + dq_n$ might be more appropriately denoted by $p_{q_n}(x)dx$ instead of $p_0(q_n)dq_n$. Here x represents values assumed by the random variable q_n. The notation used in this text for conditional probabilities would also require that $p_1(q_n \,|\, \Delta t_{n-1})dq_n = p_{q_n|\Delta t_{n-1}}(x \,|\, y)dx$ where y represents the values assumed by Δt_{n-1}.

[81] W. Feller, *An Introduction to Probability Theory and Its Applications*, Vol. 1 (John Wiley and Sons, New York, 1968) pp. 114–237.

[82] P. S. Gardiner, Proc. IEE, Vol. **125**, no. (**5**), pp. 467–468 (1978).

[83] R. Zentner, Z. Angew, Phys., Vol. **29**, pp. 294–301 (1970).

[84] E. F. Kelley and R. E. Hebner, "Electro-Optic Field Measurement at a Needle Tip and Streamer Initiation in Nitrobenzene," 1986 IEEE Conference on Electrical Insulation and Dielectric Phenomena, Claymont, DE, Nov. 2–6, 1986, pp. 272–277 (Nov. 1986).

[85] M. O. Pace, D. N. Pittman, A. L. Wintenberg, I. Alexeff, and T. V. Blalock, "Effects of Pressure Near One Atmosphere on Prebreakdown Current Pulses at a Needle Cathode in Hexane," Conference Record of the 1988 IEEE International Symposium on Electrical Insulation, Cambridge, Massachusetts, 88CH2594-0-DEI, pp. 23–26 (June 1988).

[86] P. K. Watson, "EHD Instabilities in the Breakdown of Point-Plane Gaps in Insulating Liquids," Proc. IEEE Conference on Electrical Insulation and Dielectric Phenomena, pp. 370–376 (1981).

[87] I. Alexeff, T. V. Blalock, A. L. Wintenberg, J. V. Foust, and M. O. Pace, "Multipulse Prebreakdown Phenomena in Liquid Dielectrics – Advanced Theory," Proc. A.P.S. 29th Annual Meeting, Division of Plasma Physics, pp. 1954 (1987).

[88] C. Fenimore, " The Thermal-Expansive Growth of Prebreakdown Streamers in Liquids," Conference Record of the 1988 IEEE International Symposium on Electrical Insulation, Cambridge, Massachusetts, 88CH2594-0-DEI, pp. 27–30 (June 1988).

[89] R. S. Sigmond, R. Hegerberg, and D. Linhjell, "Image Converter Recording of Spontaneous DC Breakdown of Corona Gaps in Air-SF_6 Mixtures," Fifth International Symposium on High Voltage Engineering, Braunschweig, Federal Republic of Germany, paper 15.05, pp. 24–28 (August 1987).

[90] B. Lieberoth-Leden and W. Pfeiffer, "Predischarge Development in N_2 and SF_6 at High Gas Pressure," IEEE Trans. Elec. Insul., Vol. **24**, No. 2, pp. 285–296 (April 1989).

[91] International Electrotechnical Commission, High Voltage Test Techniques, IEC Publication 60–1,2,3,4, (1973–1977).

[92] IEEE Standard Techniques for High Voltage Testing, IEEE Std **4** (1978).

[93] Y. X. Zhang, R. H. McKnight, and R. E. Hebner, "Interactions Between Two Dividers Used in Simultaneous Comparison Measurements,"

[94] Qi Qing-Cheng and W. S. Zaengl, "Investigations of Errors Related to the Measured Virtual Front Time T1 of Lightning Impulses," IEEE Trans. Power Appar. Sys., Vol. PAS-**102**, pp. 2379–2390 (1983).

[95] Draft High Voltage Test Techniques Revision of Publication 60–3 and 60–4; Prepared by WG7 of IEC/TC42 (undated).

[96] F. C. Creed and M. M. C. Collins, "The Measurement of Short-Duration Impulse Voltages," IEEE Trans. Commun. Elect., Vol. **82**, pp. 621–630 (1963).

[97] IRR-IMS-Group: "Facing UHV Measuring Problems," Electra No. **35** (July 1974).

[98] R. Malewski, "Measuring Properties of IREQ's 5.4 MV Voltage Divider," IEEE Proceedings, Vol. **133**, Pt. A, pp. 523–533 (1986).

[99] D. Kind, H. Korff, A. Schmidt, and K. Schon, "Chopping Errors for Characterizing HV Impulse Dividers," paper 71.02, Fifth International Symposium on High Voltage Engineering, Braunschweig, FRG (1987).

NBS-114A (REV. 2-80)

U.S. DEPT. OF COMM. **BIBLIOGRAPHIC DATA SHEET** *(See instructions)*	1. PUBLICATION OR REPORT NO. NISTIR 89-4167	2. Performing Organ. Report No.	3. Publication Date OCTOBER 1989

4. TITLE AND SUBTITLE

Research for Electric Energy Systems - An Annual Report

5. AUTHOR(S)

Richard J. Van Brunt, Editor

6. PERFORMING ORGANIZATION *(If joint or other than NBS, see instructions)*

NATIONAL INSTITUTE OF STANDARDS AND TECHNOLOGY
~~NATIONAL BUREAU OF STANDARDS~~
U.S. DEPARTMENT OF COMMERCE
GAITHERSBURG, MD 20899

7. Contract/Grant No.

8. Type of Report & Period Covered

9. SPONSORING ORGANIZATION NAME AND COMPLETE ADDRESS *(Street, City, State, ZIP)*

Department of Energy
Division of Electric Energy Systems
1000 Independence Avenue, SW
Washington, D.C. 20585

10. SUPPLEMENTARY NOTES

☐ Document describes a computer program; SF-185, FIPS Software Summary, is attached.

11. ABSTRACT *(A 200-word or less factual summary of most significant information. If document includes a significant bibliography or literature survey, mention it here)*

This is a report of technical progress in four investigations conducted at NIST and supported by the U.S. Department of Energy under Task Order Number 137. The first investigation is concerned with the measurements of electric fields and ions in the vicinity of high-voltage transmission lines and biological exposure facilities. For this investigation, results are reported on evaluations of two methods for measuring ion mobilities at atmospheric pressure and an aspiratory-type ion counter for measuring monopolar charge densities in air. The second investigation is concerned with development of advanced diagnostics for compressed gas-insulated power systems. For this investigation, results are reported on measurements of collisional electron detachment and negative ion conversion reactions in SF_6 and on a new technique for measuring the stochastic behavior of partial discharges. The third investigation is concerned with measurement of prebreakdown phenomena at solid-liquid dielectric interfaces. Results are presented here from optical observations of the influence of hydrostatic pressure on prebreakdown partial discharge development and measurement of nanosecond impulse breakdown at liquid-solid interfaces. The fourth area of research is concerned with electrical measurement of fast transient phenomena. Results are presented from an investigation into the interactions between two dividers used simultaneously to measure fast impulse voltages.

12. KEY WORDS *(Six to twelve entries; alphabetical order; capitalize only proper names; and separate key words by semicolons)*

corona discharges; drift tubes; electron detachment; impulse dividers; interfacial breakdown; ion mobilities; ion densities; liquid dielectrics; optical delays; partial discharges; sulfur hexafluoride; transient measurements.

13. AVAILABILITY

☒ Unlimited
☐ For Official Distribution. Do Not Release to NTIS
☐ Order From Superintendent of Documents, U.S. Government Printing Office, Washington, D.C. 20402.
☒ Order From National Technical Information Service (NTIS), Springfield, VA. 22161

14. NO. OF PRINTED PAGES
108

15. Price
A06